Optical Tweezers for Signal Detection and Micromanipulation

Pamela Ann Jordan

UNIVERSITY
of
GLASGOW

Department of Electronic and Electrical Engineering
and
Department of Physics and Astronomy

Thesis submitted for the degree of Doctor of Philosophy

8th June 2005

Abstract

The work presented in this thesis explores new multi-disciplinary applications of optical tweezers in the physical and biological sciences. Firstly, the three dimensional trapping of partially silvered spheres in a standard TEM_{00} optical trap was characterised. These spheres were then coated with an azo dye such that surface-enhanced resonance Raman (SERRS) measurements could be made on a single bead whilst it was simultaneously trapped in 532 nm optical tweezers. The length of time over which the SERRS signal could be recorded was increased, from milli-seconds to minutes, by using 1064 nm optical tweezers and introducing second harmonic light, generated via a frequency doubling crystal, for the excitation of the SERRS signal. In addition to trapping single particles, a spatial light modulator (SLM) was introduced into the optical tweezers to produce holographic optical tweezers. The SLM allowed the creation and manipulation of several optical beams both simultaneously and independently of each other. Three dimensional trapping and manipulation of multiple micron-sized spheres were achieved using the SLM in the Fourier plane of the traps. This ability to trap and manipulate objects, such as fluorescent spheres and *E. coli*, in 3D was extended to create permanent 3D structures that were set within a polymer matrix. These objects could be created, permanently set and imaged ex-situ. A summary of conclusions and ideas for future work are included.

For my parents, Mary and John

Chan fhiosrach mur feòraich.

Declaration

I declare that, except where explicit reference is made to the contribution of others, that this dissertation is the result of my own work and has not been submitted for any other degree at the University of Glasgow or any other institution.

Pamela Ann Jordan

Publications

Journal publications:

- Pamela Jordan, Hugh Clare, Leonard Flendrig, Jonathan Leach, Jon Cooper and Miles Padgett, "Permanent 3D microstructures in a polymeric host created using holographic optical tweezers", J. Mod. Opt. 51, 627-632 (2004).

- Pamela Jordan, Graeme McNay, Frances T. Docherty, Gavin Sinclair, W. Ewen Smith, Jonathan M. Cooper and Miles Padgett, "3D optical trapping of partially silvered microparticles" Opt. Lett., 29, 2488-2490 (2004).

- Gavin Sinclair, Pamela Jordan, Jonathan Leach, Miles J. Padgett and Jon Cooper, "Defining the trapping limits of holographical optical tweezers", J. Mod. Opt. 51, 409-414 (2004).

- Jonathan Leach, Gavin Sinclair, Pamela Jordan, Johannes Courtial, Miles J. Padgett, Jon Cooper and Zsolt J. Laczik, "3D manipulation of particles into crystal structures using holographic optical tweezers", Opt. Express 12, 220-226 (2004).

- Gavin Sinclair, Jonathan Leach, Pamela Jordan, Graham Gibson, Eric Yao, Zsolt John Laczik, Miles J. Padgett and Johannes Courtial, "In-

teractive application in holographic optical tweezers of a multi-plane Gerchberg-Saxton algorithm for three-dimensional light shaping". Opt. Express 12, 1665-1670 (2004).

- Graeme McNay, Frances T. Docherty, Duncan Graham, W. Ewen Smith, Pamela Jordan, Miles Padgett, Jonathan Leach, Gavin Sinclair, Paul B. Monaghan and Jonathan M. Cooper, "Visual observation of SERRS from single silver coated silica microparticles within optical tweezers", Angew. Chem. Int. Ed., 43, 19, 2512-2514 (2004).

- Gavin Sinclair, Pamela Jordan, Johannes Courtial, Miles Padgett, Jon Cooper and Zsolt John Laczik, "Assembly of 3-dimensional structures using programmable holographic optical tweezers", Opt. Express, 12, 22, 5475-5480 (2004).

- Pamela Jordan, Jonathan M. Cooper, Graeme McNay, Frances T. Docherty, W. Ewen Smith, Gavin Sinclair and Miles Padgett, "Surface enhanced resonance Raman scattering in optical tweezers using co-axial second harmonic generation" Opt. Express, 13, 11, 4148-4154 (2005).

- Ethan Schonbrun, Pamela Jordan, Johannes Courtial and Miles Padgett, "3D interferometric optical tweezers, using a single spatial light modulator", Opt. Express, 13, 10, 3777-3786 (2005).

- Pamela Jordan, Jonathan M. Cooper, Mattias Goksör, Dag Hanstorp, Amanda Wright, John Girkin, Paul Blackburn and Miles Padgett, "Ex-situ imaging of fluorescent permanent 3D structures created using holographic optical tweezers", in preparation 2005.

Conference proceedings:

- Gavin Sinclair, Pamela Jordan, Johannes Courtial, John Laczik and Miles Padgett, "Pre-programmable assembly of 3-dimensional structures using holographic optical tweezers", SPIE January 2005.

- Gavin Sinclair, Pamela Jordan, John Laczik, Johannes Courtial and Miles Padgett, "Semi-automated 3-dimensional assembly of multiple objects using holographic optical tweezers", SPIE, Denver, August 2004.

- Miles Padgett, Jonathan Leach, Gavin Sinclair, Johannes Courtial, Eric Yao, Graham Gibson, Pamela Jordan, Jon Cooper and John Laczik, "Three dimensional structures in optical tweezers", SPIE, Denver, August 2004.

- Jonathan Leach, Pamela Jordan, Gavin Sinclair, Johannes Courtial, Miles Padgett, Jon Cooper and John Laczik, "Crystal structures within optical tweezers", CLEO, Baltimore, June 2003.

Presentations:

- P. Jordan, "3D manipulation using SLM's in optical tweezers", Chalmers University, Gothenburg, Sweden. November 2004.

- P. Jordan, "Biofabrication and SERRS in optical tweezers", European Optical Tweezers Meeting, Greenock, September 2004.

- P. Jordan, "Introduction to holographic optical tweezers", Bioengineering Group Seminar, March 2004.

- P. Jordan, "3D trapping of partially silvered microparticles". The Burn. March 2004.

- P. Jordan, "Micromanipulation using holographic optical tweezers". Unilever, Research and Development Colworth, March 2004.

Posters:

- P. Jordan, "Application of a single spatial light modulator to form a 3D optical lattice for interferometric optical tweezers", IoP 100 years after Einstein, Warwick (2005).

- P. Jordan, "Permanent 3D structures in a polymer host created using holographic optical tweezers", Photon '04, Glasgow Caledonian University (2004).

- P. Jordan "Visual SERRS in optical tweezers", Photon '04, Glasgow Caledonian University (2004).

Acknowledgments

There are so many wonderful and talented people that I would like to thank for all their help and patience that I am at a loss as to where to begin.

I will start by thanking my supervisors Jon Cooper and Miles Padgett for all their help, motivation and encouragement throughout my PhD and for helping me to cross the boundaries between Physics, Engineering and Chemistry and being involved in several interesting and varied experiments. Both Jon and Miles are extremely talented people and I have nothing but respect and admiration for them. Their wealth of knowledge has helped me immensely and I would like them to know that I appreciate all of their support.

I will also take this opportunity to thank Unilever who are my industrial sponsors and who have shown a keen and involved interest in all my work. My supervisors were Hugh, Leonard, Fabien and Bill for periods throughout my PhD. I would particularly like to thank Hugh who has become somewhat of an adopted father to me, who has always given me good advice and remains a close friend. Not only have Unilever part funded my PhD, but they also gave me a most wonderful opportunity to work with Prof Howard Stone and his microfluidics group at Harvard University, Boston. It was a fantastically interesting visit and Howard taught me a lot about fluid dynamics and two phase flows.

Then there is the optics group where the majority of my work was done. I worked particularly closely with Miles, Gavin, Jonathan, Johannes and Eric and I have to thank them so much for coming through to the lab to chat to me so that I didn't get too lonely!! Then there is Martin, Ben, Ken, Graeme and Graham who I haven't worked with so closely but who has always been there for a chat and a laugh.

Then there is my collaboration with the Department of Pure and Applied Chemistry at Strathclyde University where I worked with Graeme, Frances and Ewen.

I would also like to thank Dag, Mattias, Emma and baby Erik for their hospitality when I visited Sweden and their help with experiments while I was there.

I also have to say a huge thank you to all my friends who kept me sane throughout my PhD and who ensured that I played just as hard, if not harder, than I worked!! I don't think I have space to name you all personally, but you know who you are! All those coffee breaks, dinners and nights out were just what the doctor ordered!

I would like to thank Joel, for whom words fail me. You are the best, I love you.

Of course, I doubt if I would have got through any of this without the support of my family, particularly my mum, dad, Alison and the mad but loveable Murphy. Thank you so much, I love you all, x x x.

Contents

List of Figures

List of Constants

Symbol	Quantity	Units
c	velocity of light	m/s
d	diameter	m
E	electric field	V/m
∇E	electric field gradient	V/m^2
E	energy	J
F	force	N
g	gravity	$9.81\ m/s^2$
h	Planck's constant	$6.63 \times 10^{-34}\ m^2kg/s$
I	intensity	W/m^2
k	photobleaching rate	s^{-1}
k	Boltzmann's constant	$1.38 \times 10^{-23}\ J/K$
n	refractive index	dimensionless
P	power	W
P	polarisation	C/m^2
$\mathbf{p}$	linear momentum	kgm/s
p_{rad}	radiation pressure	Pa
Q	efficiency of optical tweezers	dimensionless
r	radius	m
$R(z)$	radius of wavefront curvature	m
T	temperature	K
v	velocity	m/s
z_r	Raleigh range	m
α	polarisability (of a particle)	m^2C/V
ε_0	permittivity of free space	F/m
η	viscosity of a fluid	Ns/m^2
λ	wavelength	m
Λ	grating period	m
μ	electric dipole moment	Cm
ν	frequency of light	Hz
ρ	density	kg/m^3
χ	linear dielectric susceptibility	dimensionless
ω	beam radius	m
ω	frequency of oscillating wave	rad/s
ω_0	beam waist	m
ω_{min}	beam waist	m

List of Abbreviations

Abbreviation	Full text
DBS	direct binary search
DOE	diffractive optical element
FWHM	full width half maximum
GS	Gerchberg Saxton
Nd:YAG	neodymium:yttrium-aluminium-garnet
PZT	piezoelectric stage
SERS	surface enhanced Raman scattering
SERRS	surface enhanced resonance Raman scattering
SLM	spatial light modulator
TEM_{00}	transverse electromagnetic (wave)
TEM	transmission electron microscopy

Chapter 1

Introduction

Since their first demonstration in 1986 by Arthur Ashkin [1], optical tweezers have become an important tool for many areas of science with applications in biology [2, 3, 4, 5, 6, 7, 8], chemistry [9, 10, 11] and, more recently, within microfluidic technologies [12, 13, 14, 15, 16, 17]. Optical tweezers operate on the principle that a tightly focussed laser beam can draw a dielectric particle into the region of highest light intensity and trap it, as described in detail in Chapter 2. These trapped particles can be then be manipulated and guided by the focussed laser light.

Although designed by physicists, optical tweezers have found numerous uses in other scientific fields. Several optical tweezers review papers exist, including those with emphasis placed on biological applications [18, 19], the photophysics and photochemistry of laser manipulated microparticles [20] and on optical manipulation within optical tweezers [21]. These papers review the majority of the material available before 2003. However, the last few years has seen new and interesting work being carried out within the field of optical tweezers, much of it "cross-disciplinary". As it is not possible to do a full literature review on optical tweezers within this thesis, a short

summary of the work since 2000 will be presented and the reader referred to the aforementioned review papers for further background.

Biology is currently one of the largest fields that exploit optical tweezers. For example, over the last few years, biologists have used optical tweezers to combine trapping and single molecule fluorescence detection [8], to study the forward and reverse motion of single RecBCD molecules on DNA [22] and to quantify binding interactions of bacteria such as *E. coli* [23]. Optical tweezers and biology have also been combined within cell assays to develop non-destructive, non-contact, on-chip microcultivation [14] and to form microstructure arrays for biosensor applications [24].

Biologists are concerned with interactions at the cellular level, especially cell-cell interactions where it is important to control the number of interactions. In order to perform such experiments, biologists have to be able to isolate, manipulate and organise biological material. As cells are generally between 1 μm and 10 μm in diameter, optical tweezers offer a complementary technology to the microscope for the biologist, allowing the manipulation and visualisation of such samples.

An area that has also seen rapid development within optical tweezers is that of microfluidics and cell sorting. Lasers have been used to sort particles through small (mm) sized channels as far back as 1987 [25]. Sorting has now been achieved through the use of Bessel beams [26] and, with the development of holographic optical tweezers, rapid cell sorting can be achieved using an optical lattice and a microfluidic device [15]. The fabrication of microfluidic structures, such as a peristaltic pump and a valve [12], microoptomechanical pumps driven by holographic optical vortex arrays [27], and optically driven submicron manipulation tools [28] have also all been demonstrated. Optical

tweezers are now even being used to study and manipulate colloidal systems [29, 30].

However, physicists still use optical tweezers to investigate the fundamental properties of light such as measuring the spin and orbital angular momentum [31, 32] and the transfer of momentum and orbital angular momentum to trapped particles [33, 34].

Other uses of optical tweezers include the ability to trap and manipulate highly reflective or metallic particles in two and three dimensions, as described in Chapter 3, and the use of diffractive optical elements to produce holograms to allow manipulation of several particles simultaneously within an optical tweezers system, as discussed in more detail in Chapter 6.

The work presented in this thesis investigates the application of optical tweezers to the well known analytical chemistry technique of surface enhanced resonance Raman scattering (SERRS). Chapter 3 examines the trapping of partially silver coated, micron sized silica particles within optical tweezers. The ability to trap these partially silvered spheres is desirable in order to observe SERRS in optical tweezers, as the roughened silver surface is key to the SERRS enhancement. Chapter 4 examines one experimental setup in which particles can be trapped and a corresponding SERRS signal recorded while Chapter 5 changes the experimental setup slightly to use a dual wavelength optical tweezers in order to achieve long lived SERRS signals, minutes as opposed to milli-seconds achieved in Chapter 4. This technique has potential in the future to be used to manipulate beads, and bead immobilised ligands (such as proteins or DNA) in a sensitive bioanalytical assay, for example.

The remainder of the thesis describes the use of holographic optical tweezers for the simultaneous manipulation of several microparticles in 3 dimensions, and the setting of such particles to make permanent microstructures

was investigated, Chapter 7. The ability to permanently set fluorescent spheres, or fluorescently tagged bacteria, within a gelatin matrix and use it as a probe for a confocal microscope combines the two main strands of the thesis of optical manipulation and signal detection, Chapter 7.

Chapter 2

Optical tweezers and Raman scattering theory

Optical tweezers rely on the extremely high gradient force created in a tightly focussed laser beam to trap and manipulate micron sized objects. With the invention of spatial light modulators, the uses for optical tweezers have advanced allowing independent, 3 dimensional, real time manipulation of multiple particles and biological samples that was previously impossible.

Raman spectroscopy is a non-destructive technique used to collect qualitative and quantitative spectra on various materials, including biological samples. Interrogation of such samples, using optical tweezers, enables simultaneous trapping, visualisation and collection of vibrational spectra, such as Raman, surface enhanced Raman (SERS) and surface enhanced resonance Raman (SERRS). SERRS relies on a metallic surface to enhance the optical signal due to a surface plasmon effect, and is combined with optical tweezers in this thesis.

2.1 The beginning of optical tweezers

2.1.1 Gaussian beams

The laser beams used in conventional optical tweezers systems have a Gaussian intensity profile. In a steady state condition, transverse Gaussian laser modes are sustainable within a laser cavity. Characteristic parameters of a Gaussian beam are the beam size and the wavefront curvature, refer to Figure 2.1.

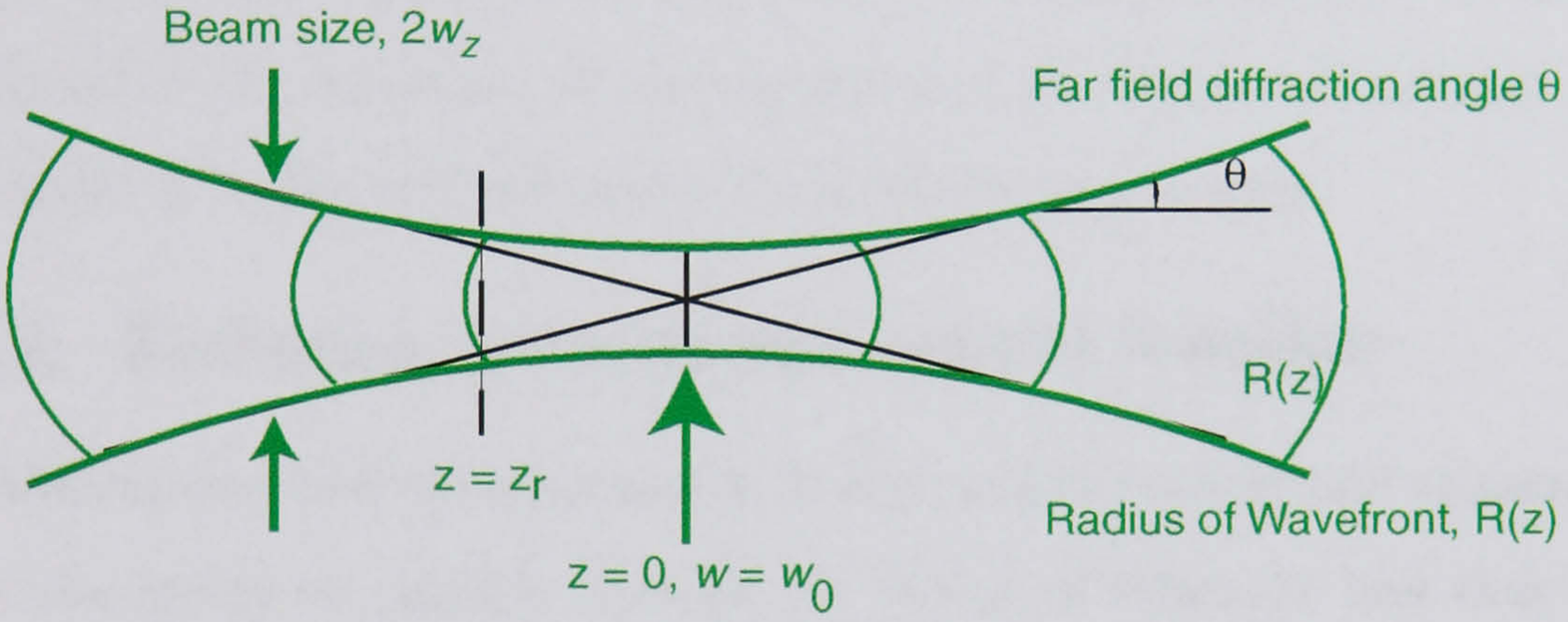

Figure 2.1: The beam size, $2w$, and wavefront curvature, $R(z)$, of a Gaussian beam as described in Section 2.1.1.

At the $z = 0$ position, $w = w_{min} = w_0$ and defines the size of the "Beam Waist", where w_z is the beam size at position z and w_{min} and w_0 are the minimum beam size and are designated the "Beam waist",

$$w_z = w_0\sqrt{1 + \left(\frac{z}{z_r}\right)^2} \tag{2.1}$$

and $R(z)$ is the radius of the wavefront at position z.

$$R(z) = \frac{1}{z}(z^2 + z_r^2) \tag{2.2}$$

where

$$z_r = \frac{\pi w_0^2 n}{\lambda} \tag{2.3}$$

In the above equations, w is the beam radius, z is the distance from the plane of the beam waist to the plane of interest along the z direction, λ is the wavelength and n is the refractive index.

When $z = z_r$, the beam width increases to $w = \sqrt{2}w_0$. The Rayleigh range, or beam parameter, is defined as z_r and is the position where the curvature of the wavefront is a maximum and the radius of curvature is a minimum. It is also defined as the length of the focal region.

2.1.2 Radiation pressure and optical leviation

Maxwell showed that electromagnetic waves transmit energy and momentum from one region to another through his theory of relativity and that it is this transfer of momentum that is responsible for "Radiation Pressure" [35]. When the photons in a light beam are absorbed by an object, the photon's momentum is transferred to the surface of the object. The rate at which momentum is transferred to the surface is equal to the force on the surface. Radiation pressure, p_{rad}, is defined as the average force per unit area and is given by $p_{rad} = I/c$ where the intensity I is defined as the average rate of energy transfer per unit area and c is the velocity of light. If a photon is completely reflected, the resulting change in momentum is twice as great as in the absorbed case and $p_{rad} = 2I/c$. This radiation pressure is extremely small. For example, the radiation pressure of sunlight on the earth is p_{rad} 10^{-6} Pa. Such pressures, and the associated forces, have a negligible effect

on massive bodies, but its effect can be felt on a microscopic scale where bodies can be driven away from the radiation source.

Ashkin first proposed using radiation pressure as a method for studying atoms with light, i.e. to deflect atoms out of an atomic beam [36], in 1970 after demonstrating in 1969 that micron-sized particles could be trapped and accelerated using the radiation pressure from a laser beam [37].

In this ground breaking experiment, Ashkin used a continuous wave TEM_{00} argon laser in the green focused horizontally through a 120 μm glass cell to accelerate and trap transparent latex spheres 0.585 μm, 1.31 μm and 2.68 μm in diameter. These spheres were suspended in water which helped to overcome the radiometric (heating) effects that would otherwise dominate the radiation effects. It was discovered that the 2.68 μm spheres were drawn towards the centre of the milli-Watt powered laser beam and accelerated in the direction of light propagation. Once the sphere hit the wall of the glass cell, the bead remained in its trapped position until the laser beam was removed, after which the sphere would wander off under the mechanics of Brownian motion, see Figure 2.2. The same phenomenon was observed using

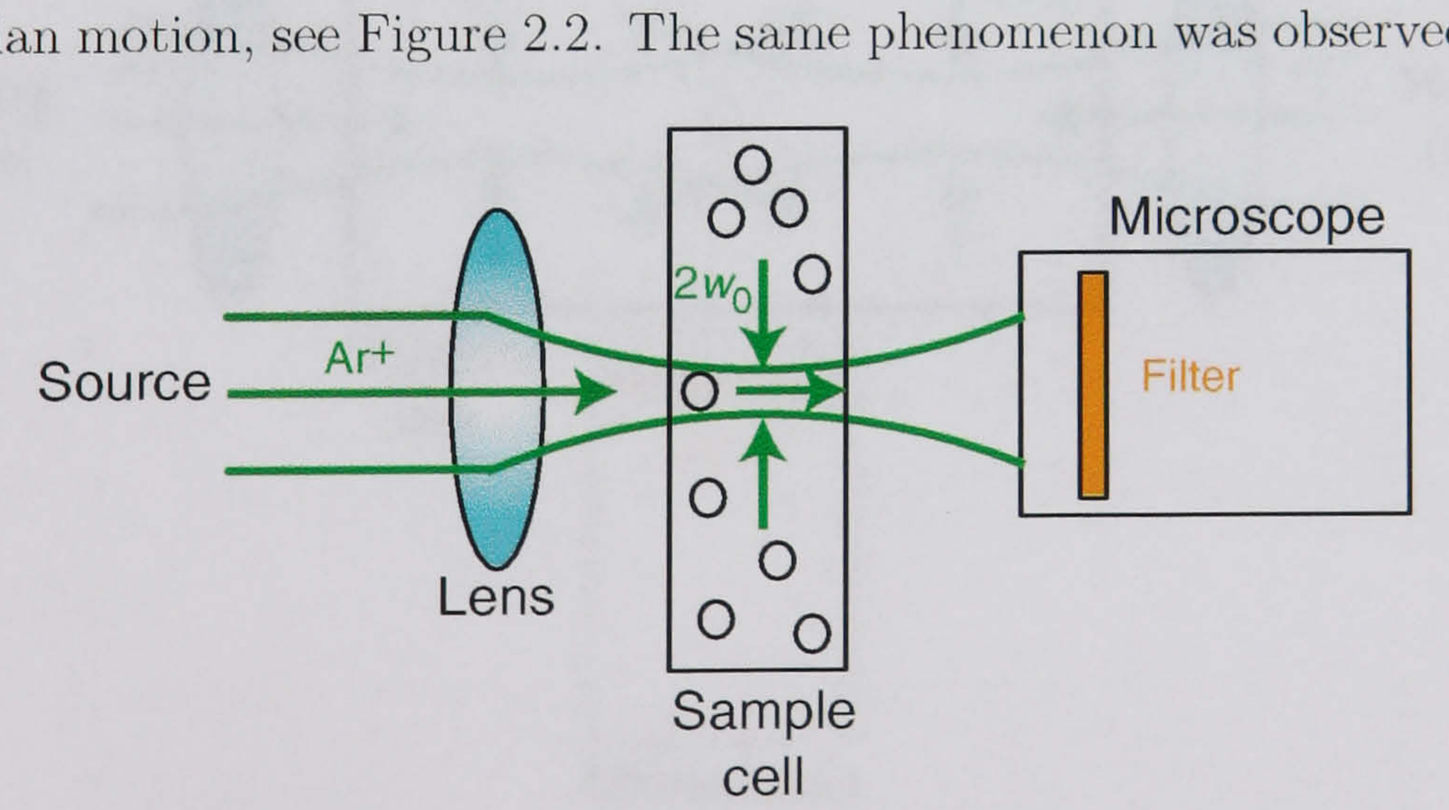

Figure 2.2: A 2.68 μm sphere is drawn into the focus of the laser beam and accelerated in the direction of the light as described in Section 2.1.2.

the smaller particles, but more power was required to accelerate the particles with the same limiting velocity of the larger particles.

Ashkin had demonstrated that high index particles suspended in a low index medium could be accelerated in the axial direction. He further proposed, and showed using air bubbles in a glycerol and water mixture, that low index spheres held within a high index solution would be repelled from the most intense part of the beam. This knowledge allowed modifications to be made to a laser beam in order to trap both high and low index spheres. High index spheres are trapped using the mechanisms described in this Chapter, whilst the trapping of low index spheres follows the same trapping principles as metallic particles. In order to trap low index or metallic particles, methods including scanning [10] and annular [38, 31] beams have been used, see Chapter 3. Low index and metallic particles have also been trapped in Laguerre-Gaussian beams [39] and mixtures of high and low index particles have also been trapped simultaneously [40].

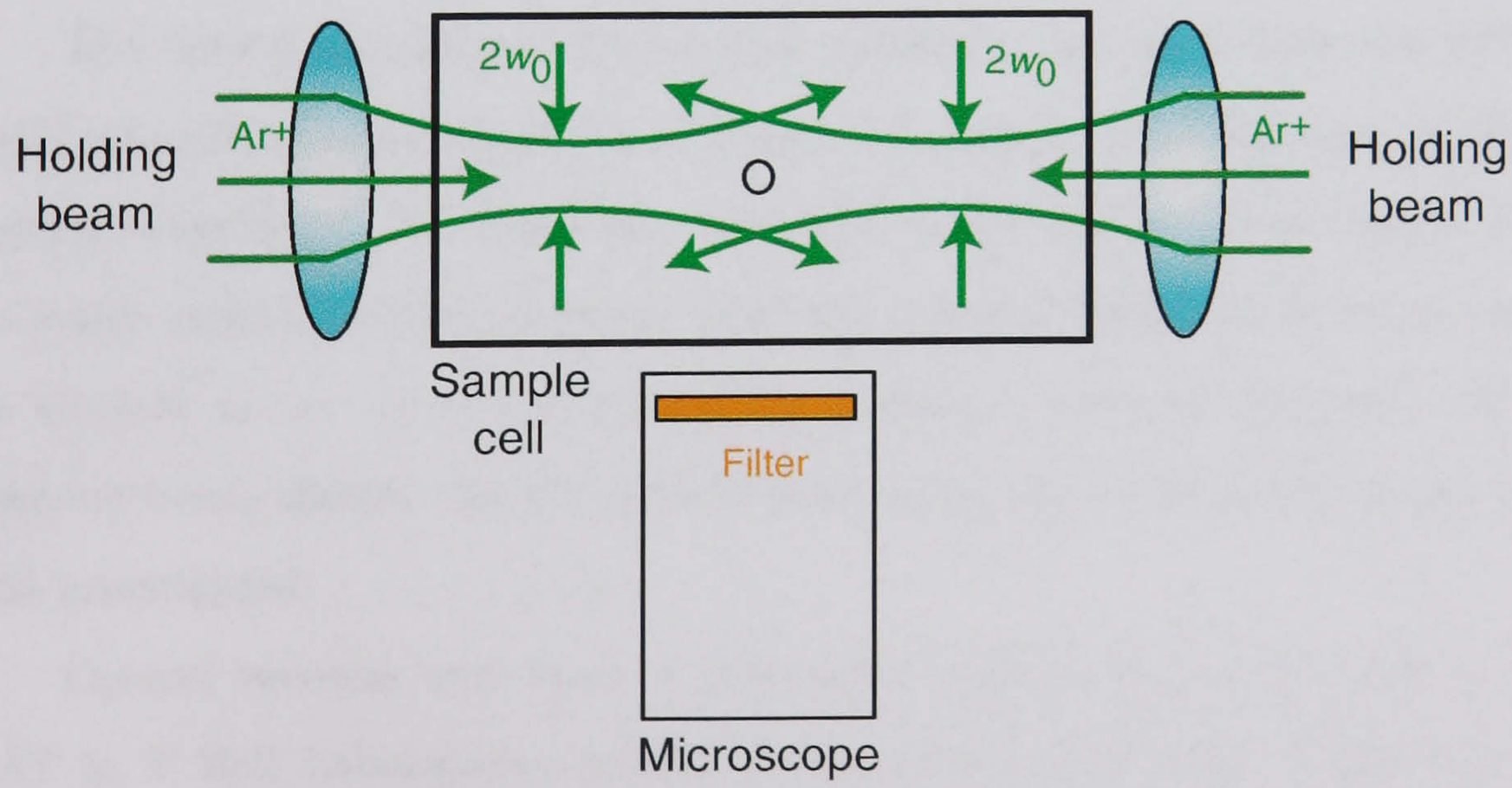

Figure 2.3: The trapping of a high index sphere using two equal and opposing TEM_{00} Gaussian beams. See Section 2.1.2 for more details.

These results enabled Ashkin to produce a stable optical potential well for high index particles using two opposing TEM_{00} Gaussian beams. These beams accelerated a particle towards the stable equilibrium point where the two beams met, see Figure 2.3.

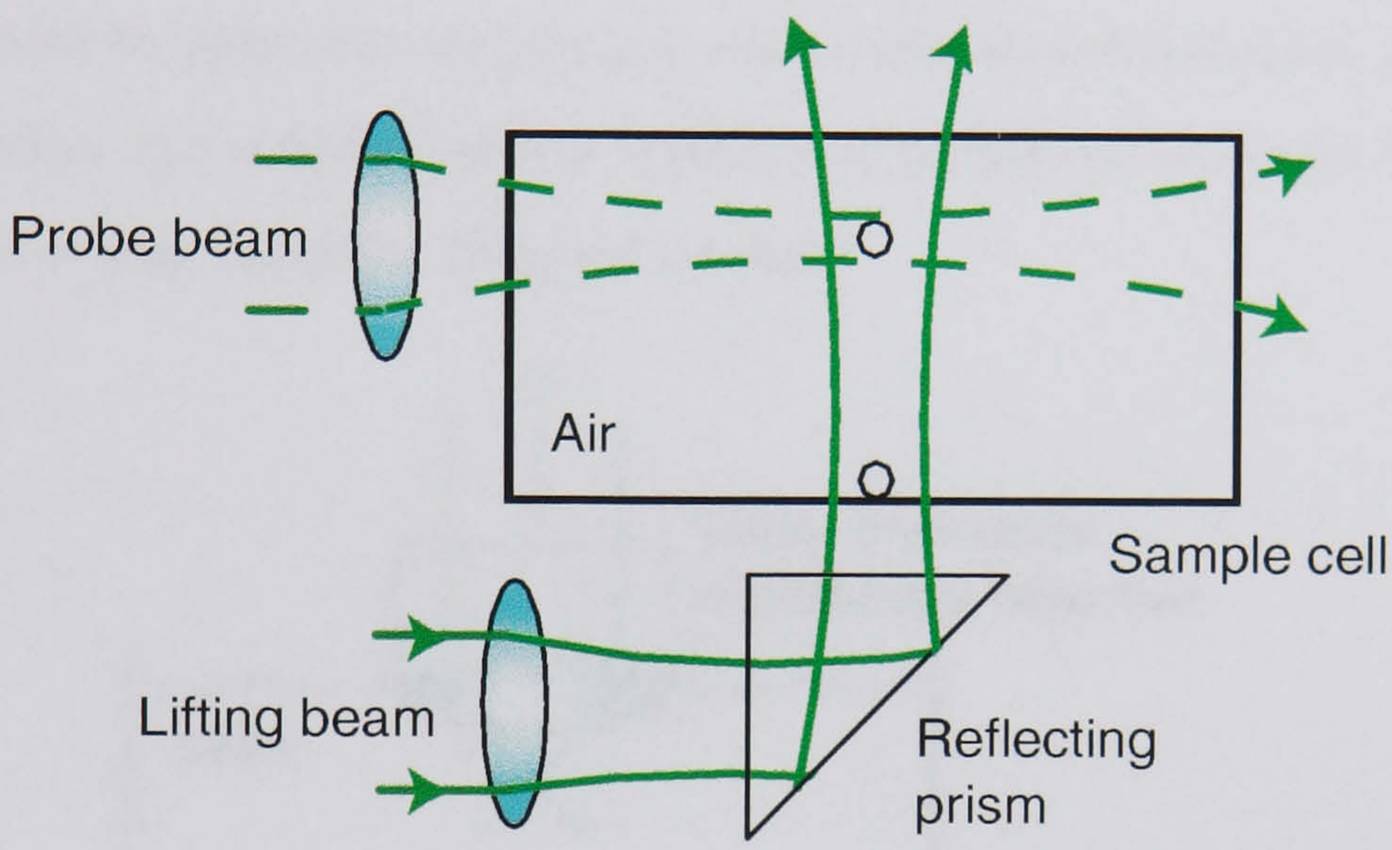

Figure 2.4: Levitation equipment. The lifting beam lifts a sphere to the probe beam where the strength of the trapping forces are studied, refer to Section 2.1.2.

The optical levitation of 20 μm glass spheres in air was achieved in 1971 [41] using the apparatus shown in Figure 2.4. Again, a TEM_{00} laser in the green, wavelength $\lambda = 514.5$ nm, was used to lift a micron sized sphere to a stable position above the beam waist in a manner analogous to balancing a football in the vertical stream of water from a burst fire hydrant. The second beam allowed the horizontal forces acting on the levitated sphere to be investigated.

Optical tweezers were born in 1986 when Ashkin and his co-workers at AT & T Bell Laboratories published the results from their "Single-beam gradient force optical trap for dielectric particles" [1]. Using a single, strongly focused argon laser beam, it was possible to stably trap particles ranging

from 25 nm to 10 μm in size in three dimensions, refer to Figure 2.5. This single beam trap was made possible by the fact that the highly focussed laser beam produced an axial gradient force greater than the scattering force, as explained in Section 2.2.1. Furthermore, it enabled a range of new possible applications by proposing trapping of other colloidal and biological particles, such as silica and polymer spheres to cells and viruses as well as for the atom trap that it was originally designed for [42].

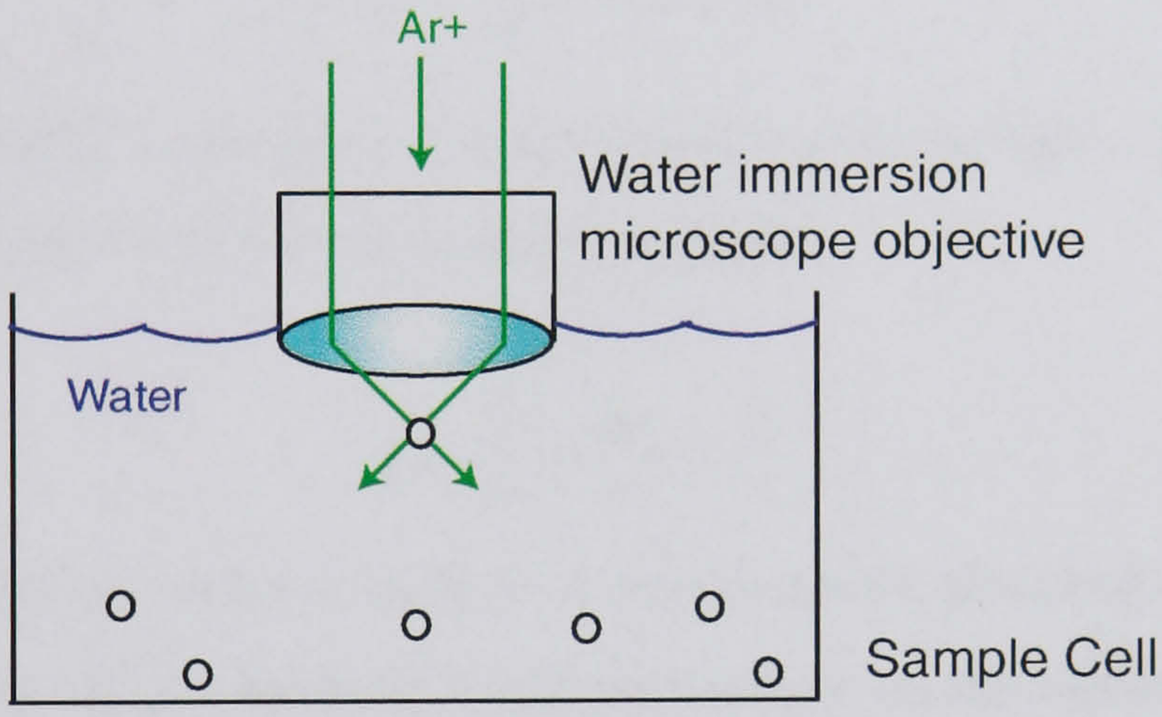

Figure 2.5: The first single beam gradient force radiation pressure trap as demonstrated by Ashkin in 1986 [1]. Rayleigh and Mie particles were trapped in water. See Section 2.1.2 for further details.

2.2 Optical tweezers

2.2.1 The trapping forces

The understanding of the forces underlying the principles of optical tweezers can be considered using two distinct explanations, one based on ray optics and the other on the electric field associated with the light.

In order to understand the ray optics approach to optical tweezers, it is useful to think of light as a stream of quantised bundles of energy called photons. Every photon carries energy, E, and momentum, p, which can be described by Equations 2.4 and 2.5. Ashkin [43] published a detailed analysis of the ray optics regime, with the central understanding based on the conservation of momentum.

$$E = h\nu = \frac{hc}{\lambda} = pc \tag{2.4}$$

where h is Planck's constant, ν is the frequency of the light, λ is the wavelength of the light and c is the velocity of light.

$$p = \frac{h}{\lambda} = \frac{h\nu}{c} = \frac{E}{c} \tag{2.5}$$

When a photon meets a surface, it can be either absorbed, transmitted, reflected, refracted or scattered, resulting in a force on the surface in question. If the photon is absorbed by a dielectric particle, momentum p is transferred from the light beam of power P to the particle. The incident momentum per second in a medium of refractive index n is given by nP/c [43]. This results in a reaction force F on the particle. The dimensionless quantity Q describes the efficiency of such an optical system and is given by

$$Q = \frac{cF}{nP} \tag{2.6}$$

where a Q value of 1 represents the case where all a photon's momentum is absorbed by an object. In typical optical tweezers systems, Q lies between 0.01 and 0.3 for dielectric, biological and metallic objects [5, 44, 45, 46]. Here, F is the force actually generated by the laser beam in the tweezers system.

The maximum possible force, F, an optical tweezers trap can exert on an object in a medium of refractive index n is given, upon rearrangement of Equation 2.6, by:

$$F = \frac{PnQ}{c} \tag{2.7}$$

In practise, the maximum force that the trap can exert is calculated by measuring the velocity v at which an object with diameter d in a fluid of viscosity η escapes. This is described by the Stokes drag force, F_{drag} as detailed below.

$$F_{drag} = 3\pi\eta dv \tag{2.8}$$

To calculate the Q value, the drag force F_{drag}, Equation 2.8, is set equal to F in Equation 2.7, and hence can be calculated using Equation 2.6. The drag force, Equation 2.8, does not apply when the sample is in a static position, but allows calculation of the force required to remove a particle from an optical trap by a fluid flowing past the particle, as demonstrated in Chapters 3.3.3 and 4.3.4.

Using a ray optics approach, it is possible to accurately describe the trapping mechanisms of optical tweezers incident on a Mie particle (particle diameter, d $\gg$ wavelength, λ). For a transparent, dielectric object, the acting forces primarily result from the light refracting through the object. As the light refracts, the corresponding change in photon momentum causes a reaction force on the object according to Newton's 2^{nd} and 3^{rd} laws:

Newton's 2^{nd} law: "The rate of change of momentum of a moving body is proportional to and in the same direction as the force

acting on it."

Newton's 3^{rd} law: "If one body exerts a force on another, there is a equal and opposite force, called a reaction, exerted on the first body by the second."

There are also forces generated from reflection and scattering off the object's surface. When the trapped object is suspended in a fluid of similar refractive index, these forces are suppressed and are, in general, small enough to be ignored.

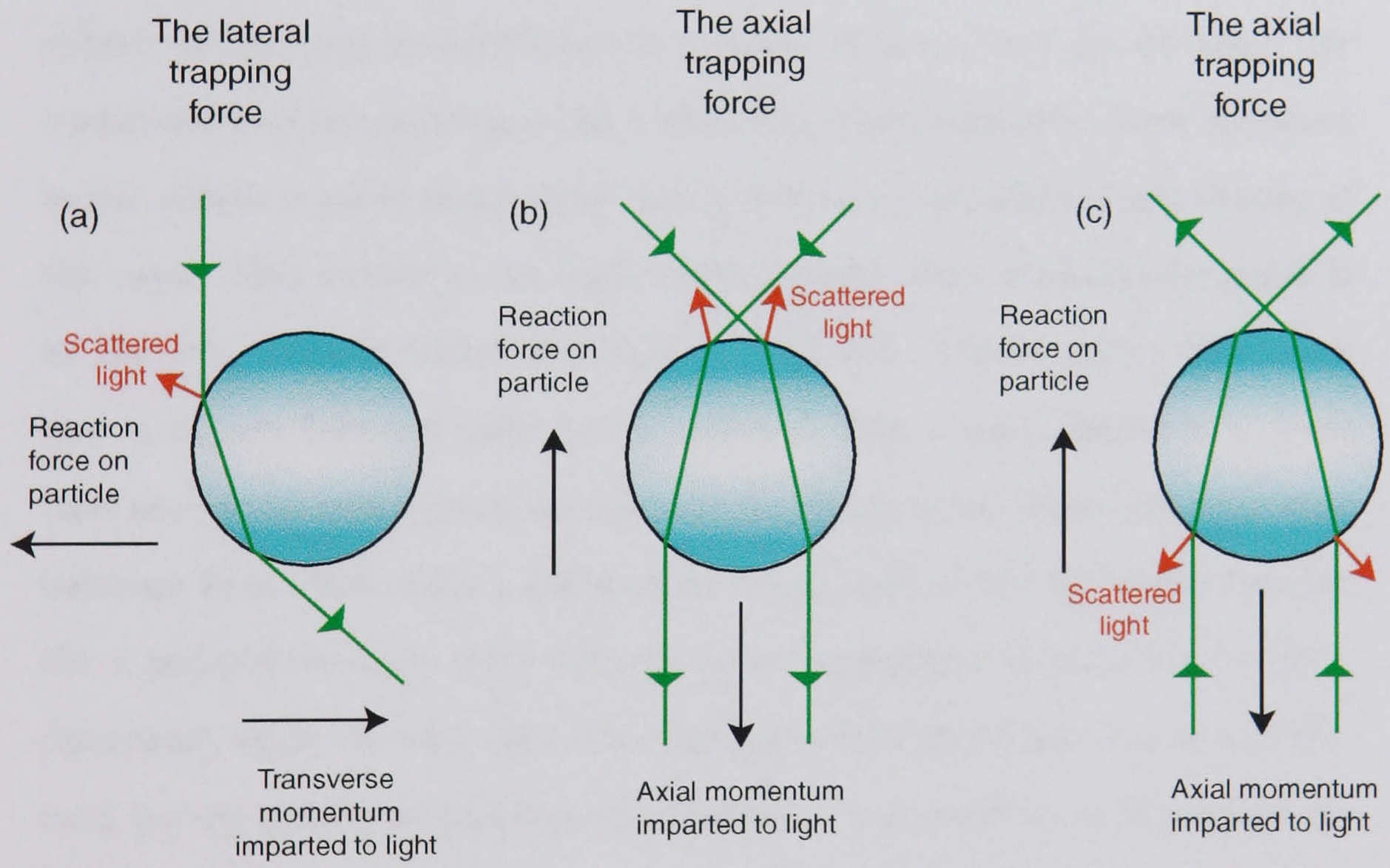

Figure 2.6: The axial and lateral forces responsible for trapping micron sized transparent spheres with a higher refractive index than the surrounding medium. See Section 2.2.1 for a more detailed explanation.

With reference to Figure 2.6, it can be seen that the gradient force always acts to move the centre of the sphere to the focus of the beam, whilst

the scattering force always acts in the direction of light propagation. Figure 2.6(a) shows that a dielectric object is drawn back towards the region of highest light intensity. Here the sphere is placed in a beam of light coming directly from above, with the most intense part of the beam incident of the left hand side of the sphere. The rays are bent by refraction at the interfaces where they enter and leave the sphere. A certain amount of reflection also takes place at these interfaces. All rays of light carry momentum. Before refraction by the sphere, all the rays carry momentum in the longitudinal direction and none in the transverse direction. However, upon exiting the sphere, the ray has an additional component of momentum to the right. By conservation of momentum in the x direction, these rays must have imparted to the sphere a momentum equal and opposite to the momentum change of the rays. This results in an equal and opposite force pushing the particle to the left, towards where the light is brightest. Figure 2.6(b) illustrates that a tightly focussed laser beam, incident from above, results in a force that moves the sphere back up towards the beam focus. Here, the light rays entering from above have a substantial component of lateral momentum (in the x and y directions) and relatively little longitudinal momentum (in the z direction), while the rays that leave the bottom of the sphere are nearly vertical having gained longitudinal momentum. By conservation of momentum in the z direction, the sphere will experience a force from these rays in the upwards direction. Momentum from the scattered rays acts downwards, so in this case the scattering and gradient forces act in opposite directions. In this case, the stable 3D trap position lies just below the focus of the beam where the gradient and scattering forces are in equilibrium. Figure 2.6(c) demonstrates what happens when the direction of light is reversed. Again,

the resultant force on the sphere acts to move the sphere up towards the focus and now the scattering and gradient forces have the same sign (acting in the same direction). It follows that, in this instance, the stable 3D trapping position is just beyond the beam focus.

The details in Figure 2.6 are only true when the refractive index of the sphere, n_1, is larger than that of the surrounding medium, n_2. If this situation is reversed, the particle acts like a diverging (as opposed to a converging) lens, and the object is pushed out of the beam as described in Section 2.1.2. The trapping of metallic particles also differs to that explained here and this is described in more detail in Chapter 3.

The ray optics approach gives accurate results for Mie particles. However, the forces acting on Rayleigh particles (i.e. particles with a diameter d less than λ) are better described using the electric field method, using the following equations [1].

$$F_{scat} = \frac{I_0}{c}\frac{128\pi^5 r^6}{3\lambda^4}\left(\frac{\left(\frac{n_1}{n_2}\right)^2 - 1}{\left(\frac{n_1}{n_2}\right)^2 + 2}\right)^2 n_2 \tag{2.9}$$

$$F_{grad} = -\frac{n_2^3 r^3}{2}\left(\frac{\left(\frac{n_1}{n_2}\right)^2 - 1}{\left(\frac{n_1}{n_2}\right)^2 + 2}\right)\nabla E^2 \tag{2.10}$$

$$F_{gravity} = -\frac{4}{3}\pi r^3(\rho_1 - \rho_2)g \tag{2.11}$$

where I_0 is the intensity of the incident light, n_1 is the refractive index of the particle, n_2 is the refractive index of the solution, r is the radius of the particle, ∇E is electric field gradient, ρ_1 is the density of the particle, ρ_2 is the density of the solution and g is the acceleration due to gravity.

In the electromagnetic approach to trapping, the object is treated as a small dielectric particle. The electromagnetic field polarises the dielectric particle and orients the charges in the direction of the electric field E. It can be shown [1, 47] that a dipole in a non-uniform electromagnetic field will experience a force proportional to the square of the gradient of the electric field ∇E^2, given by Equation 2.10. Therefore, one requirement for achieving trapping is that the object to be trapped can be polarised.

It is interesting to note that both the gradient and scattering forces are linearly proportional to the light intensity I_0. As the gradient force is required to exceed the scattering force in order to create a 3D trap, it is not enough simply to increase the laser power in an effort to increase the trapping potential. Instead, the gradient force can be maximised by focusing the laser beam as tightly as possible through a high numerical aperture microscope objective lens. Furthermore, the scattering force acts in the direction perpendicular to the wavefronts, causing the object to be pushed in the direction of the light propagation, whilst the gradient force acts to draw the object towards the region of highest intensity. It can also be seen that the scattering force $F_{scat} \propto r^6$ and the gradient force $F_{grad} \propto r^3$, consequently scattering forces are less of a problem for smaller particles.

For a 1.5 μm diameter silica particle trapped in optical tweezers, F_{grad} is of order $10's\ pN$, F_{scat} is of order of $pN's$ and $F_{gravity} = 10^{-14}N$. The direction of each force in inverted optical tweezers is illustrated in Figure 2.7. The scattering force acts in the direction of the laser beam propagation, the gradient force acts to draw the particle into the region of highest light intensity (i.e. the focus) while the force of gravity always acts in a downwards direction. When a particle is stably trapped, the vectorial sum of all the forces balance.

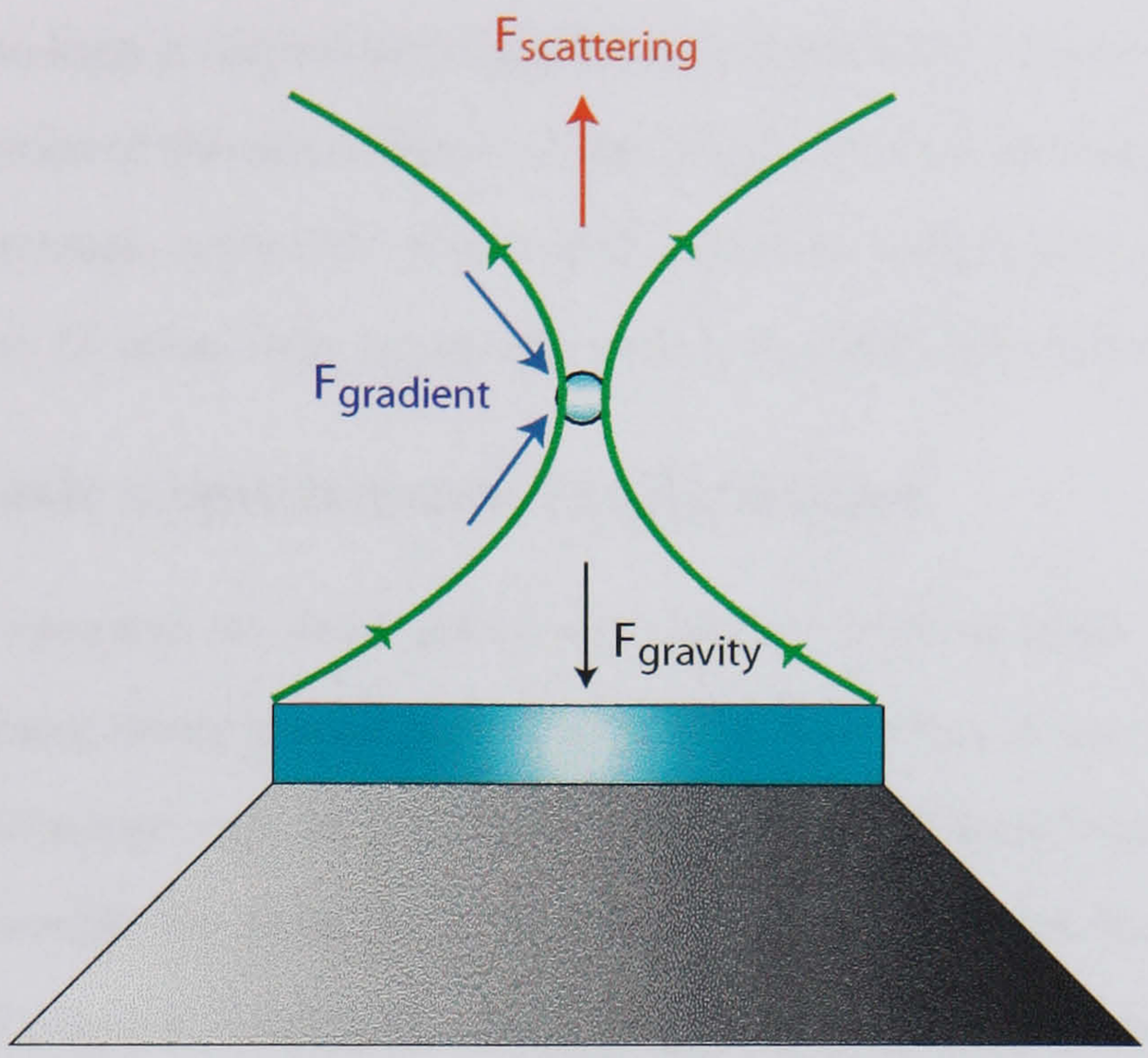

Figure 2.7: When the trapping laser beam is incident from below (inverted microscope), the scattering force acts in the direction of the laser beam propagation, the gradient force acts to draw the particle into the region of highest light intensity (i.e. the focus) while the force of gravity always acts in a downwards direction. Section 2.2.1.

The force of gravity, Equation 2.11, always acts downwards, although it is often neglected in many calculations as its effect is small, compared to the gradient and scattering forces, for polystyrene ($\rho_1 = 1050\ kg/m^3$) or latex spheres, ($F_{gravity} = 10^{-16}N$). Its effect is more prominent when higher density, (e.g. silica, $\rho_1 = 2600\ kg/m^3$) spheres are trapped ($F_{gravity} = 10^{-14}N$).

It should be noted that some particles, such as silver, have a complex refractive index $n = n' + in''$ which means that the particle is partially absorptive, i.e. it only partially transmits the light resulting in a significant increase in the scattering force. Ultimately, if the light scattering from the

particle is too high it cannot be trapped in a conventional optical tweezers. So for two particles of the same diameter and trapped under identical conditions in optical tweezers, a particle with a real refractive index (such as silica) will have a higher Q value than a particle with a complex refractive index.

2.2.2 Basic experimental configuration

For optical tweezers to work effectively, several criteria must be satisfied. Firstly, the laser beam should pass through the back of an objective lens such that the microscope can work normally. Secondly, the laser beam should fill or slightly overfill the back of the aperture of the objective lens to achieve the smallest possible focal spot, and therefore the largest electric field gradient. Lastly, the beam must be brought to a diffraction-limited focus at the specimen plane where the sample is viewed. Figure 2.8 shows a schematic diagram of one experimental setup which can be used to satisfy these criteria. Figure 2.9 is a photograph of the experimental setup described in Figure 2.8.

The conjugate planes of the optical tweezers allow the laser beam to be steered accurately through the setup, as described in Section 2.2.3.

2.2.3 Beam steering in optical tweezers

For optical tweezers to operate properly, it is vital that the collimated laser beam passes through the centre of all lenses and overfills the back of the microscope objective as described in Section 2.2.2. This can be achieved using the two beam steering mirrors as illustrated in Figure 2.10. The first beam steering mirror controls the entrance angle to the back of the aperture whilst the second beam steering mirror allows fine tuning of the position of the beam in the diffraction limited sample plane.

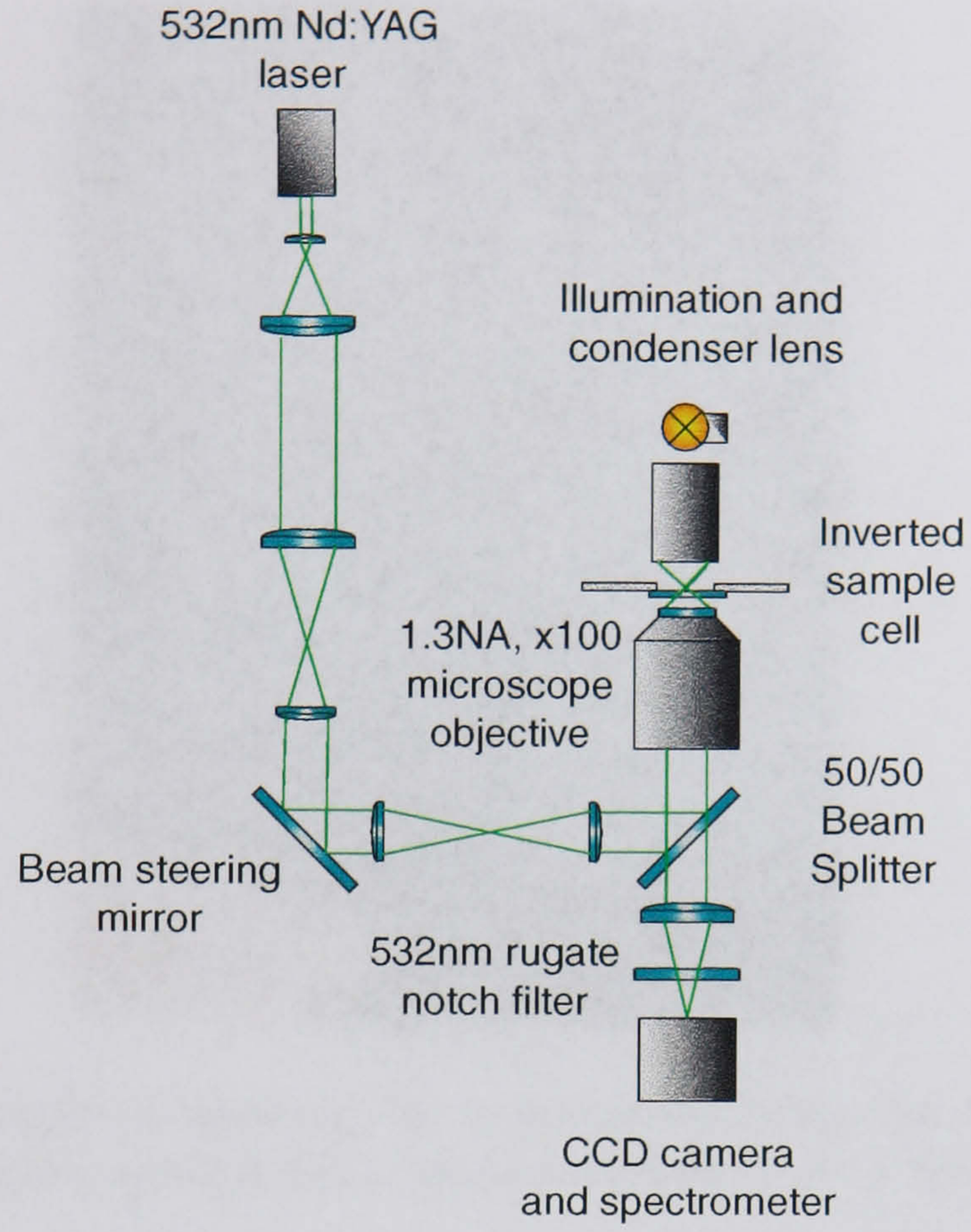

Figure 2.8: Figure showing one basic experimental apparatus setup for the optical tweezers used during this research, as described in Section 2.2.2.

An angular shift, α, at the first beam steering mirror causes a lateral shift, ΔC, of the collimated laser beam at the entrance pupil of the microscope objective, plane C, whilst an angular shift, β, at the second beam steering mirror results in a lateral shift, ΔD, of the focussed beam within the sample cell at plane D. The relative transverse movement of the laser beam within the sample plane depends on the values of the focal lenses in the telescope as detailed below.

By applying the general lens formula $1/s + 1/s' = 1/f$ [48] to the system, it can be shown that the lateral movement ΔD caused by an angular shift of β at plane B is represented by:

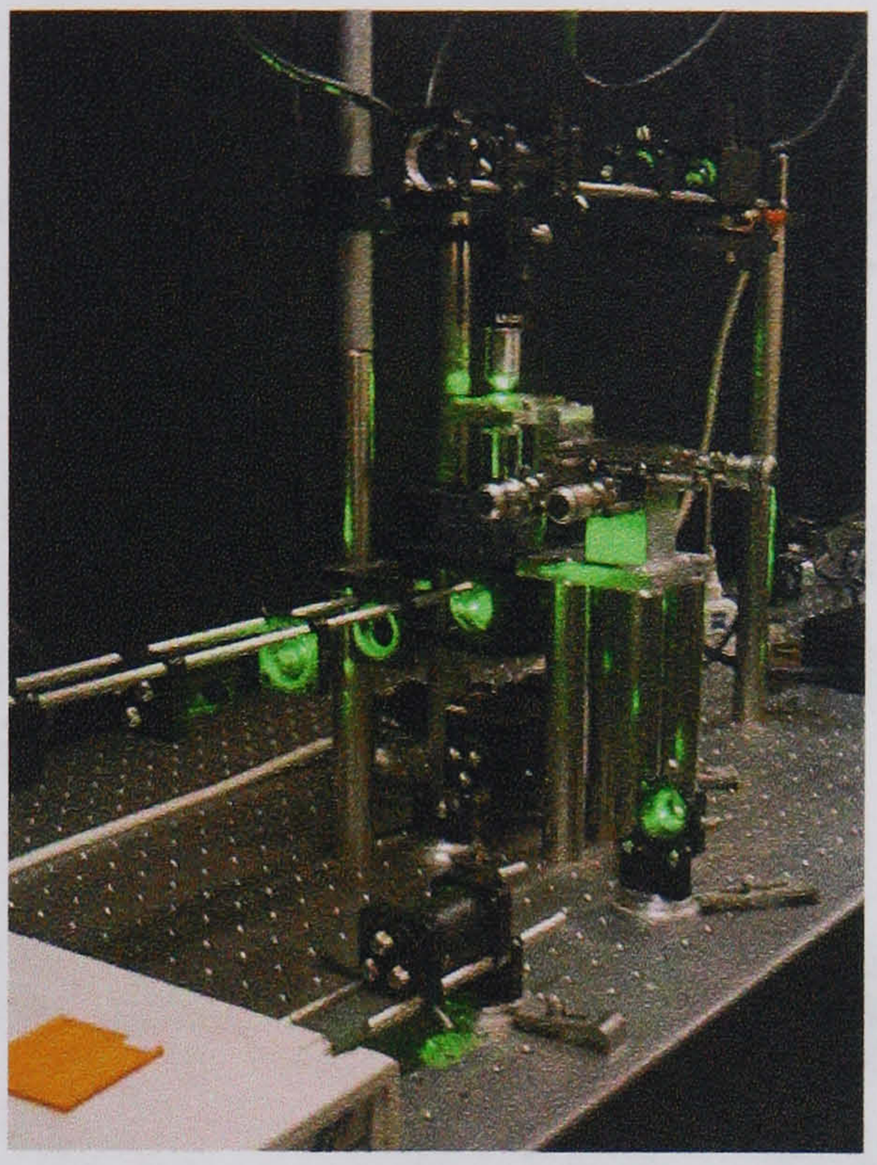

Figure 2.9: Photograph showing the experimental setup for the beam focussing and trapping using optical tweezers as described in Section 2.2.2.

$$\Delta D = \frac{f_1 f_3 \beta}{f_2} \tag{2.12}$$

Following similar principles, we find that the relationship between an angular movement of α at plane A and the lateral movement ΔC at plane C is given by the equation below. Also refer to Figure 2.10.

$$\Delta C = \frac{f_1}{f_2} d\alpha \tag{2.13}$$

In the optical tweezers setup used in this work, the telescope was arranged so that a real image was formed at the focal point of both lenses, resulting in the image rays leaving the second lens, f_2, as a collimated beam with a virtual image at infinity. If the real image was not formed at the focal point

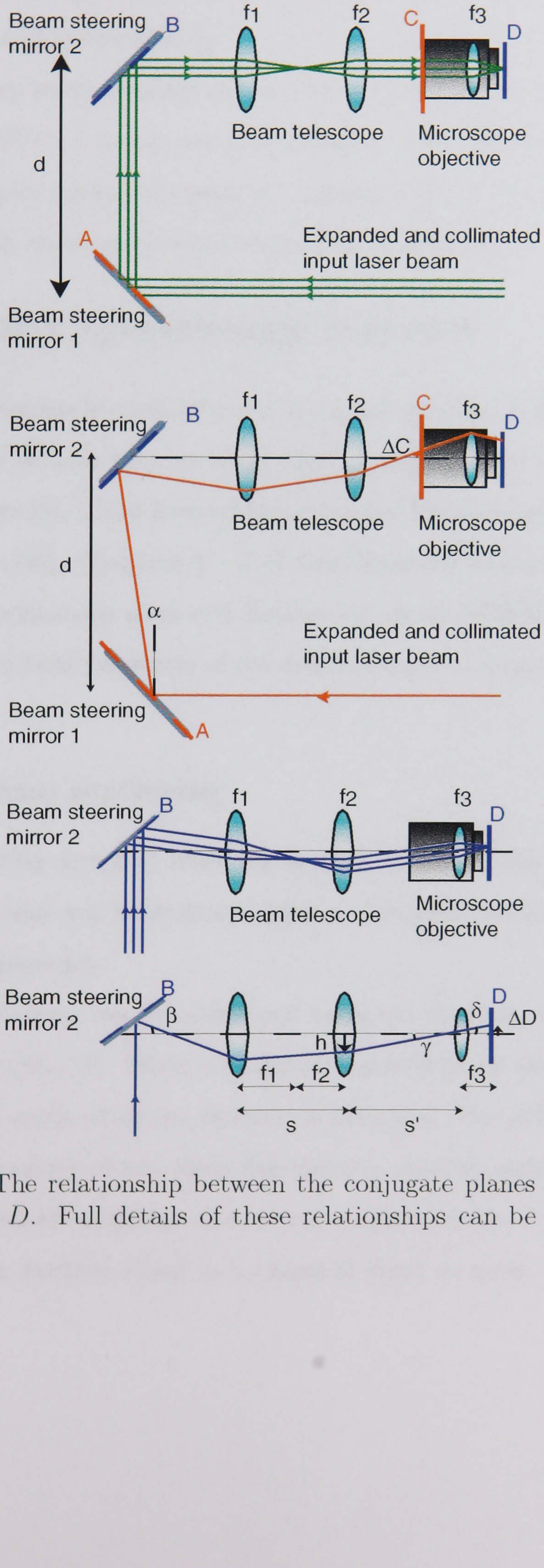

Figure 2.10: The relationship between the conjugate planes A and C and planes B and D. Full details of these relationships can be found in Section 2.2.3.

of both the f_1 and f_2 lenses, there is no longer a collimated beam entering the microscope objective lens, f_3.

A collimated beam always gives one trap in the objective's focal plane and nothing else. When a trap is put into different z positions, as demonstrated using holographic optical tweezers in Chapters 6 and 7, the beam entering the back of the objective is either converging or diverging.

2.3 Raman spectroscopy overview

Raman spectroscopy is a well reviewed technique [49, 50, 51, 52, 53]. Raman and resonance Raman measurements have previously been combined with optical tweezers [54, 55] as have surface-enhanced Raman scattering (SERS) measurements [56]. Chapters 3 – 5 of this thesis are concerned with combining surface-enhanced resonance Raman scattering (SERRS) with optical tweezers, and a brief discussion of the different types of Raman scattering is presented.

2.3.1 Raman scattering

Raman scattering was first observed in 1928 by C. V. Raman [57], who demonstrated that not all scattered light is elastically scattered i.e. it can be shifted in frequency.

Raman scattering can be understood using the classical approach to the theory of light [58, 59]. When a molecule is placed in an electric field, the electron cloud surrounding the molecule is polarised. The polarisability of a molecule is a measure of how easily this electron cloud is moved or distorted. As light consists of oscillating electric and magnetic fields, it can cause the position of the electron cloud in a chemical bond to move. This in turn

induces an electric dipole. Light is re-emitted from this dipole; this is called scattering. The polarisability of the molecule can be described by

$$\mu = \alpha E \tag{2.14}$$

where μ is the induced dipole moment, α is the polarisability and E is the electric field.

Every type of molecule is unique, and therefore has a unique polarisability. This unique polarisability means that each molecule also has unique Raman scattering properties, so that the emission spectrum is a characteristic "fingerprint" of the molecule under investigation.

In terms of energy levels, Raman scattering involves the excitation of a photon from the ground state to a "virtual" energy state that lies at an energy less than the first "real" electronic state. In a real absorption process, energy is conserved resulting in the system being in a discrete state. When energy is transferred between the photon and the molecule the resulting state is described as a "virtual state" [59]. The virtual energy level can be thought of as a perturbation or distortion of the electron distribution and opens up the possibility of spectroscopic transitions other than direct absorption. Scattering processes, unlike direct absorption, do not require incident photons to have an energy corresponding to an electronic transition of the system.

In Raman spectroscopy, the sample is irradiated by a laser beam of frequency ν_0. The difference in energy between the ground state and a virtual energy level, E, irradiated by this frequency, ν_0, is related through the equation [58]

$$E = h\nu_0 \tag{2.15}$$

where h is Planck's constant.

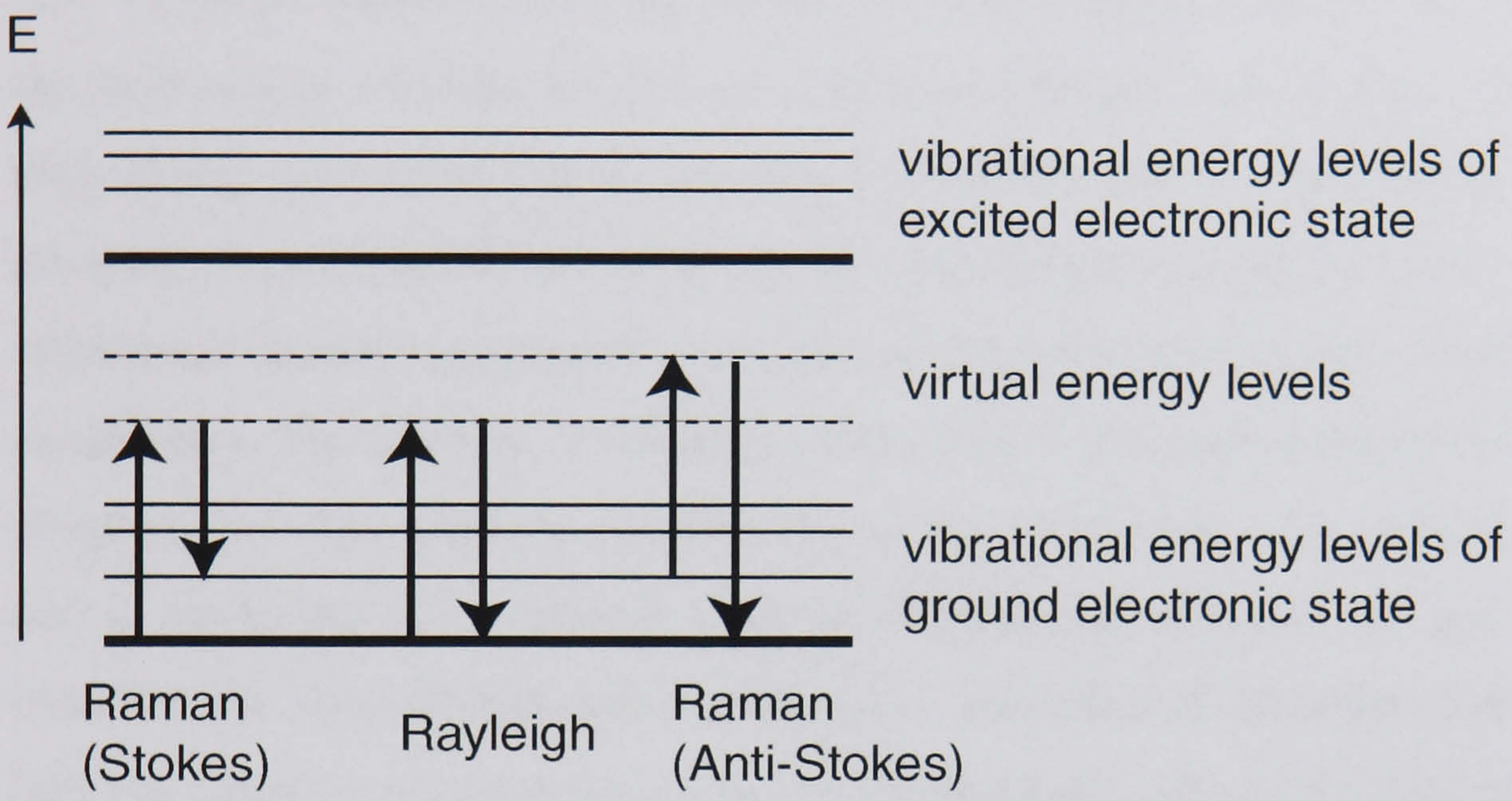

Figure 2.11: Energy level diagrams of the different processes allowed in Raman scattering, namely Rayleigh scattering, Stokes scattering and anti-Stokes scattering. These processes are described in Section 2.3.1.

Figure 2.11 shows the transitions that are possible in Raman scattering. Raleigh scattering is the simplest case where the scattered light emitted by a molecule has the same frequency, ν_0, as the excitation light, ν_0. This is also known as elastic scattering. Raman, or inelastic, scattering is where the frequency of the scattered light is different from the incident light ν_0 and it happens for only a small fraction of light (approximately 1 in 10^7 photons [60]). Two types of Raman scattering exist, and they are defined as Stokes and anti-Stokes scattering. Stokes Raman scattering occurs when a photon is excited from the lowest vibrational energy level in the ground electronic state to the virtual energy level by the exciting frequency ν_0. This excited

molecule then relaxes to an excited vibrational energy level of the ground electronic state with the emission of a photon with a new frequency of (ν_0-$\Delta E/h$) and a wavelength that is longer than that of the illuminating radiation. In Stokes Raman scattering, energy is transferred from the photon to the molecule (i.e. inelastic scattering). Anti-Stokes Raman scattering occurs when energy is transferred from the molecule to the photon (also an inelastic process). Here a photon is excited by the irradiating frequency ν_0 from a vibrational excited energy level in the ground electronic state to the virtual energy level. The molecule or transitions then relax to the lowest energy level of the ground state with the emission of a photon of frequency (ν_0+$\Delta E/h$) and a wavelength that is shorter than the illuminating radiation. As governed by the Maxwell-Boltzmann distribution, described by Equation 2.16 [58], the majority of molecules are in the lowest vibrational energy level of the ground state at room temperature. For this reason, Stokes scattering is generally dominant over anti-Stokes scattering.

$$\frac{N_n}{N_m} = \exp \frac{-\Delta E}{kT} \tag{2.16}$$

where N_m and N_n are the number of molecules in the ground energy states m and n respectively, ΔE is the difference in energy between the two vibrational energy levels, k is Boltzmann's constant (1.3807×10^{-23} JK^{-1}) and T is the temperature. Raman scattering depends linearly on the number of molecules probed [53].

The difference in energy between the incident and the scattered light corresponds to the difference in energy between the two vibrational energy levels involved in the Raman process. These bands are characteristic of a certain molecule and can be used to gain molecular (including energetic and

structural) information. Note that these frequency shifts are independent of the frequency of the excitation light, i.e. Raman spectra can be observed using a laser at any wavelength.

Raman scattering is different to fluorescence. Fluorescence involves an absorption/emission process where, upon the absorption of a photon, the molecule can move to an excited electronic (or real) state. During relaxation, the molecule emits radiation (fluorescence) and this occurs on a time scale of 10^{-9}s [58]. Raman, on the other hand, is the result of a photon-molecule collision which occurs on a near instantaneous timescale of 10^{-14}s [58].

2.3.2 Resonance Raman scattering

If a sample is irradiated with an energy that corresponds to an electronic absorption maximum of the molecule at the virtual energy level, specific Raman bands can be enhanced by a factor of 10^3 - 10^4 compared to normal Raman scattering. As the energy of an incident photon approaches that of an electronic transition energy associated with the material, the intensity of the scattering is enhanced. This enhancement increases rapidly as the energy of the incident photon approaches that of an electronic transition [59]. The molecule is said to be in resonance. In other words, only molecules with an electronic absorption maximum corresponding to the excitation frequency of the laser are likely to be enhanced. Resonance Raman should not be confused with fluorescence; fluorescence is an absorption/emmission process while resonance Raman is the result of a photon/molecule scatter mechanism.

2.3.3 Surface enhanced Raman scattering (SERS)

Surface enhanced Raman scattering (SERS) is an enhancement of the normal Raman scattering by 5 - 6 orders of magnitude [61, 62] and is achieved

when the molecule of interest is adsorbed onto certain metal surfaces. The mechanisms behind SERS are still under debate, although it is thought to be a combination of an electromagnetic enhancement [50, 52] and a chemical enhancement [51].

Electromagnetic enhancement is where the effective electric field magnitude is made larger and is due to the interaction of the metal surface and the excitation laser. This in turn results in the molecule radiating an amplified Raman field. The most significant contributor of electromagnetic enhancement comes from surface plasmons. A surface plasmon is generated when the electron cloud in a metal is excited and restricted to the surface of the metal. At the surface plasmon resonant frequencies, the electron cloud can move easily and produces a large oscillation in the local electric field strength [58]. The surface plasmon frequency depends on the feature size of the metal surface features as described in Section 2.3.7. When the metal surface is smooth, the surface plasmon is a wave that is confined to the surface and it radiates in a direction parallel to the surface ($\ll$ 10 nm). However, when the metal is rough, on the nm scale, the plasmons are localised within the roughened surface and can radiate in directions both parallel and perpendicular to the surface [51]. For this reason, a rough metallic surface is needed to support SERS. Furthermore, only a small number of metals have a plasmon excitation at visible frequencies; the most common metals used are silver [63, 64, 65], gold [66, 67, 68] and copper [69, 70].

In chemical enhancement, the molecular polarisability is changed and is thought to be as a consequence of adsorbing molecules onto the surface of the metal [71, 72, 73, 74]. The binding of the analyte to the metal surface changes the polarisability of the adsorbate and hence changes the Raman

signal. As a result, the Raman and SERS spectra of the same analyte can differ substantially. SERS requires the molecule to be in close proximity to the metal surface, so the chemical enhancement is thought to arise from the broadening of the energy levels or from new, intermediate resonant levels created near the metal surface. The charge-transfer theory is the most accepted method for describing this effect [74]. For example, transitions are possible between the electrons in the highest occupied molecular orbit of the metal and the lowest unoccupied molecular orbit of the adsorbed molecule. An electron-hole pair is produced by an incident photon, with the hole residing in the metal. If during the residence time the molecule relaxes into a different vibrational state, the recombination of the electron-hole pair results in a Raman shifted photon. Hence the Raman scatter in SERS is as a result of electron/adsorbate interaction as opposed to photon/adsorbate interaction in normal Raman. However, opinion is that the electromagnetic enhancement is greater than the chemical enhancement [50].

The SERS enhancement is related to an electromagnetic resonance effect that depends markedly upon several factors [52, 50] including the shape, roughness and surface geometry of the metal substrate [75, 76] the orientation of the molecule on the metal surface [77] and molecule-metal separation [77, 78, 79]. Since SERS is primarily due to an electromagnetic effect, which decreases with distance from a point source, it follows that molecules a distance away from the metal surface may also experience an enhancement. Studies of molecules interacting with small metal spheres, with a radius r, suggest that the SERS enhancement of the emitting molecule changes depending upon the proximity of the adsorbed molecule a distance d from a metal surface with a $(r/r+d)^{12}$ dependence [50].

The success of the electromagnetic model [50] in accounting for a large number of SERS observations encouraged investigations into the effect of enhanced electromagnetic fields on molecules near rough metal surfaces on phenomena such as enhanced absorption, fluorescence and photochemistry [80, 81, 82, 83] as it was predicted that there should be enhanced absorption and luminescence of molecules adsorbed onto metal surfaces that have electronic transitions close to the plasma frequency of the metal.

2.3.4 Surface enhanced resonance Raman scattering (SERRS)

Surface enhanced resonance Raman scattering, (SERRS), was first reported in 1983 by Stacy and Van Duyne [84] and is usually considered to be a combination of resonance Raman scattering, described in Section 2.3.2, and surface enhanced Raman scattering, (SERS) described in Section 2.3.3. SERRS occurs when a chromophore has an electronic absorption maximum close to the excitation wavelength, and which also coincides with the surface plasmon resonance. This can lead to enhancements as large as 10^{10} to 10^{12} compared to Raman scattering, or 10^3 to 10^4 compared to SERS [65, 85, 86, 87, 88]. Furthermore, SERRS appears to be much more sensitive than even fluorescence [89, 90].

2.3.5 Advantages of Raman spectroscopy

Raman, resonance Raman, SERS and SERRS are all capable of providing structural and vibrational information of many molecules. Raman bands can be selectively enhanced using resonance Raman, SERS or SERRS and single molecule detection is possible using SERRS. Spectra are viewed through relative wavenumbers and molecularly specific spectra are observed. The peaks

in a Raman spectrum are well defined and distinct from each other which allows the identification of several different analyte molecules simultaneously.

2.3.6 Converting between wavelength and Raman shift

Spectroscopists favour plotting graphs in terms of the Raman shift (relative wavenumbers to the exciting laser wavelength), $\Delta\nu$, measured in cm^{-1} as opposed to the wavelength measured in metres (m). The value of the Raman shift is calculated by taking the inverse of the laser wavelength (in cm) minus the inverse of the Stokes Raman shifted wavelength (in cm). The relative wavenumber shift for a particular molecule is constant no matter what excitation wavelength is used. For instance, if a laser of 532 nm wavelength is used for the excitation, this corresponds to a wavenumber of 18797 cm^{-1}. If our main Raman peak appears at a shift of 1370 cm^{-1}, this would equate to a wavenumber of 17427 cm^{-1} (i.e. 18797 cm^{-1} - 1370 cm^{-1}) which is equivalent to 574 nm, i.e. a shift of 42 nm from the excitation light. Any Raleigh scattered light, or incident laser light, will have a wavenumber of 0 cm^{-1}.

2.3.7 Silver plasmon resonances in nanoparticles

The wavelength of the maximum peak in a scattering cross section, λ_{max}, changes with the size of the particle as dictated by Mie theory [91, 92]. Typically the value of λ_{max} increases with increasing particle diameter and produces broader scattering bands.

For silver, typical values of λ_{max} are 390 nm for 20 nm diameter particles up to 445 nm for 80 nm diameter particles. For particles with diameters larger than 100 nm, two peaks appear in the light-scattering spectrum. For particles of 120 nm diameter, λ_{max} = 530 nm increasing to a value of λ_{max}

580 nm for 140 nm diameter. Beyond this particle diameter, λ_{max} starts to decrease back down to a value of λ_{max} 490 nm for 300 nm diameter particles [91]. These values correspond to resonance energies of approximately 3.1 eV for 20 nm diameter particles and 2.1 eV for 140 nm diameter particles.

2.4 Conclusion

Optical tweezers have proved useful in a wide variety of topics since their introduction as an atom trap [42] in 1978. They have been used in applications as diverse as manipulating biological materials to trapping metallic particles. Further uses have been for manipulating multiple beads in microfluidic channels in order to produce pumps and valves. Previous work on the trapping of metallic particles is discussed in Chapter 3. The more recent development of holographic optical tweezers has further advanced this technology and resulted in new applications which are mainly involved in the 2 and 3 dimensional patterning of surfaces and the simultaneous, multiple trapping of many objects. These applications are discussed in Chapter 7.

This thesis starts to explore some of these new applications, including the ability to trap metallic coated particles and to show that these metal particles are particularly suited to spectroscopic (SERRS) interrogation and finally, the use of holographic optical tweezers to create permanent microstructures.

Chapter 3

3D optical trapping of partially silvered microparticles

The stable three dimensional optical trapping of micron sized silica particles, partially coated with silver, using a focussed TEM_{00} laser beam is demonstrated. Spheres with different amounts of silver on their surface were investigated. It was found that, when only a small amount of silver was present on the surface of the sphere, stable 3D trapping was readily achieved. However, as the amount of silver covering the sphere surface increased, as measured using transmission electron microscopy (TEM), the force of the laser beam became repulsive, with the majority of the light reflecting back off the sphere surface. In this regime the spheres were more difficult to trap. Experiments investigating the transverse trapping efficiencies of the partially silvered particles, and an observation of how readily beads with differing amounts silver trapped, were made. This, in turn, was compared to the amount of silver present on the surface of the sphere. It is shown that these new particles were trapped in a similar manner, with comparable efficiencies, to that of a dielectric particle whilst also retaining some of the interesting properties of true metallic particles.

3.1 Introduction

For dielectric objects, the trapping mechanism for optical tweezers arises due to the extremely high gradient force in the electric field that is produced near the focus of the beam, as described in Chapter 2.

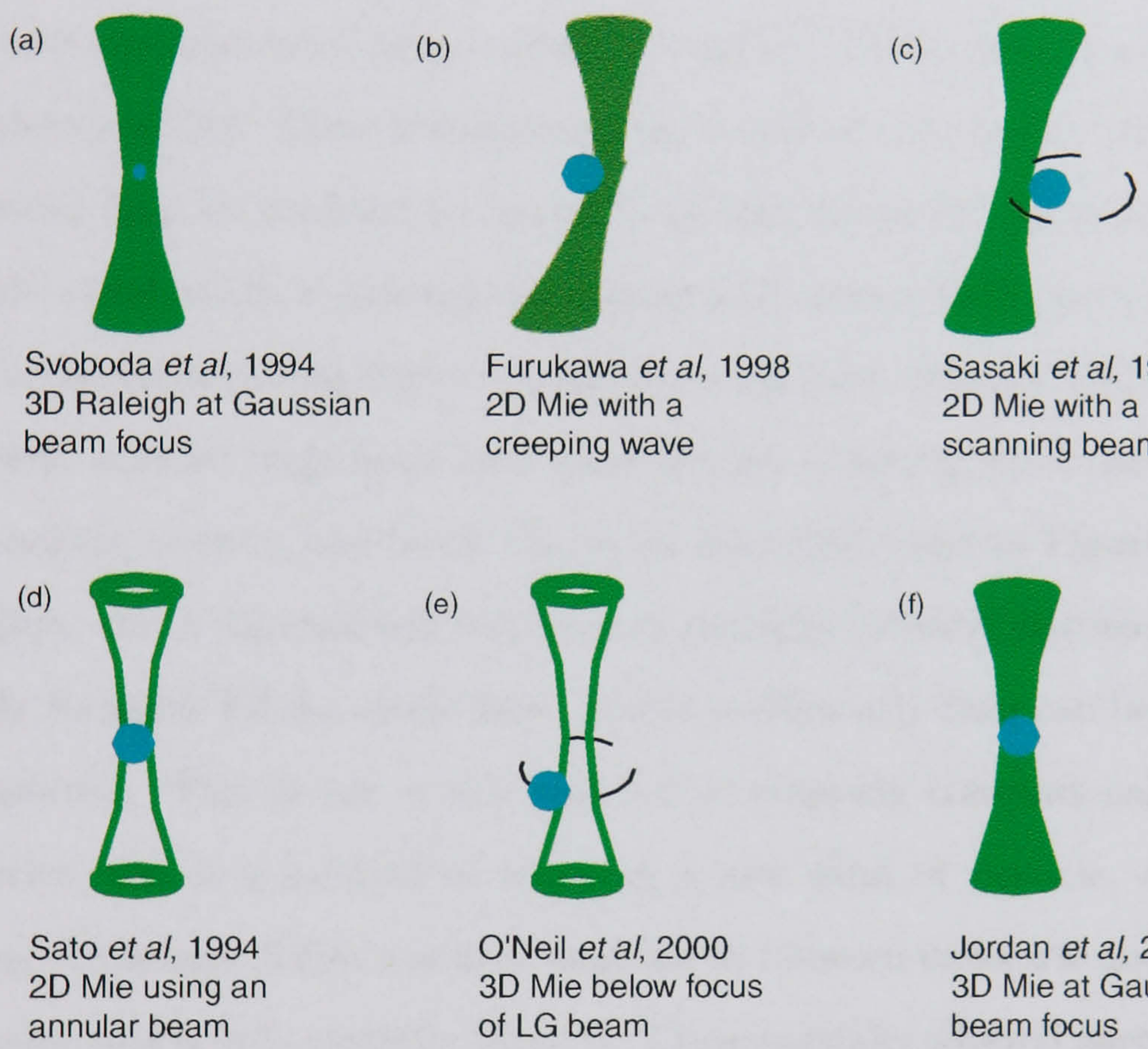

Figure 3.1: Different methods for trapping metallic particles. (a) Rayleigh particles trapped in 3D at the focus of a Gaussian beam, (b) Mie particles trapped in 2D by a surface plasmon wave, (c) Mie particles trapped in 2D by scanning and (d) annular beams, (e) 3D trapping by light scattering around and below the focus of a Laguerre-Gaussian beam and (f) 3D trapping of partially silvered microspheres at the beam focus of a Gaussian beam. See Section 3.1 for a full explanation.

The trapping of metallic spheres proves to be more difficult due to increased scattering forces from their highly reflective surface. In the majority of cases, these forces are greater than the gradient force and the focussed

laser beam repels the metallic sphere away. A variety of methods have been employed to overcome this problem. Metallic Rayleigh ($d \ll \lambda$) particles [93] have been trapped in 3 dimensions using a standard Gaussian beam. In this size regime, the scattering forces are similar for both dielectric and metallic samples. Trapping of metallic Mie ($d \gg \lambda$) particles in 2 dimensions has also been demonstrated using a rapidly scanning TEM_{00} laser beam [10] and annular rings [38]. These methods appear to exploit the repulsive force of the scattered light to produce an optical cage that keeps the particle confined. On the other hand, 2 dimensional trapping of micron sized particles due to attractive forces arising from creeping waves has been achieved [94] and, most recently, annular rings have been used to trap a micron sized particle, in 3 dimensions, outwith and below the beam focus [31], refer to Figure 3.1.

Here, the 3 dimensional trapping of partially silvered particles using a highly focussed TEM_{00} mode laser, and how efficiently they can be trapped, is reported. This is not a new method of trapping conventional metallic particles, but is a method of trapping a new kind of particle, developed during the course of this research, that lies in between dielectric and metallic particles, and is only partially silvered. These partially silvered particles were trapped using a mechanism similar to that of a dielectric particle whilst being able to retain some of the characteristics associated with metallic particles. One attraction for using metallic particles is that they can be used to enhance spectroscopic signals, generated as a consequence of molecular and electro-optical interactions at the surface of the bead, refer to Chapters 4 and 5.

3.2 Experimental setup and materials

3.2.1 Optical tweezers setup

The optical tweezers and associated microscope was based upon an infinity-corrected Zeiss Plan-Neofluar oil immersion objective lens (Zeiss, UK), with a numerical aperture of 1.3 and a magnification of $\times 100$, configured in an inverted geometry, allowing easy access to the sample plane as shown in Figure 3.2. The trapping laser beam was a frequency doubled Nd:YAG ("Excel", Photonics Solutions, Germany), which emitted at 532 nm with a variable output power of up to 1.5W. The sample cell consists of a metal slide 3 mm thick, 75 mm long and 25 mm wide, with a circular sample space of diameter 1 cm. A cover slip (Thickness No. 1, VWR International, UK) was adhered onto one side to create the sample chamber. The sample cell was mounted on a piezoelectric (PZT) stage (Piezosystem Jena Inc., Germany), which allowed 100 microns of travel in 3 dimensions and was controlled using a TTi DG 230 frequency generator (RS components, UK). All trapping in this Chapter was performed using approximately 100 mW, giving 20 mW in the trapping plane, as measured using a Newport Model 1815-C power meter (Newport, UK). The laser beam was expanded, collimated and projected onto the back of the microscope objective using beam steering mirrors, an afocal telescope and a 50/50 beamsplitter (LINOS, Germany). The particles were suspended in deionised water, providing a viscous damping force, partial buoyancy and enabling heat transfer away from the beam focus. White-light illumination was used to create an image of the sample, which was captured on a video camera.

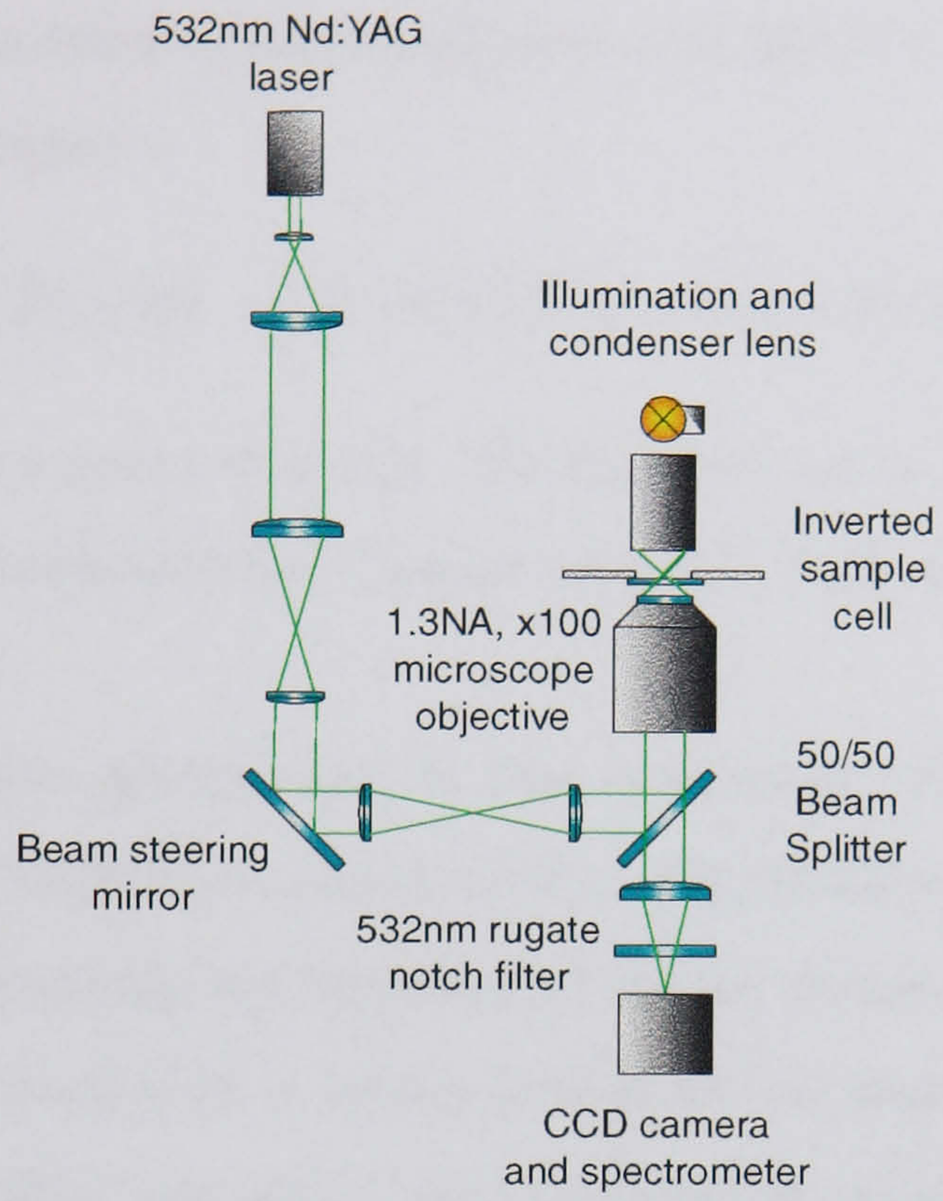

Figure 3.2: The experimental setup for surface enhanced resonance Raman scattering in optical tweezers as described in Section 3.2.1.

3.2.2 Silver coated microparticles

The 1.5 μm diameter silica beads (Lancaster, UK) were silver coated using a Tollen's reagent method [95, 96] for between 10 and 120 minutes. The Tollen's reagent is a mild oxidising agent and was produced by preparing a solution of silver nitrate, $AgNO_3$, in sodium hydroxide, NaOH, and ammonia, NH_3, according to the following reactions [97]:

$$2AgNO_3 + 2NaOH \rightarrow Ag_2O + H_2O + 2NaNO_3 \tag{3.1}$$

Tollen's reagent:

$$Ag_2O + 4NH_3 + H_2O \rightarrow 2Ag(NH_3)_2OH \tag{3.2}$$

When an aldehyde, from a reducing sugar, is mixed with Tollen's solution, the silver ions are reduced to silver. In this case, glucose was used as the

reducing sugar. The silver attaches itself onto a surface if it is clean enough. Reduction of the reagent:

$$RCHO + 2Ag(NH_3)_2OH \rightarrow RCOO(NH_4) + 2Ag + 3NH_3 + H_2O \quad (3.3)$$

where R represents a group of atoms. The simplest case is where R=H and the reducing agent is formaldehyde, whilst when R = $C_5H_{11}O_5$, the reductant is glucose $C_6H_{12}O_6$.

For the particular spheres used in this experiment, 10 drops of 0.4M sodium hydroxide (NaOH) were added to 10 ml of 0.1M silver nitrate ($AgNO_3$) whilst stirring continuously, see Equation 3.1 for the chemical reaction. This resulted in the formation of a brown precipitate to which concentrated, 14.3M, ammonia (NH_3) was added until the solution turned clear, refer to Equation 3.2. 1g of 1.5 μm diameter silica particles (Lancaster, UK) were added, followed by 0.5g of glucose (in powder form), reaction given by Equation 3.3. This mixture was stirred continuously, and 1 ml aliquots were taken, at each sample time required, and centrifuged at 10,000 rpm for 2 minutes. Excess Tollen's solution was washed from the spheres using a 4:1 water:ethanol mixture. The centrifugation and washing steps were repeated. All chemicals were purchased from Sigma Aldrich, BHD and Fisher Chemicals.

The spheres for all the experiments detailed in this Chapter came from the same batch of Tollen's coated microparticles. For the "single coated" particles, samples were taken at 10 minute intervals between 10 and 120 minutes. To investigate if more silver than that produced in the initial reduction reaction could be adsorbed onto the particles, the procedure was repeated to produce "twice-coated" particles. To achieve this, a sample of the spheres

from the original solution, after 60 minutes of coating, was taken. They were centrifuged down, at 10,000 rpm, to remove excess "reacted" solution and then suspended in a fresh Tollen's solution for up to a further 60 minutes. Samples were subsequently taken after 10, 20 and 60 minutes in this new solution and these are referred to as having a total coverage time of 70, 80 and 120 minutes respectively. This was done in order to understand more about how the Tollen's reagent coated the silica particles.

Beads, once made, were then diluted 20 microlitres of partially silvered particles into 1 ml of de-ionised water. This was further diluted into 20 ml of de-ionised water. 200 μl of this solution was then placed in the sample cell of the optical tweezers for all experiments described in this Chapter.

This coating work was carried out by Graeme McNay at the Department of Pure and Applied Chemistry at the University of Strathclyde.

3.3 Methods

3.3.1 TEM's of partially silvered microparticles

Transmission electron microscopy (TEM) images were taken using a JEOL 1200 (JEOL, Japan), operated at 80 kV, of 300 particles at each sample time of 10, 20, 60, 70 and 80 minutes. This allowed the visualisation of the silver coverage on the particles and a comparison between silver coating and trapping probability. The TEM grids were prepared following Method (a) in reference [98] by the University of Strathclyde.

For both "single" and "double" coated spheres, 60 individual particles were viewed in a TEM for each sampling time, and the amount of silver present on their surface was classified into one of four categories by visual inspection: 0-25% of the sphere surface coated with silver, 25-50% of the sphere surface

coated with silver, 50-75% of the sphere surface coated with silver and then particles that were 75-100% coated with silver.

3.3.2 Trapping probability of partially silvered microparticles

An aqueous solution of 1.5 μm diameter silvered silica spheres (200 μl deionised water containing on the order of 10^6 partially silvered beads) was placed into a sample cell and statistics were taken on whether an individual, partially silvered sphere was trapped or repelled using a focussed TEM_{00} laser beam. The partially silvered spheres were produced using the Tollen's reagent described in Section 3.2.2. The experiment was originally done on plain, 1.5 μm diameter silica spheres (Lancaster, UK) in exactly the same setup, as that for the coated beads, for comparison.

For the "single coated" spheres 780 particles were tested, 60 particles for each sample time taken at 10 minute intervals between 0 and 120 minutes. This experiment was subsequently repeated with "twice coated" particles where the Tollen's solution was refreshed after 60 minutes as described in Section 3.2.2.

3.3.3 Q values of partially silvered microparticles

The Q values (Q is a dimensionless quantity describing the amount of a photon's linear momentum that is absorbed by an object) of these silver coated microparticles were calculated using the following method.

A TTi DG 230 frequency generator (RS components, UK) connected to the PZT stage was used to control the frequency, f, with which the sample stage was scanned backwards and forwards over a lateral displacement of 36.5 μm. This meant that when scanned at $1Hz$, the distance covered was

$d = 73\mu$m, i.e. a velocity of 73 $\mu m/s$. See Figure 3.3. The frequency generator wave profile was a triangle wave with a peak to peak voltage of 3V.

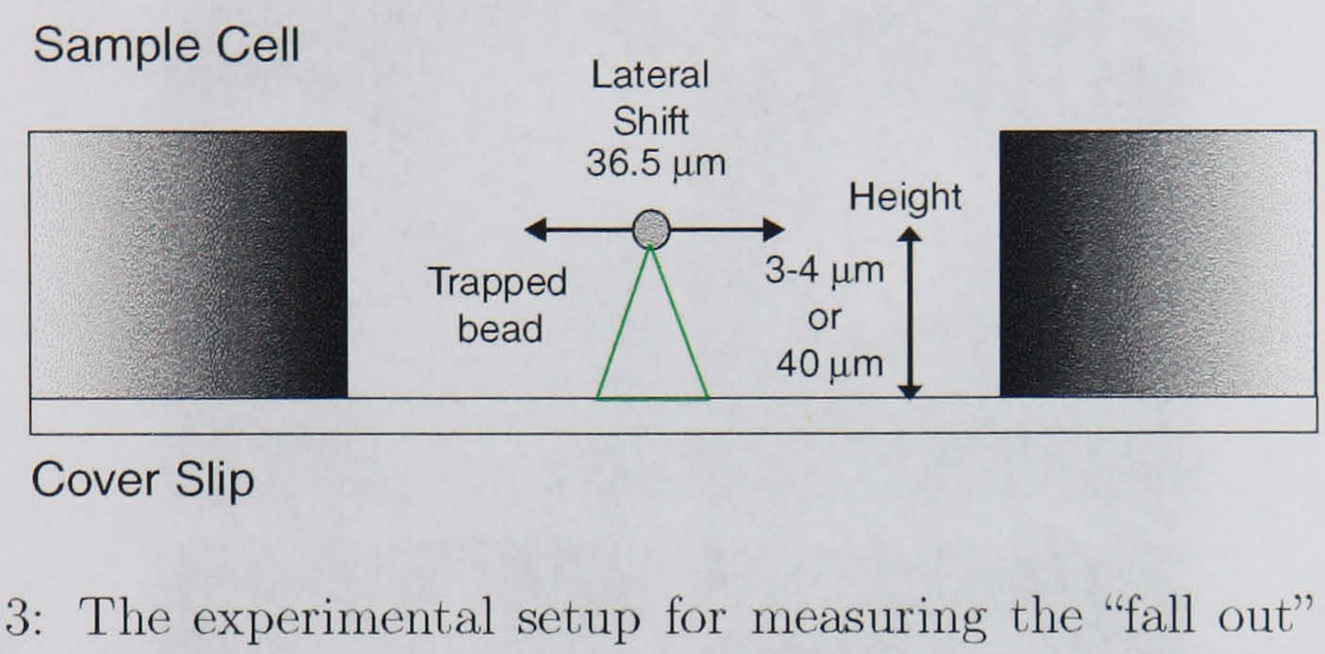

Figure 3.3: The experimental setup for measuring the "fall out" frequency of optically trapped particles. Particles were initially trapped and scanned backwards and forwards at a height of 3-4 μm above the cover slip with increasing frequency over a distance of 73 μm until the bead moved out of the trap. The same particle was then lifted to a height of 40 μm above the cover slip using the PZT and the experiment repeated. See Section 3.3.3 for details.

In order to determine the trapping efficiency of the partially silvered metallic particles, a particle was trapped at the laser focus (a few microns above the cover slip) and the sample stage scanned, with increasing frequency, until the bead moved out of the trap. Knowledge of the fall out frequency and the distance over which the particle was scanned allowed the escape velocity to be calculated using $v = fd$. The escape velocity of the particles was recorded and allowed the drag force, F_{drag}, and Q, the trapping efficiency, to be determined using Equations 2.8 and 2.6. The same sphere was then re-trapped, raised to a higher axial displacement 40 μm above the cover slip using the PZT stage, and the experiment repeated. This was repeated for 10 different spheres at each axial displacement and the average values calculated.

3.4 Results and discussion

3.4.1 TEM's of partially silvered microparticles

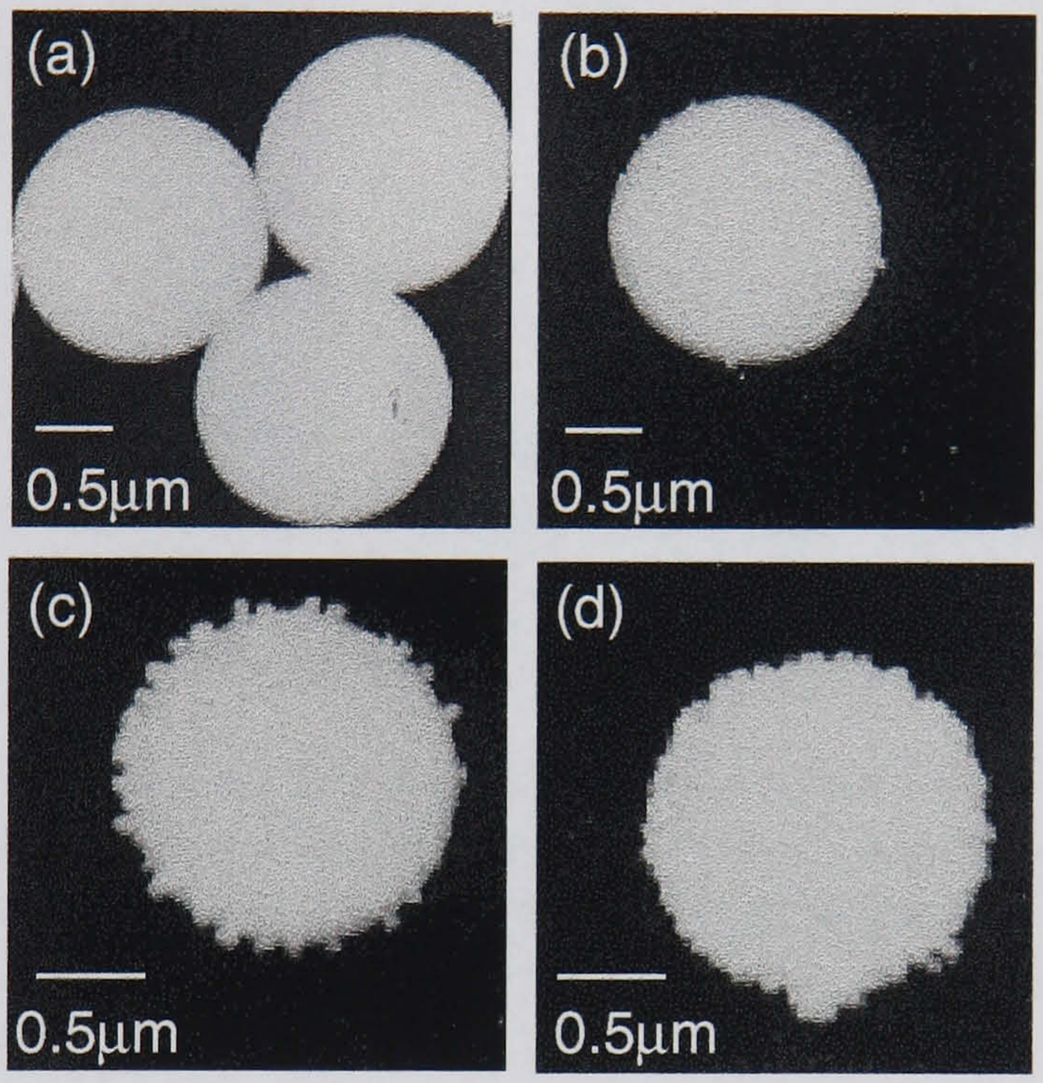

Figure 3.4: Transmission electron micrographs of (a) plain silica particles, (b) a silica particle with 0-25% of its surface coated with silver, (c) a silica particle with 50-75% of its surface coated with silver deposits and (d) a silica particle with 75-100% of its surface coated with silver. It is obvious that the silver does not coat the spheres evenly, but does so partially and in an uneven manner. See Section 3.4.1 for details.

The following graphs show the results from TEM's of the spheres partially silvered by Tollen's reagent. Figure 3.4 illustrates the TEM images of spheres coated for different times for "single coated" particles. Figure 3.4(a) shows the TEM image for plain 1.5 μm diameter silica spheres. The amount of silver covering the surface can vary from almost none, Figure 3.4(b), to a complete, although very uneven, coating as shown in Figure 3.4(d). It is clear from these images that the silver coating is not uniform, but that silver deposits are left on the surface of the microparticle.

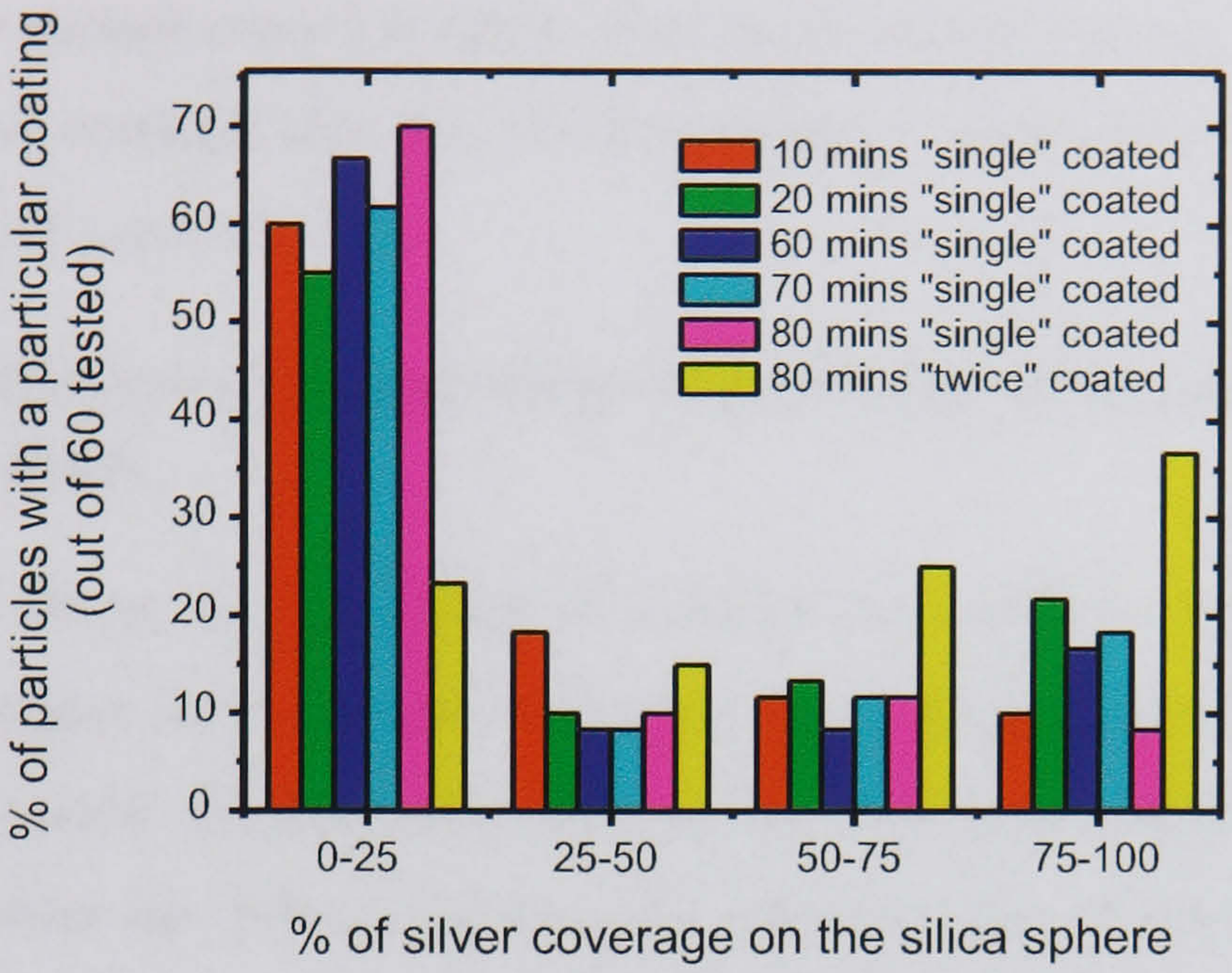

Figure 3.5: For each of the coating times, 60 particles were viewed and the amount of silver on their surface assessed. The amount of silver on the surface of the sphere was split into four categories: 0-25% coated, 25-50% coated, 50-75% coated and 75-100% coated. The Tollen's reagent was not changed in this experiment. See Section 3.4.1.

Figure 3.5 shows the TEM results for the percentage of the sphere's surface coated in silver for "single coated" particles. 63% (188/300) had up to a quarter of their surface coated with silver deposits, while 15% (45/300) had a surface that had between three-quarters and all of their surface coated with silver. The remainder had between a quarter and a half of their surface coated with silver. Furthermore, the amount of coating on the particle surface appears to be independent of coating time, implying that all the coating effectively takes place within the first few minutes of the reaction, as further demonstrated in Section 3.4.2.

For the "twice coated" particles, only 23% of the particles had less than a quarter of their surface coated in silver after 80 minutes. However, there was an increase in the number of particles that had between three-quarters and

all of their surface coated in silver. For the 80 minute sample, 37% (22 60) had a silver coverage that fell into this category compared to 15% for the single coated particles.

3.4.2 Trapping probability of partially silvered microparticles

Figure 3.6 shows the percentage of particles that could be trapped in the optical tweezers as a function of coating time. Figure 3.6(a) corresponds to "single coated" particles only while 3.6(b) also shows the "twice coated" particles where the Tollen's solution was refreshed after 60 minutes.

In both cases, for uncoated, plain silica particles, all 60 particles (100%) tested trapped without difficulty as expected. This value dropped to 68% (492/720) for particles with a "single" Tollen's coating. See Figure 3.6(a). For the spheres that were "twice coated", 71% (255/360) trapped between the 10 and 60 minutes coating time. This corresponds to the "single coated" particles mentioned above and the percentage of particles that trapped is comparable as expected. For the "twice coated" spheres, 13% (46/360) of the particles tested trapped i.e. those particles where the Tollen's solution was refreshed after 60 minutes. Refer to Figure 3.6(b).

The results from Figure 3.6(a) and 3.6(b) suggest that the coating of the metallic particles using the Tollen's reagent could be described by an adsorption isotherm, such as a Langmuir isotherm [60, 99, 100] (or some variant), showing saturation due to depletion of the reagent.

It was found that the "single coated" particles could be trapped starting from a configuration with the beam focus either above or below the centre of the sphere and that they could be easily manipulated in three dimensions, see Figure 3.7. Figures 3.7(a) to 3.7(b) show a trapped, "single coated" particle

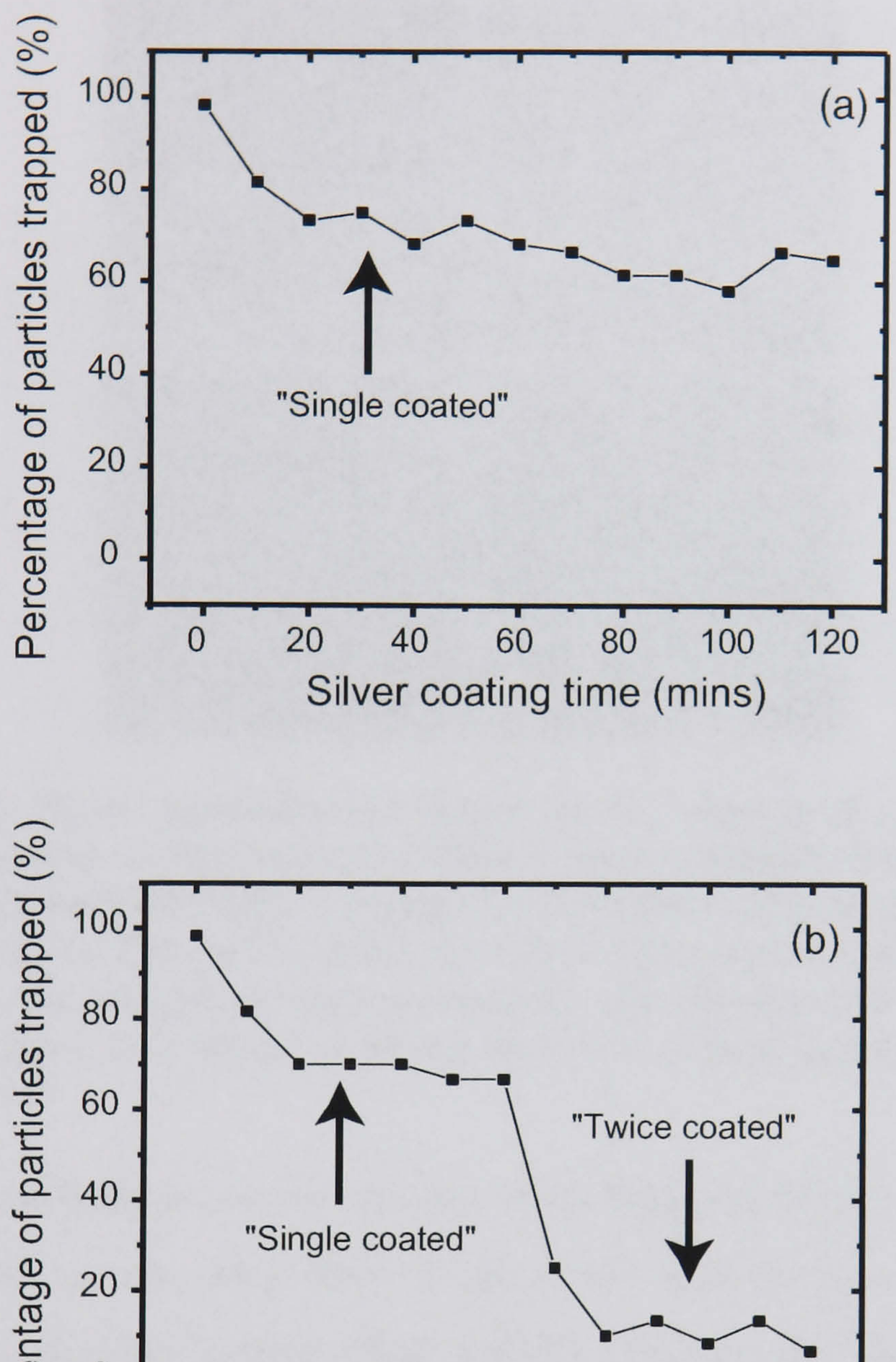

Figure 3.6: Graph (a) shows the percentage of silica particles trapped ($n = 60$) with the sphere surface silvered using a Tollen's reagent method, i.e. "single coated" particles. The second graph, (b), shows the percentage of silica particles trapped ($n = 60$) with the sphere surface silvered using a Tollen's reagent method which was refreshed after 60 minutes corresponding to "twice coated" particles. See Section 3.4.2 for details on the trapping probability.

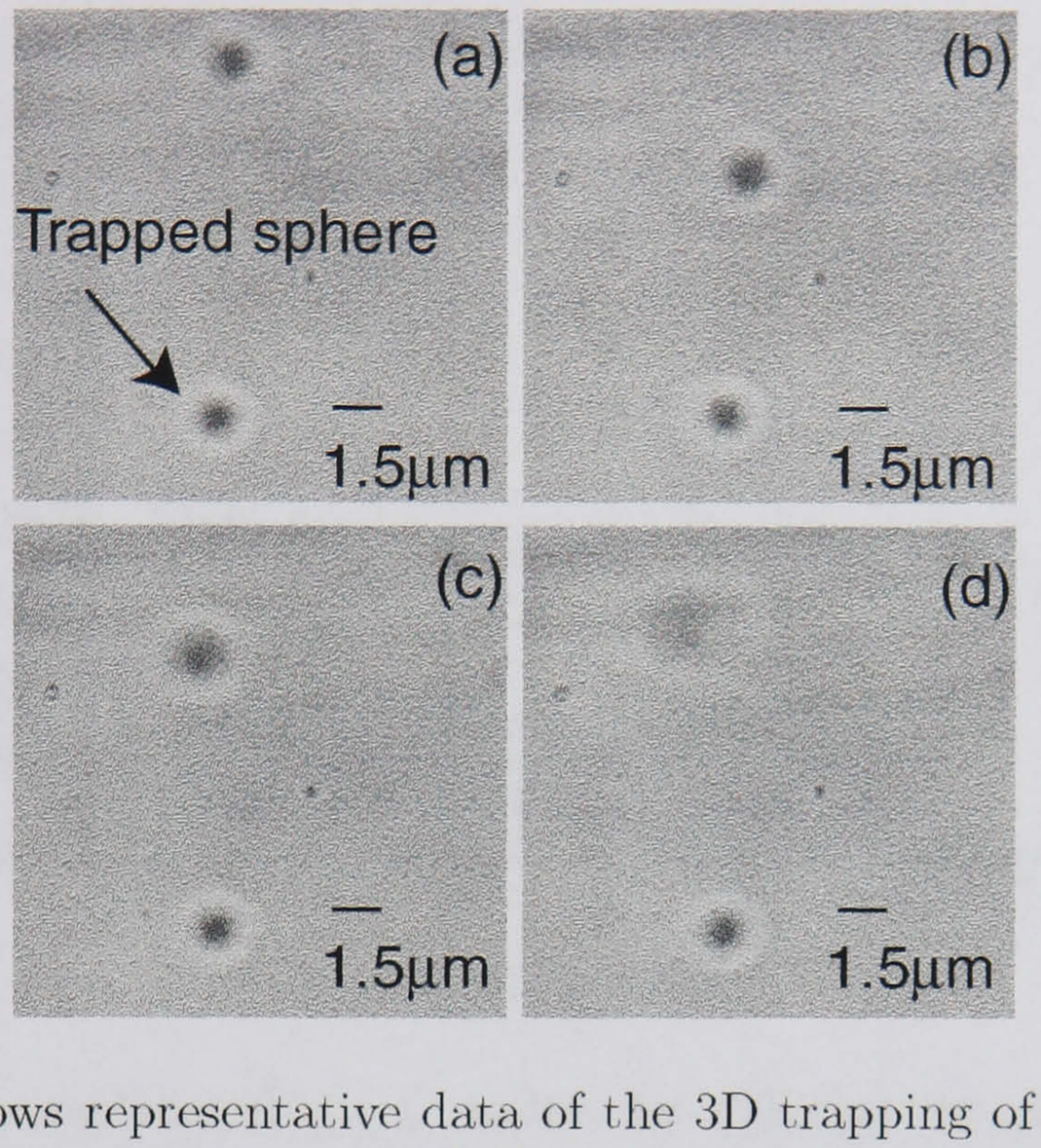

Figure 3.7: Shows representative data of the 3D trapping of a silica sphere partially coated in silver using the Tollen's reagent method. The sphere was left to react with the Tollen's reagent for 60 minutes. Picture (a) shows the trapped sphere. Picture (b) shows the sphere being moved towards another particle in the sample and then pictures (c) and (d) show the metal particle being lifted to a height of 40 μm above its original position. Refer to Section 3.4.2.

being moved in the transverse direction while Figures 3.7(c) and 3.7(d) show the trapped particle being lifted 40 μm in the axial direction. This is in contrast to previous findings where metallic Mie-sized particles could only be trapped in 2 dimensions provided the beam focus was located near the bottom of the particle [38].

3.4.3 Q value of partially silvered microparticles

Figure 3.8 demonstrates the Q values of the "single" and "twice" coated microparticles both at the beam focus and lifted up 40 μm into the sample cell.

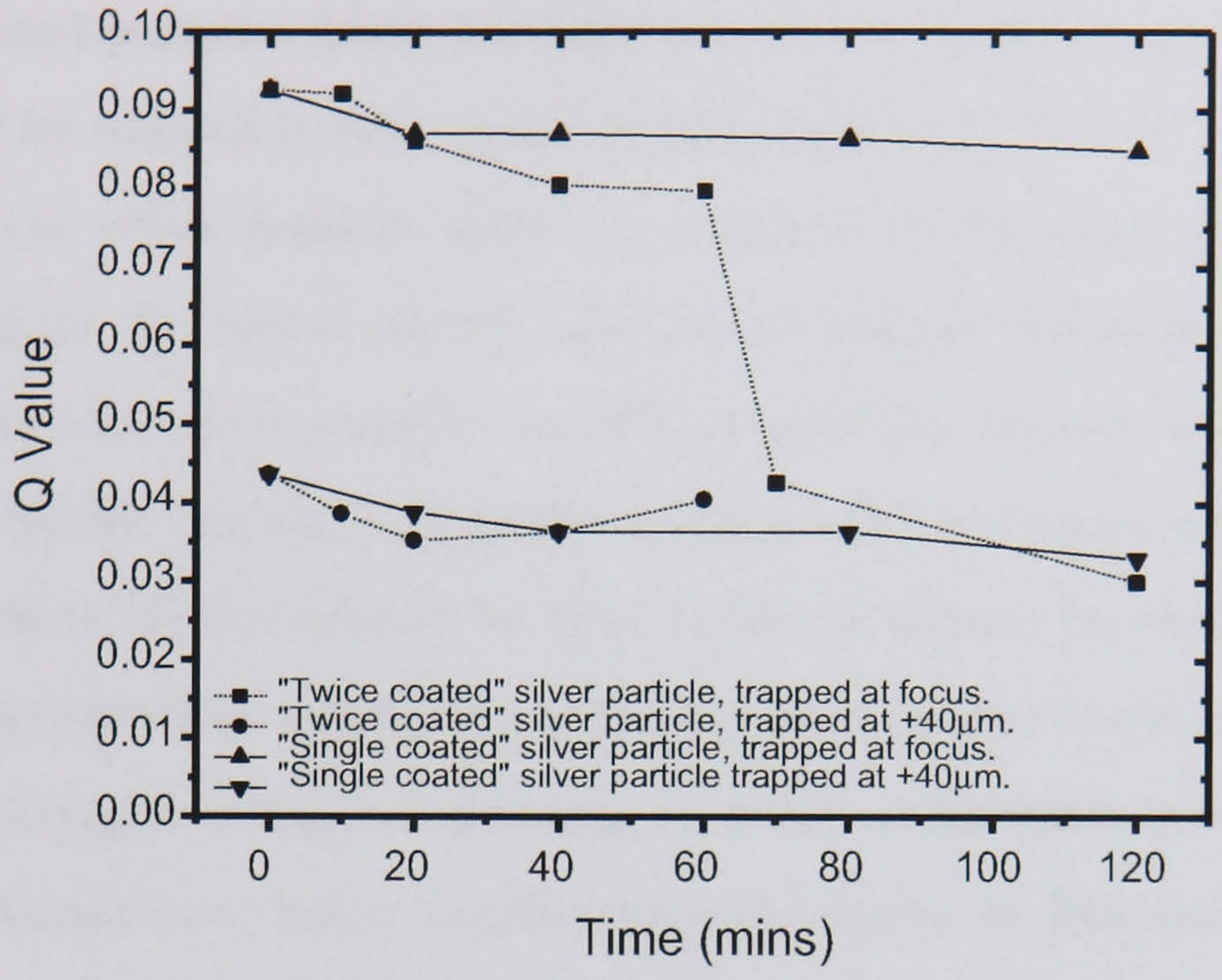

Figure 3.8: Comparison of the Q values for different "single" and "twice" coated silver, silica spheres at the focus of the laser beam and lifted 40 μm above the beam focus. See Section 3.4.3 for more details.

For plain silica spheres, the Q value was 0.092±0.004 at zero axial displacement. This fell to 0.086±0.008 for "single coated" particles and to 0.03±0.01 for "twice coated" particles. This corresponds to a fall out frequency of 4.0±0.2 Hz, 3.6±0.2 Hz and 1.2±0.4 Hz for the plain silica, "single coated" and "twice coated" particles respectively. The values are quoted as mean±variance and is a measure of the spread of results that arises from a real variation of the spheres, i.e. a variation in the amount of silver present on the surface of the spheres.

For an axial displacement of 40 μm, the Q value was 0.044±0.006 for plain silica spheres and 0.036±0.003 for the "single coated" spheres which corresponds to fall out frequencies of 1.9±0.3 Hz and 1.5±0.1 Hz. It was not possible to lift the "twice coated" particles axially.

It is interesting to note that the graphs of the Q values for the "single" and

"twice" coated particles follow the same trend as the percentage of particles that could be trapped in both cases, as illustrated in Figure 3.6.

When the silver deposits cover the majority of the sphere surface, as in the case of the "twice coated" 120 minute sample, trapping was more difficult and was rarely possible. In 90% of cases the spheres were strongly repelled. For this reason, those particles that could be trapped could only be manipulated in 2D and couldn't be lifted axially by 40 μm. Previous methods that trapped metallic spheres using the repulsive nature of the laser beam also only managed to trap metallic spheres in 2D, as discussed in Section 3.1.

Even though silver has a complex refractive index, as discussed in Chapter 2.2.1, it is thought that the dominant factor affecting the trapping mechanism of the semi-transparent spheres here was the fraction of the surface area that was covered with silver. The 25% critical coverage may be at the point where the scattering force equals the gradient force. The silver coverage on the sphere also made little difference to the force of gravity on the particle, Equation 2.11. Even if the particle was coated with a 100 nm thick layer of silver ($\rho_1 = 10490\ kg/m^3$) over the whole surface area, the force of gravity is still on the order of $10^{-14}N$ which is negligible in comparison to the gradient and scattering forces ($pN's$).

3.5 Conclusions

3.5.1 TEM's of partially silvered microparticles

It is interesting to note that, for "single coated" particles, the 68% of particles that trapped in our optical tweezers is similar to the fraction, 63%, of particles with up to a quarter of their surface coated with silver. The remaining fraction corresponds to those particles that are strongly repelled from the

optical trap. It can be postulated that the trapping mechanism can be explained by the fact that those particles, with less than 25% (or some number close) surface coverage, are sufficiently transparent to enable refraction of the light beam through the sphere. This hypothesis assumes that these particles are trapped by a similar mechanism to that for a dielectric particle. Similarly for the particles that were "twice coated" with the Tollen's reagent, less than 25% of the particles had less than 25% of their surface coated in silver. However, only 13% of the "twice coated" particles trapped when one might have expected 25% to trap. This may possibly be be attributed to the fact that the spheres are biased more towards a 25% coating than a 0% coating as the classification categories are very broad.

3.5.2 Trapping probability of partially silvered microparticles

For the "single coated" particles, the number of particles that could be trapped remained constant at about 68% from the 10-120 minute coating time. In the case where the Tollen's reagent was changed, the percentage of silver particles trapped remained similar to that for the "single coated" particles, 71% compared to 68%, between the 10 and 60 minute coating time i.e. before the Tollen's solution was refreshed. However, there was a reduction in the number of particles that could be trapped after 60 minutes, from 71% to 13%, over a period of several minutes i.e. "twice coated" particles. This corresponds to the refreshing of the Tollen's solution after 60 minutes. This "step" action illustrating the decrease in the number of particles that can be trapped at the start of each Tollen's reaction confirms that all the coating effectively happens as soon as the spheres are immersed in the Tollen's solution. It is possible that the coating mechanism could be described by a

Langmuir, or other, isotherm, where there is saturation due to depletion of the reagent. Therefore, it does not appear to matter how long the spheres are left in the Tollen's solution for, effectively either "single" or "twice" coated particles are produced depending on whether or not the Tollen's reagent was refreshed.

3.5.3 Q values of partially silvered microparticles

By referring back to Figure 3.6 it is clear that the Q values, Figure 3.8, follow the same trend as the number of particles that can be trapped with the TEM_{00} laser beam. This is to be expected as the amount of silver on the surface of the sphere depends primarily on whether the particle was coated once or twice using the Tollen's reagent. As the amount of silver on the surface of the sphere increased, it was more difficult to trap the particle as the scattering force overcomes the gradient force.

3.5.4 Conclusion

It has been demonstrated that it is possible to trap partially silvered microspheres using a standard focussed optical trap with an efficiency similar to that of a dielectric particle. This is far simpler than the previous methods of trapping for conventional metallic particles that involved scanning or annular beams to create an optical "cage" around the microparticle. More importantly, it allows the three dimensional manipulation of the particle which was not possible with some of the metallic trapping methods that relied upon the repulsive nature of beam. In short, this new kind of partially silvered particle allows for the easy trapping associated with dielectrics whilst allowing the metallic nature of the particle to be exploited.

It was found that the deposition of silver using the reduction of the Tollen's reagent on the spheres ceased after 10-20 minutes, implying that the coating time was not critical after this time scale. It was also shown that the silver coating on the silica spheres was not uniform, but consisted of silver deposits on the surface. Consequently, silica spheres that were partially coated with less than 25% of silver on their surface could be trapped easily. Interestingly, after a few minutes of coating, there was no appreciable difference in the percentage of particles that could be trapped, implying that the coating effectively took place within the first few minutes of the Tollen's reaction.

The trapping mechanism may be explained by the fact that the particles are sufficiently transparent to enable refraction of the beam through the sphere to produce a net attractive force to the region of highest light intensity. In other words, it was trapped using a similar mechanism to that of a dielectric particle.

This ability to easily trap partially coated microspheres, that are rough on the nm scale, using a TEM_{00} laser beam, has an important application in that it can be used to demonstrate an analytical chemistry technique called surface enhanced resonance Raman scattering, or SERRS. This is discussed in Chapters 4 and 5, also confirming that the trapped particles do indeed have a partial metallic coating that is not ablated before trapping.

The work presented in this Chapter has resulted in one journal publication.

- Pamela Jordan, Graeme McNay, Frances T. Docherty, Gavin Sinclair, W. Ewen Smith, Jonathan M. Cooper and Miles Padgett, "3D optical trapping of partially silvered microparticles", Opt. Lett., 29, 2488-2490 (2004).

Chapter 4

Surface enhanced resonance Raman scattering in optical tweezers

The trapping efficiency for partially metal coated particles (discussed in Chapter 3) was optimsed, and subsequently used to investigate SERRS. This technique relies on optical signal enhancement, associated with the interaction of a molecular species with a surface plasmon, generated at a metal surface. By over coming the difficulties for trapping metallic particles, it was possible to collect an intense, characteristic vibrational spectrum, associated with a molecular species adsorbed on the surface of a partially silvered particle in real time.

4.1 Introduction

Optical interrogation enables simultaneous trapping, visualisation and collection of vibrational spectra, such as Raman, SERS and SERRS (described in Chapter 2.3). SERRS can be used for spectroscopic, and/or bioanalytical, studies in which a metallic surface can enhance an optical signal due to a surface plasmon effect [58]. Key to this dual enhancement process is the ability

to adsorb a chromophore onto a roughened metallic surface. By choosing an excitation wavelength that is in resonance with both an electronic absorption maxima of the chromophore and the surface plasmon of the metal, SERRS can demonstrate sensitivities that are comparable to fluorescence [89, 90] and up to 10^{14} times greater than Raman scattering. SERRS has several advantages over fluorescence in that it has well defined spectral peaks. This makes it easy to simultaneously distinguish four or five different spectra and corresponding analytes in a mixture.

Previously, Raman spectroscopy and optical tweezers have been combined to study living biological cells with a near infra-red trapping laser as the excitation source [54]. Biological objects (cell size often 1-10 μm) are easily trapped in optical tweezers as they are almost transparent (to infrared wavelengths), and the trapping mechanisms for a transparent, dielectric particle apply. SERS spectra have also been recorded in an optical tweezers [56] from silver particles coated with rhodamine or phenylalanine and collated into large clusters. However, long integration times (5-10 seconds) were required. These metallic particles were not trapped, but pushed up against a glass plate by the repulsive force of the laser beam, a problem that was described and overcome in Chapter 3. The sensitivity of SERRS has allowed single molecules and nanoparticles to be detected [88].

Here the use of optical tweezers to trap dye coated, partially silvered silica particles suspended in solution to produce intense SERRS spectra from a single bead is demonstrated. SERRS gives a characteristic spectra that is dependent upon the dye molecules that are adsorbed onto the metallic surface. This can be visualised on a video camera and recorded with a spectrometer.

This work was carried out in collaboration with Graeme McNay and Prof W. Ewen Smith at the Department of Pure and Applied Chemistry at the University of Strathclyde, Glasgow, G1 1XI.

4.2 Experimental setup and materials

4.2.1 Optical tweezers setup

The optical tweezers setup was similar to that described in Chapter 3.2.1. The spectra from the particles were viewed using a CCD camera (Pulnix, Denmark) through a holographic filter (Edmund Optics, UK) that removed the laser light at 532 nm ("Excel", Photonics Solutions, Germany). All the particles trapped for the following experiments were done so using 10 mW at the trapping plane, measured using a Newport 1815-C power meter (Newport, UK). The spectra of the scattered light was recorded using an R2001-532 Raman spectrometer (Ocean Optics, UK), using 100 ms integration time, with a fibre optic cable that was aligned in the image plane of the microscope and aligned with the position of the trap. The fibre optic cable comprised a 600 μm diameter and a 6 μm detection area, as the optical tweezers uses a x100 objective lens (Zeiss, UK), limiting the signal detection area to the vicinity of the optical tweezers trap.

4.2.2 SERRS active microparticles

The 1.5 μm diameter silver coated silica beads (Lancaster, UK) were prepared by the Department of Pure and Applied Chemistry at the University of Strathclyde using a Tollen's reagent method, as described in Chapter 3.2.2.

An azo dye, 3,5-dimethoxy-4-(6-azobenzotriazol)-phenylamine (Made in-house,

University of Strathclyde), was adsorbed onto the partially silvered microparticles using the following method; 20 μl of silver microparticle solution, as described in Chapter 3.2.2, was immersed in 1 ml of water and spun down, at 10 000 rpm, to remove excess Tollen's solution. The resulting silvered spheres were then immersed in 1 ml of 1×10^{-6}M 3,5-dimethoxy-4-(6-azobenzotriazol)-phenylamine dye and incubated for a period of 24 hours. 20 μl of this silvered spheres and dye solution was then diluted into 20 ml of water. 200 μl of this resulting solution was placed in the sample cell of the optical tweezers for all experiments described in this Chapter. It has been previously demonstrated that this dye is SERRS active when adsorbed onto silver colloid and excited using 514 nm light [101].

Samples of beads immersed in 10^{-4}M, 10^{-6}M and 10^{-7}M dye concentration solutions were prepared. Monolayer coverage (i.e. a single layer of dye around the particle) corresponds to a solution containing between 10^{-3}M and 10^{-4}M dye, depending on the whether the dye molecule orients itself vertically or horizontally (the dye molecule used here can be approximated to a cuboid 3 Å $\times$ 8 Å $\times$ 1 Å) on the surface, although a random orientation is most probable. Therefore, a 10^{-4}M solution should be capable of producing a monolayer of dye. With a solution containing 10^{-6}M or 10^{-7}M azo dye, there is less than monolayer coverage available and hence will give sporadic areas of dye adsorbed onto the partially silvered particle. Dilutions of the dye were done with methanol and water.

4.3 Methods

4.3.1 Confirmation of SERRS from single silver coated silica microparticles in optical tweezers

Silver microparticles, modified by a 10^{-6}M dye solution, were placed in a sample cell that sat in the focus of the optical tweezers trap on top of a PZT stage using the setup described in Section 4.2.1. These individual modified microparticles were trapped in the laser beam and any SERRS response recorded. Prior to recording the spectrum, the laser beam was blocked using a beam stop and a dark current spectrum recorded. This dark spectra was automatically subtracted from any subsequent recorded spectra. The experiment was repeated using silica particles coated only with silver to confirm that there was no SERRS signal from plain silica samples that could interfere with the SERRS signals recorded from silver and dye modified silica spheres.

The SERRS spectrum from dye adsorbed on colloidal silver was acquired using a Renishaw 2000 Raman Microprobe with a CCD spectrometer (Renishaw Plc, UK), a dedicated Raman system at the University of Strathclyde. The excitation was provided by a Spectra-Physics Model 2020 argon-ion laser (Renishaw Plc, UK) with a wavelength of 514.5 nm and 3 mW of power at the source. This experiment was also carried out on dye only coated silica particles to confirm that there was no significant SERRS spectra from such modified microparticles.

4.3.2 Visualising the SERRS signal

The partially silver and dye coated silica microparticles were again placed in a sample cell within the optical tweezers setup, described in Section 4.2.1, with 10 mW of power at the trapping plane. The focussed laser beam was

brought close to a single microparticle, as though trying to trap it, and their interaction (spectral and visual) recorded. The collection of the SERRS spectra was performed using an Ocean Optics S2000 spectrometer (Ocean Optics, UK), with dark current subtraction. The resolution of this spectrometer was poor (optical resolution 2.5 nm, or 88 cm^{-1}, FWHM [102]), compared to the dedicated Raman system (which can resolve spectra down to 15 cm^{-1} or 0.14 nm FWHM), and cannot distinguish between the several, closely spaced sharp peaks that a dedicated Raman spectrometer can. However, it does show two principal spectral features at 1352 cm^{-1} and 1601 cm^{-1}. Solutions with 10^{-4}M, 10^{-6}M and 10^{-7}M dye adsorbed onto the surface of the silvered spheres were prepared, using the method described in Chapter 3.2.2, and the effect of the dye concentration on the visual SERRS investigated.

4.3.3 SERRS from spheres in the vicinity of the laser beam

The silver and dye coated microparticles, modified using a 10^{-6}M concentration azo dye solution, were placed in a sample cell that was positioned at the focus of the optical tweezers, described in Section 4.2.1, with 10 mW delivered at the trapping plane. The focussed laser beam was used as a tool to excite spheres, that were immobilised (by physical adsorption) onto the bottom of the cover slip of the sample cell, with the focal point of the laser a distance of 2 μm away from the immobilised sphere. The visual response was recorded using the CCD camera before the experiment was repeated with the focal point of the tweezers trap lying on the periphery of the 1.5 μm diameter sphere. The sample was kept at the focal point of the tweezers trap in the axial direction and only moved in the lateral direction. The convergence half angle of the light focussed by the 1.3 N.A. microscope objective is

59.1 degrees through immersion oil and the glass cover slip, and 77.8 degrees through water.

4.3.4 Effect of dye concentration on Q value of SERRS active particles

The calculation of the Q values here was performed in exactly the same way as described in Chapter 3.3.3, except that here the azo dye, for solutions containing either 10^{-1}M or 10^{-6}M 3,5-dimethoxy-4-(6-azobenzotriazol)-phenylamine dye, was adsorbed onto the silver particles and investigated. The sample cells were loaded with solution and mounted on the PZT stage with 10 mW of power delivered at the trapping plane. Ten beads were trapped at each position, at the beam focus and lifted 40 μm above the cover slip, and average Q values calculated.

4.4 Results and discussion

4.4.1 Confirmation of SERRS from single silver coated silica microparticles in optical tweezers

For the 3,5-dimethoxy-4-(6-azobenzotriazol)-phenylamine dye, the most intense features in the Raman spectrum are between 1200 cm^{-1} and 1600 cm^{-1}. For the SERRS spectra observed, the three most distinct or "characteristic" peaks occur at 1249 cm^{-1}, 1352 cm^{-1} and 1601 cm^{-1}, which, when using a 532 nm excitation source, correspond to wavelengths of 570 nm, 573 nm and 582 nm. The 1352 cm^{-1} peak is attributed to the -N= N- (azo) stretch of the dye and the 1601 cm^{-1} band is attributed to the symmetric -C-C- stretch in the benzene rings. The 1249 cm^{-1} band may be caused by an azide stretch while the small peaks between 1400 - 1500 cm^{-1} may be caused by -C-H- deformation.

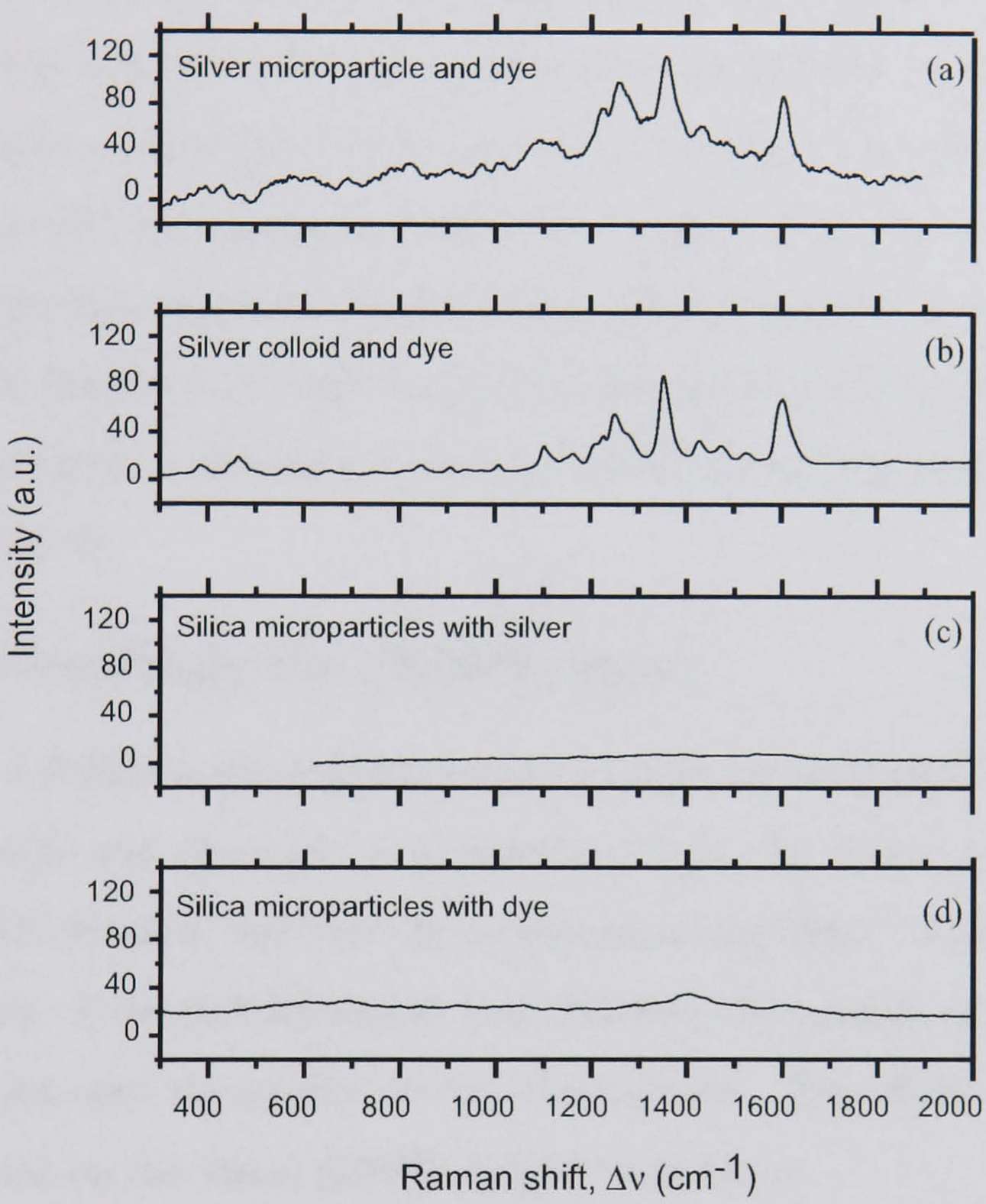

Figure 4.1: Comparison of the SERRS spectra obtained from a) the 10^{-6}M solution azo dye adsorbed onto partially silvered microparticles and recorded in the optical tweezers setup, b) the azo dye adsorbed on silver colloid and analysed in a dedicated Raman system, c) partially silvered silica particles and d) dye adsorbed onto plain silica particles. The 1352 cm^{-1} peak is attributed to the -N=N- (azo) stretch of the dye and the 1601 cm^{-1} band is attributed to the symmetric -C-C- stretch in the benzene rings. See Section 4.4.1 for more details.

Figure 4.1(a) confirms that the spectra recorded in the optical tweezers setup, consisting of the raw data with dark current subtraction, was indeed SERRS as it was the same as the spectra taken at Strathclyde where the same dye was adsorbed onto silver colloid and analysed within a dedicated Raman system as illustrated in Figure 4.1(b). No signal was observed from partially silvered silica particles (with no dye added) or for the circumstance when the dye was adsorbed onto plain silica particles (with no silver coating), as shown in Figures 4.1(c) and 4.1(d). This provides corroborative evidence that silver, which is necessary for surface enhancement, was present on the trapped particle.

4.4.2 Visualising the SERRS signal

Whenever a SERRS active particle interacted with the laser beam, an intense "flash" of light was observed. It is postulated that this "flash" corresponds to a SERRS emission, and that the brightness of the "flash" is indicative of the intensity of the SERRS signal, and therefore the amount of silver and dye adsorbed onto the surface of the silica particle. The effect of the dye concentration on the visual SERRS is illustrated below.

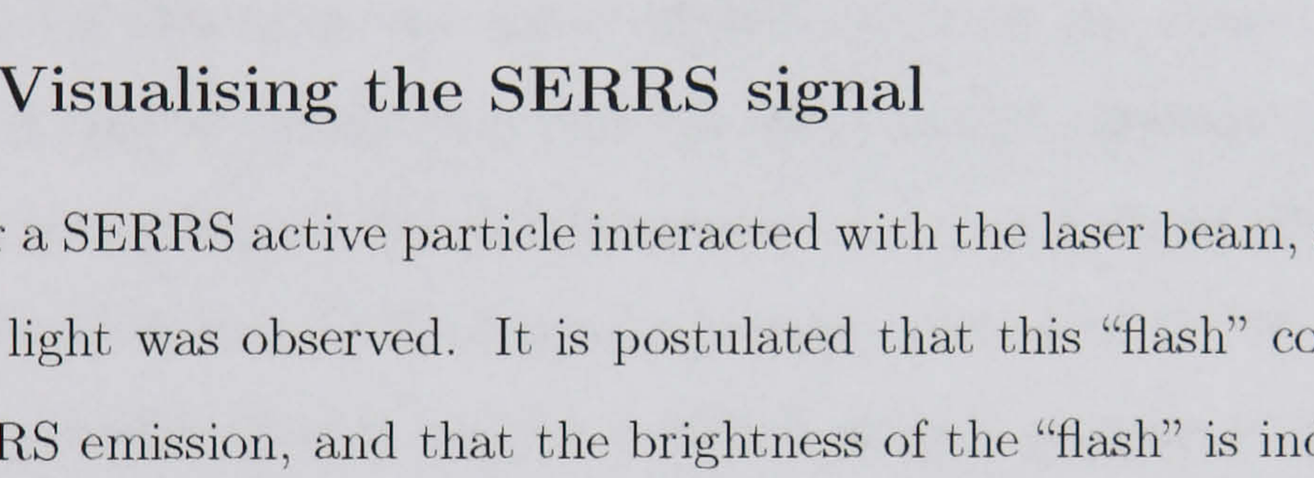

Figure 4.2: SERRS from silica beads partially coated in silver and coated with a 10^{-4}M concentration dye solution. Figure (a) shows the sphere approaching the laser beam, (b) shows the visual SERRS and (c) shows how the sphere is repelled away from the beam after interaction. There is 100 ms between each frame. Refer to Section 4.4.2 for more details.

Figure 4.2 shows a real time sequence where a silver coated microparticle, modified in a solution containing 10^{-4}M dye, interacted with the 10 mW laser beam. In Figure 4.2(a) there is a sphere approaching the optical trap. It is not possible to see the optical trap (as it has been filtered out using a 532 nm holographic filter). Figure 4.2(b) clearly shows an intense visual SERRS signal where the sphere is drawn into the optical trap. However, this also produces a large repulsive force and Figure 4.2(c) shows the sphere being repelled away from the laser beam, most probably due to a large amount of silver being present on the surface of the sphere. There is 100 ms between each picture.

Figure 4.3 illustrates the visual SERRS effect of the different concentrations. It can be clearly seen that the silver coated particles modified in a solution containing 10^{-4}M dye demonstrated a strong visual effect, as did the particle which was modified using a priming solution of 10^{-6}M dye. However, the partially silvered spheres modified using a solution of 10^{-7}M dye exhibited little or no visual SERRS and a corresponding unconvincing spectra on the spectrometer. There was little difference in the visual effect with different silver coating times, which further corroborates hypotheses drawn from earlier results, in Chapter 3, namely that the time for adsorption of the Tollen's reagent takes $\ll$ 20 minutes.

4.4.3 SERRS from spheres in the vicinity of the laser beam

SERRS can also be recorded from dye coated, partially silvered spheres that interact within the vicinity of the laser beam. Figure 4.4 illustrates two examples where a SERRS emission was excited without the optical tweezers trapping the sphere. Figure 4.4(a) shows a SERRS signal being excited with

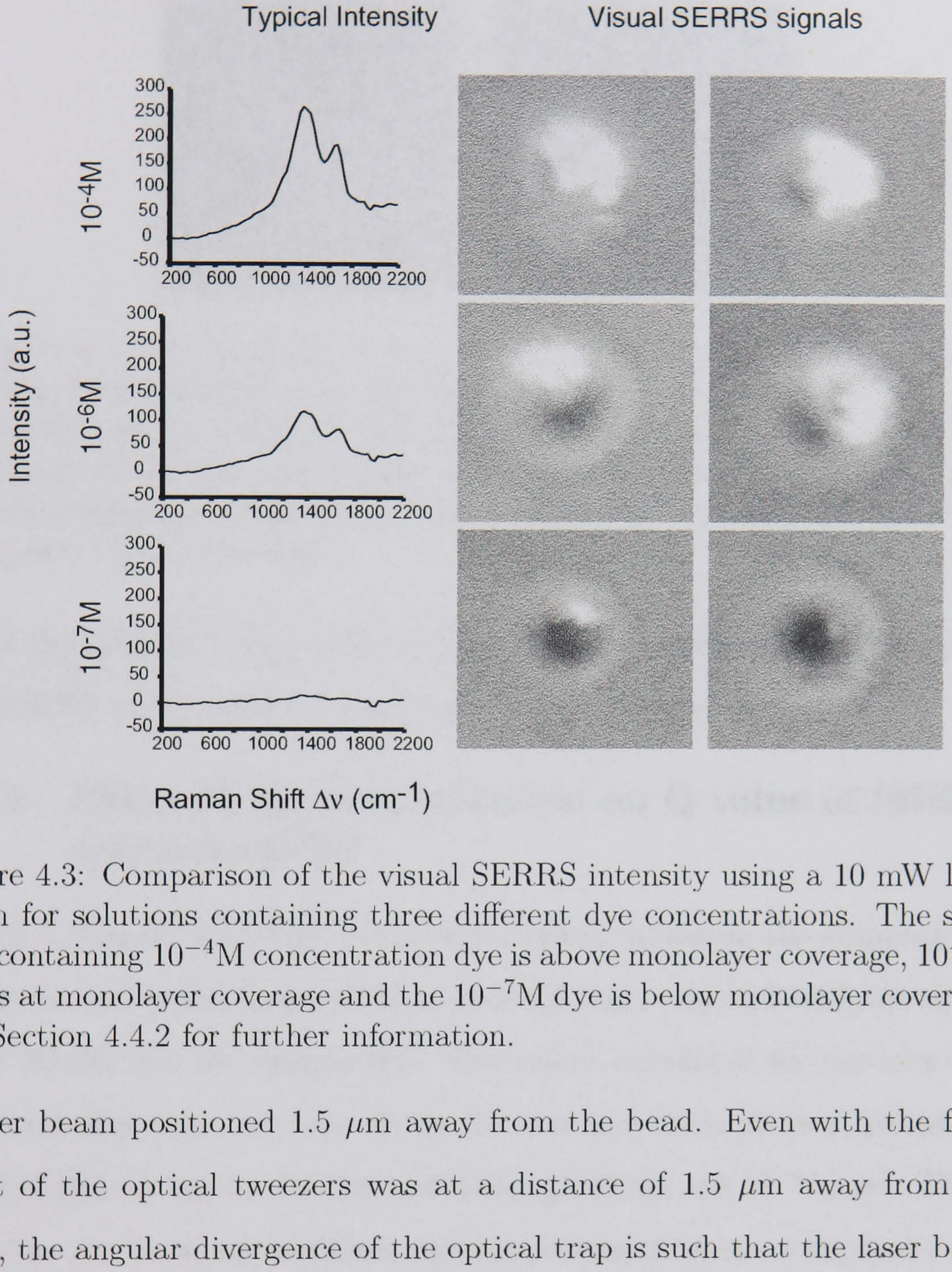

Figure 4.3: Comparison of the visual SERRS intensity using a 10 mW laser beam for solutions containing three different dye concentrations. The solution containing 10^{-4}M concentration dye is above monolayer coverage, 10^{-6}M dye is at monolayer coverage and the 10^{-7}M dye is below monolayer coverage. See Section 4.4.2 for further information.

a laser beam positioned 1.5 μm away from the bead. Even with the focal point of the optical tweezers was at a distance of 1.5 μm away from the bead, the angular divergence of the optical trap is such that the laser beam could still "touch" the top of the 1.5 μm diameter modified microparticle and, hence, should be able to stimulate a SERRS response. This excitation is less intense than that demonstrated in Figure 4.4(b), but it is also much longer lived. This SERRS emission in Figure 4.4(a) can be observed for a period of up to 10 seconds, compared to 100 ms for Figure 4.2 described in Section 4.4.2. Figure 4.4(b) shows a shorter lived, although more intense

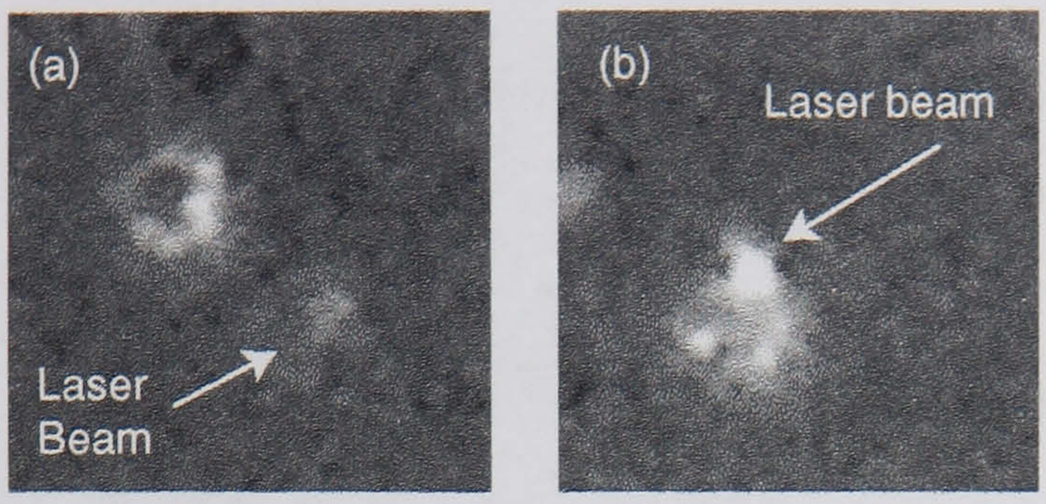

Figure 4.4: Two examples of the characteristic speckle pattern when (a) the long lived emission when the laser beam is a finite distance away from the beads and (b) the short lived radiation when the laser beam is on the periphery of the dye coated silica sphere. The radiation is emitted from discrete regions on the particle which is thought to be highly SERRS active hot spots. See Section 4.5.3.

signal than Figure 4.4(a), with the laser focus lying just on the periphery of the SERRS active particle, which lasts in the region of 1s.

4.4.4 Effect of dye concentration on Q value of SERRS active particles

Figure 4.5 shows the effect of the dye concentrations on the trapping of a sphere in the optical tweezers both near the cover slip and with the sphere lifted 40 μm into the sample cell. The values calculated for particles near the cover slip show that the Q for the dye and silver coated spheres are 0.063 ± 0.005 for the 10^{-4}M dye and 0.061 ± 0.002 for the 10^{-6}M dye. This is less than the Q value for plain, single coated silvered spheres trapped at the same position, of 0.086 ± 0.008. The most probable reason for the reduction of Q here is that the particles may become more absorptive when they have dye on their surface. Laser damage to the sample and radiation produced from the SERRS active particles may produce an extra repulsive force that could contribute to the reduction in the Q value, although both of these "events" are unlikely. The dye concentration does not appear to have an effect on

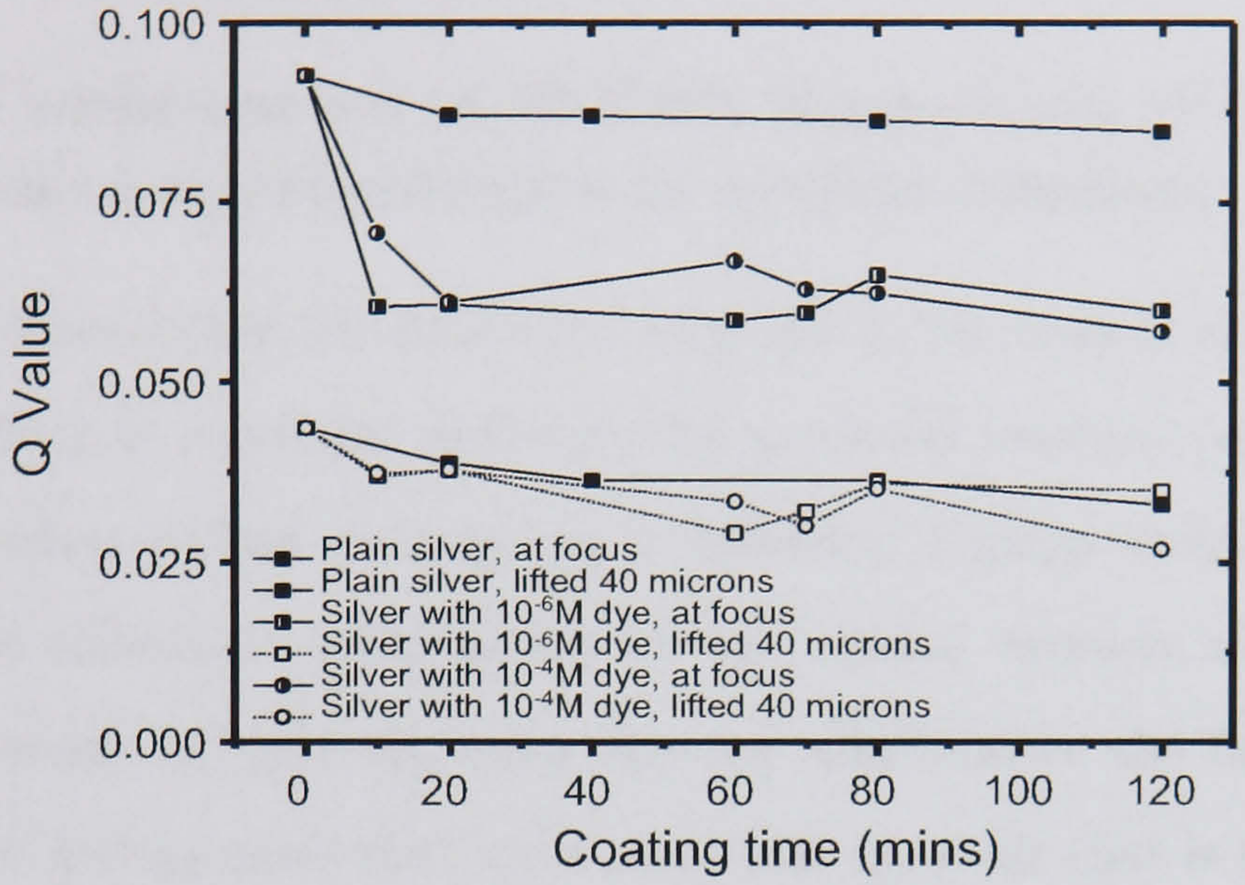

Figure 4.5: Comparison of the Q values for different silver and dye coated silica spheres and at the focus of the laser beam and lifted 40 μm above the beam focus. See Section 4.4.4.

the Q value as both sets of data taken lie at the same value, suggesting that the dominant factor in trapping is the transparency of the partially coated sphere. Upon lifting the spheres up 40 μm into the sample using the optical tweezers, all the Q values converge to the similar values of 0.036±0.003 for single coated silver spheres, 0.033±0.004 for 10^{-4}M dye coated particles and 0.034±0.003 for the 10^{-6}M dye coated particles. This can be attributed to the fact that the dominant factor of the Q value, at this position, is the use of the objective lens away from its design conjugates. Q values for samples prepared in Tollen's reagent for periods greater than 60 minutes, where the reagent was refreshed (giving particles "twice coated" with silver), were not obtained as the trapping of the particles here was not possible.

4.5 Conclusions

4.5.1 Confirmation of SERRS from single silver coated silica microparticles in optical tweezers

It was confirmed that the spectrum recorded in the optical tweezers setup was SERRS as it correlated well with the spectrum recorded using the same dye on a silver colloid recorded in a dedicated Raman system. The use of different excitation wavelengths, for the optical tweezers and dedicated Raman systems, to give the same spectra corroborates the fact that it is the relative wavenumber shift for a particular molecule that is measured, as mentioned in Chapter 2.3.6. The fact that little or no signal was recorded for the silica microparticles with silver and the silica microparticles with dye further enforces the need for the dye to be adsorbed onto a metal surface in order to get the SERRS signal.

4.5.2 Visualising the SERRS signal

Spectra recorded on the spectrometer confirmed that the visual "flashes" coincided with a SERRS emission, with a bright visual "flash" corresponding to the most intense SERRS signals.

In the above cases, the SERRS active particles were not trapped by the laser beam, but interacted with the beam and were then repelled away. It is probable that these particles had a large amount of silver adsorbed onto their surface, with the most intense SERRS signals corresponding to the particles with the most silver and dye adsorbed onto their surface.

4.5.3 SERRS from spheres in the vicinity of the laser beam

The 532 nm focussed laser light in the optical tweezers was so intense that it was able to excite SERRS signals from spheres from up to few μm's away. This demonstrates that is it not necessary to trap a partially dye and silver coated sphere in order to stimulate a SERRS response for a period of up to a few (10) seconds, provided that the sphere was immobilsed and therefore would not be repelled by the laser light. This would also allow particles with large amounts of silver to be analysed, as they are more difficult to trap with an optical tweezers.

4.5.4 Effect of dye concentration on Q value of SERRS active particles

The addition of dye to the partially silvered microparticles lowered the Q value of the spheres when compared to the silvered microparticles, most probably because the azo dye absorbs strongly at 532 nm and therefore makes the particles more absorptive. Further into the sample cell, the trapping ability of the spheres was dominated by the use of the objective lens away from it design conjugates.

4.5.5 Conclusion

Interestingly, it was the particles with the weakest SERRS emission that were the easiest to trap. This may be indicative of the amount of silver coating on the surface of the sphere. In all cases, the SERRS from the particles stopped once the particles were trapped. This is most likely due to the fact that the dye was photobleached due to the intense laser beam.

The dye reduced the Q value of particles in the optical tweezers, as the dye makes the particle absorb the trapping light more strongly. However, the amount of silver on the surface still dominates whether the particle can be trapped easily or not. The stronger the dye concentration, the stronger the visual SERRS emission appears on the CCD camera.

Trapping of the silver and dye coated spheres in this instance was not a pre-requisite for stimulating a SERRS response. Upon trapping the SERRS emission only lasted about 100 ms. However, it was possible to obtain a longer SERRS signal (up to 10s) by immobilising the spheres on the bottom of the cover slip and letting them interact with the highly divergent laser beam. A solution to obtaining long (minutes) SERRS signals whilst being simultaneously trapped is discussed in Chapter 5.

This work has resulted in one publication in collaboration with the Department of Pure and Applied Chemistry at the University of Strathclyde.

• Graeme McNay, Frances T. Docherty, Duncan Graham, W. Ewen Smith, Pamela Jordan, Miles Padgett, Jonathan Leach, Gavin Sinclair, Paul B. Monaghan and Jonathan M. Cooper, "Visual observation of SERRS from single silver coated silica microparticles within optical tweezers", Angewandte Chemie, 43, 19, 2512-2514 (2004).

Chapter 5

Surface enhanced resonance Raman scattering in optical tweezers using co-axial second harmonic generation

A silica particle, partially coated with silver, in the presence of a suitable chromophore, such that it could be trapped using a standard 1064 nm TEM_{00} mode laser whilst still having sufficient metal to elicit a SERRS response activated by light at 532 nm was demonstrated. By focusing a 1064 nm laser through a biaxial, frequency doubling $KTiOPO_4$ (KTP or Potassium Titanyl Phosphate) crystal, it was possible to create a dual wavelength trap with different wavelengths used for trapping and activating the particle. Typically, several microwatts of green (532 nm) excitation light were introduced for each milli-watt of infra-red (1064 nm) trapping light passing through the KTP crystal. This SERRS signal was recorded from a stably trapped particle for a period of up to several minutes, with investigations into the photobleaching rate, for individually trapped particles, made as a function of trapping power. This novel configuration has clear applications in providing apparatus that can simultaneously manipulate a particle whilst obtaining sensitive

spectroscopic information.

5.1 Introduction

Previously, Raman spectroscopy and optical tweezers have been combined to study living biological cells with a near infra-red trapping laser as the excitation source [56]. The trapping prevents the particles from drifting out of the laser beam due to Brownian motion and also permits one particle to be studied at a time rather than an average signal from numerous species. However, only one in a million photons is Raman scattered so the resulting spectral emission is weak, and consequently long acquisition times were required which potentially result in radiation damage to the sample. The use of infra-red lasers allows biological samples to be trapped with less damage than if a visible wavelength laser was used [103, 5, 104] since samples are almost transparent to IR wavelengths. Optical tweezers have also been combined in a microscope to study resonance Raman (RR) of biological cells [55]. In this example an infra-red (830 nm) tweezing laser was combined with a Argon/Krypton laser confocal imaging system to produce the excitation wavelengths necessary to excite the resonance Raman response. However, this required a dual system comprising an optical tweezers and a confocal microscope, which separated the optical paths of the trapping and excitation lasers below and above the sample.

The problem preventing the technique described in Chapter 4 being used as a highly sensitive and selective bioanalytical method is that the powerful laser beam required for optical trapping photobleached the chromophore within 100 ms. This Chapter addresses that problem and demonstrates that

a sustainable SERRS spectrum can be achieved by trapping a partially silvered, dye coated particle in a 1064 nm TEM_{00} optical trap. The optical trap was formed using a 1064 nm laser, typically operating with an output power between 500 - 1000 mW. Prior to coupling the laser into the microscope objective, a frequency doubling $KTiOPO_4$ (KTP) crystal was inserted at an intermediate beam waist to produce 4 - 16 μW of 532 nm co-linear light. Both the IR and the green wavelengths suffer a loss within the coupling optics and objective lens of the order of 50% before reaching the trapping plane. This second harmonic generated light, at 532 nm, excites a surface plasmon in the silver, which interacts with the chromophore, and thus eliminates the need for separate trapping and excitation lasers or the associated optical complexity.

The particles, which are identical to the ones described in Chapter 4, contain a chromphore that has an absorption maxima and surface plasmon resonance close to the excitation wavelength of 532 nm. The resulting SERRS emission had distinct spectral peaks and could be recorded from a stably trapped particle for a period of up to several minutes. This ability to produce long-lasting SERRS signals within an infrared optical trap produces a highly controllable method suitable for ultra sensitive and selective bioanalysis of single particles.

5.2 Second harmonic generation

The process of converting 1064 nm wavelength light into 532 nm wavelength light is called "second harmonic generation" and can be done by focussing a laser beam through a non-linear crystal such as $KTiOPO_4$ (KTP). Second

harmonic generation, or frequency doubling, has been well documented in many texts and papers [105, 106].

In most cases there is a need for a high conversion efficiency from 1064 nm to 532 nm, but, for the experiment described in this Chapter, only a few μW of 532 nm light needs to be generated.

5.3 Experimental setup and materials

5.3.1 Optical tweezers setup

The optical tweezers setup for this experiment was similar to that described in Chapter 4.2.1. However, for this experiment, the green 532 nm laser was replaced with a variable power, 1064 nm Laser Quantum Ventus (Photonics Solutions, Germany) with a maximum output power of 3W. The beam was expanded, collimated and passed through a telescope, the focal point of which fell onto a KTP frequency doubling crystal that generated microwatts of power at 532 nm. All the powers quoted in this Chapter (for both the 1064 nm and 532 nm light) correspond to the power in the trapping plane of the optical tweezers, measured using a Newport 1815-C power meter positioned before the laser beam entered the beamsplitter. The partially dye and silver coated particles, as described in Chapter 4.2.2, were viewed using a CCD camera (Pulnix, Denmark) protected with filters (Edmund Optics, UK) to remove both the infra-red wavelengths and the green excitation light. This experimental setup is shown in Figure 5.1. The SERRS spectrum was recorded by coupling a fiber optic cable, imaged onto the sample plane, to an Ocean Optics R2001-532 Raman spectrometer (Ocean Optics, UK). The fibre diameter of 600 microns corresponds to a diameter of 6 microns in the sample plane, i.e. slightly larger than a single particle.

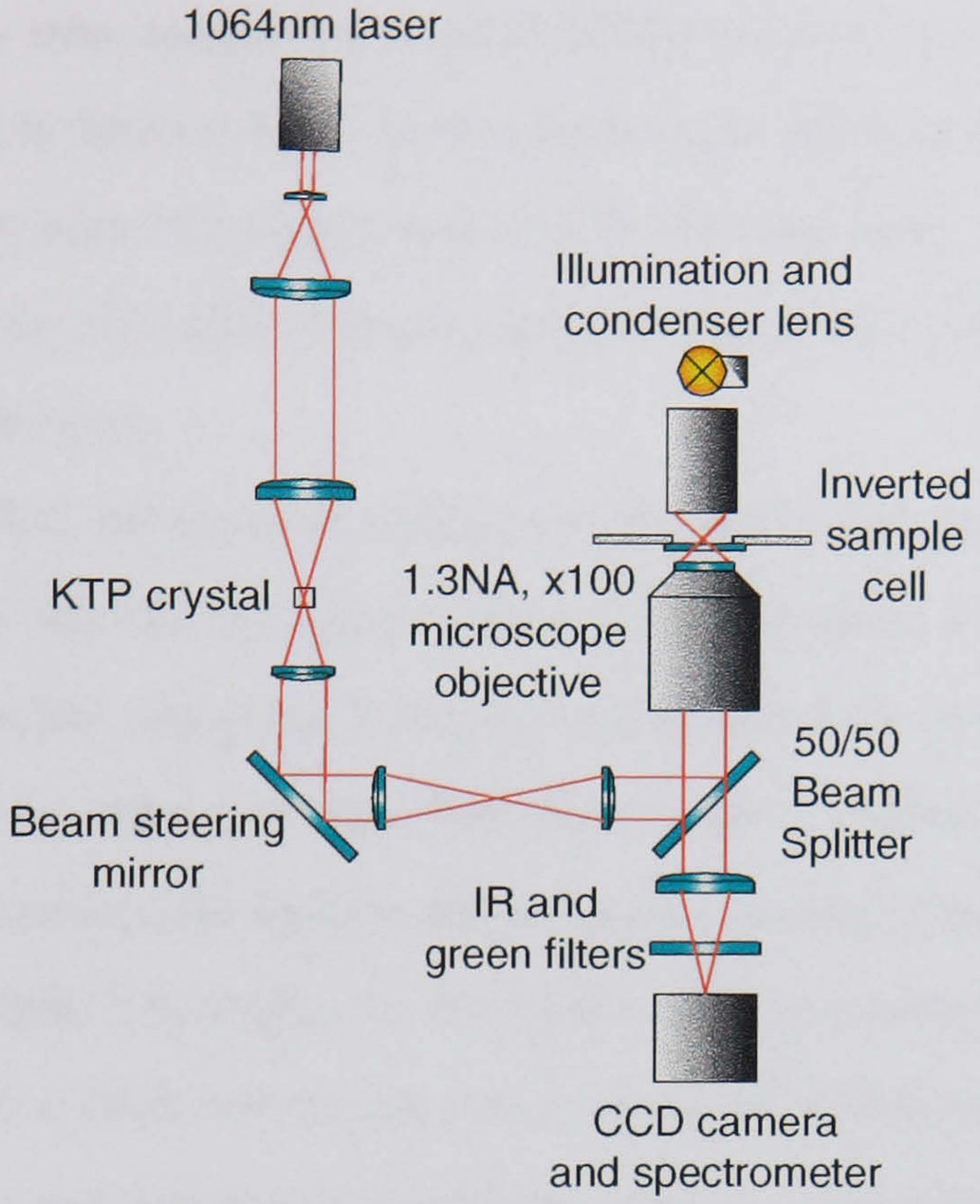

Figure 5.1: The experimental setup for the infra-red laser with green light introduced via a frequency doubling KTP crystal. See Section 5.3.1 for details.

5.3.2 SERRS active microparticles

The partially silver and dye coated particles were the same as, and were made in the same way as, those described in Chapter 4.2.2. Here, the partially silvered spheres were modified using a 10^{-4}M 3,5-dimethoxy-4-(6-azobenzotriazol)-phenylamine dye solution adsorbed onto their surface.

5.4 Methods

5.4.1 SERRS in dual wavelength optical tweezers

200 μl of solution containing dye and silver modified silica spheres were placed into a sample cell in the optical tweezers. Individual partially silvered, dye

coated particles were trapped and their SERRS spectra recorded, using the setup described in Section 5.3.1, with a 2s integration time on the spectrometer. A 1064 nm laser trapping power of 436 mW was used. Inserting a KTP crystal introduced 10.9 μW of green excitation light into the trapping plane of the optical tweezers.

To confirm that the spectral emission measured in the optical tweezers using the OR2001-532 Raman spectrometer (Ocean Optics, UK) was SERRS, the spectra recorded using this setup was compared with the SERRS spectra recorded from the same dye adsorbed onto a silver colloid taken in a dedicated Raman system (Renishaw 2000 Raman Microprobe, Renishaw Plc, UK) at Strathclyde University. In the optical tweezers setup, the laser beam was blocked and a dark current spectrum recorded which was automatically subtracted from any subsequent recorded spectra. The experiment was repeated using silica particles coated only with silver for comparison. As in Chapter 4, the spectra from dye adsorbed on colloidal silver was acquired using a Renishaw 2000 Raman Microprobe with a CCD spectrometer. The excitation was provided by a Spectra-Physics Model 2020 argon-ion laser with a wavelength of 514.5 nm and 3 mW of power at the source (Renishaw Plc, UK).

5.4.2 The decay rate of the intensity of the SERRS emission

200 μl of solution containing 10^{-4}M 3,5-dimethoxy-4-(6-azobenzotriazol)-phenylamine modified silvered spheres were placed in the sample cell of the optical tweezers. The decay rate of the intensity of the SERRS emission of several such SERRS active particles were consequently investigated using the Ocean Optics R2001-532 Raman spectrometer with an integration time of 2s,

for the 1352 cm^{-1} Raman shifted peak, and dark current subtraction. This experiment was carried out using laser trapping powers of 365 mW (with the KTP crystal introducing 9.3 μW of green excitation light), 436 mW (introducing 10.9 μW of green excitation light) and 510 mW (with 15.3 μW of green) at the trapping plane respectively. Once a bead was trapped in the dual wavelength trap, the decay rate of the intensity of the 1352 cm^{-1} Raman shifted peak was recorded until either the signal became indistinguishable from the background or the bead fell out of the trap. This was repeated for six beads for each of the three trapping powers.

The decay rate of the intensity of the SERRS emission for such particles can be described by Equation 5.1.

$$I = I_0 e^{-kt} \tag{5.1}$$

where I_0 is the intensity of the signal at time $t = 0s$. I is the intensity of the signal after a time t and k is the rate of decay of the SERRS emission (photobleaching rate).

If the decay rate of the intensity of the SERRS emission is exponential, then taking the log of either side of this equation and plotting Log(Intensity) against time will yield a graph with a straight line and a negative gradient. This allows the decay rate of the intensity of the SERRS emission k to be calculated from the gradient of the line. This analysis was done using Microsoft "Excel".

5.4.3 SERRS spectral response to trapping power

In order to investigate how the trapped SERRS active particles responded to a change in trapping power, a series of experiments were carried out. 200

μl of the solution described in Section 5.3.2 was placed in the sample cell of the optical tweezers. Prior to experiments, a calibration curve of the green excitation power against input IR power was plotted by measuring the IR input power to the KTP crystal and the amount of green excitation power exiting the crystal with the appropriate filters in place. Analysis was done using Microsoft "Excel".

Firstly, an individual particle was trapped, released and re-trapped by the laser to see how the intensity response of the 1352 cm^{-1} Raman shifted peak for an individual particle was effected. A single active particle was trapped, released and re-trapped using a 436 mW IR laser beam, which introduced 10.9 μW of green excitation light into the trapping plane. Again, the dark current spectrum was automatically subtracted from the results.

Secondly, a cluster of particles were trapped and the laser power varied between 222 mW and 510 mW, introducing 3 μW and 15.3 μW of excitation light respectively and the spectral intensity of the 1352 cm^{-1} Raman shifted peak investigated with a 2s integration time on the spectrometer. The IR power was varied from zero W to 510 mW, 365 mW, 510 mW, 365 mW, 222 mW, 365 mW and finally back to 510 mW. This introduced zero W, 15.3 μW, 9.3 μW, 15.3 μW, 9.3 μW, 3 μW, 9.3 μW and 15.3 μW of green excitation light into the sample.

This was repeated with a single trapped SERRS active particle with IR laser powers between 365 mW (9.3 μW of green) and 510 mW (15.3 μW of green). The laser power was changed from 510 mW (15.3 μW of green), to 365 mW (9.3 μW of green), back to 510mW, 365 mW and finally 510 mW.

5.5 Results and discussion

5.5.1 SERRS in dual wavelength optical tweezers

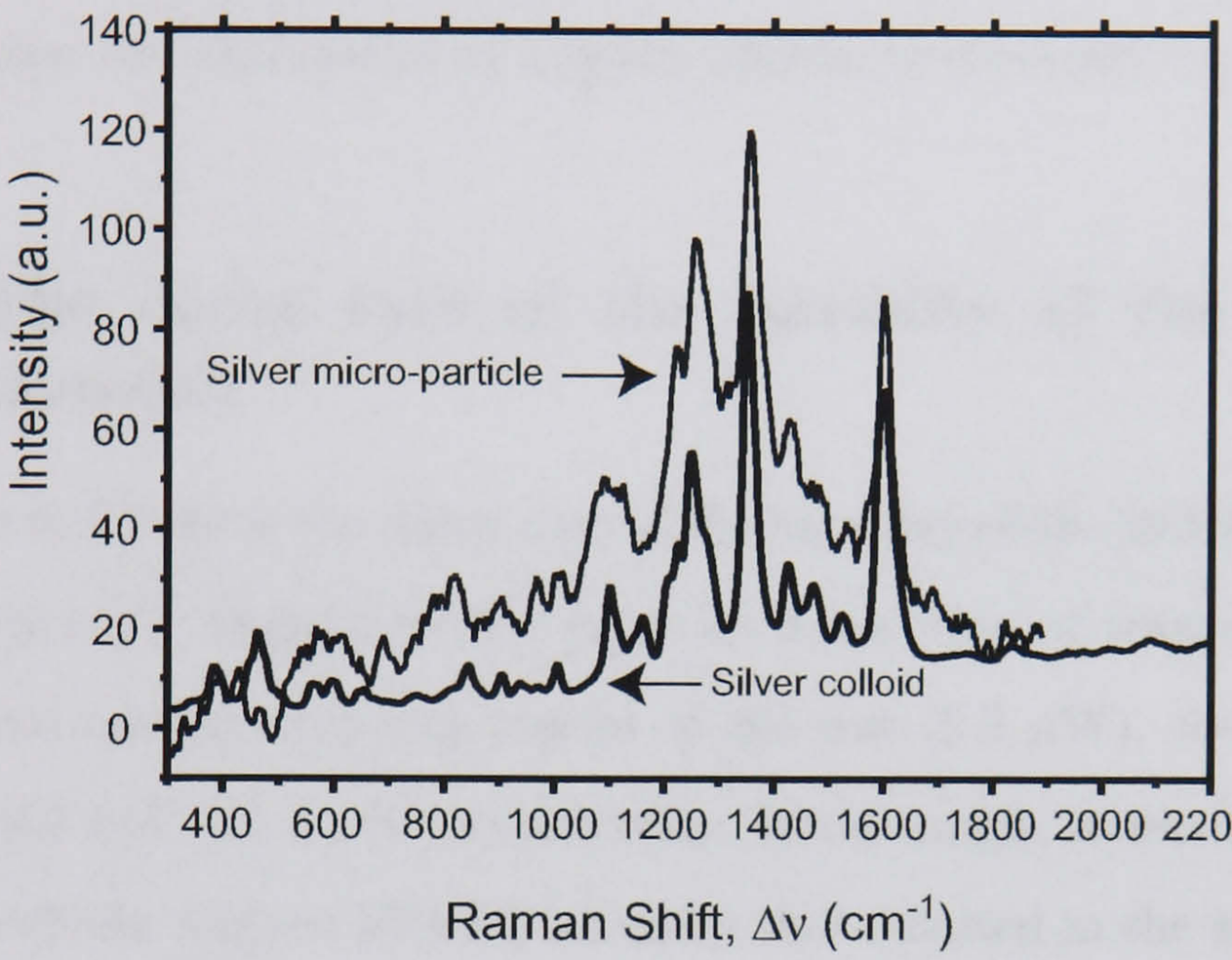

Figure 5.2: Comparison between the SERRS spectra collected from the IR SERRS setup and that collected from dye adsorbed onto a silver colloid and recorded in a dedicated Raman system. The spectra from the silver colloid was re-scaled from Figure 4.1(b). See Section 5.4.1 for more details.

As shown in Figure 5.2, the two spectra, taken using the optical tweezers and the dedicated Raman system, are in agreement. The spectra from the silver colloid was re-scaled from Figure 4.1(b). No signal was observed when dye was adsorbed onto plain silica particles and trapped in the optical tweezers as illustrated in Figure 4.1, confirming that the SERRS active particles do have a partial metallic coating that was not ablated before trapping. The fact that there is good agreement between the spectra shows that the emission from the particle really was a SERRS effect. If the emission had been fluorescence then the spectra would be different and identification of the different Raman bands would be unlikely.

In all of the experiments described in this Chapter, SERRS was detected only when the green excitation light was present. No SERRS was observed arising from two photon excitation from an IR (1064 nm) trapping laser implying that the absorption of a green photon is necessary for SERRS to occur.

5.5.2 The decay rate of the intensity of the SERRS emission

Figures 5.3 to 5.5 show the decay rate of the intensity of the SERRS emission for the 1352 cm^{-1} Raman shifted peak for a selection of trapped particles with infrared (green) trapping powers of 365 mw (9.3 μW), 436 mW (10.9 μW) and 510 mW (15.3 μW) respectively. Interestingly, it was the trapped particles with the highest SERRS intensity that resulted in the spectra with the longest half-life. The particles that were initially less intense tended to photobleach quicker, but all the particles gave distinct SERRS spectra for up to 4 minutes. After this time, the signal either became indistinguishable from the background noise or the particle escaped from the optical trap.

The rate of decay of the SERRS emission, k, for the SERRS signal from the trapped particles illustrated in Figure 5.3, which introduced 9.3 μW of green excitation light, varied from 2 ms^{-1} ($R^2 = 0.8$) to 67 ms^{-1} ($R^2 = 0.6$). From Figure 5.4, with 10.9 μW of green excitation light, the rate of decay of the SERRS emission varied between 2 ms^{-1} ($R^2 = 0.6$) and 10 ms^{-1} ($R^2 = 0.6$), while the rate of decay of the SERRS emission in Figure 5.5, introducing 15.3 μW of green excitation light, varied between 2 ms^{-1} ($R^2 = 0.9$) and 32 ms^{-1} ($R^2 = 0.8$).

The R^2 value, also known as the coefficient of determination, is an indicator range between 0 and 1 and reveals how close the estimated values of the

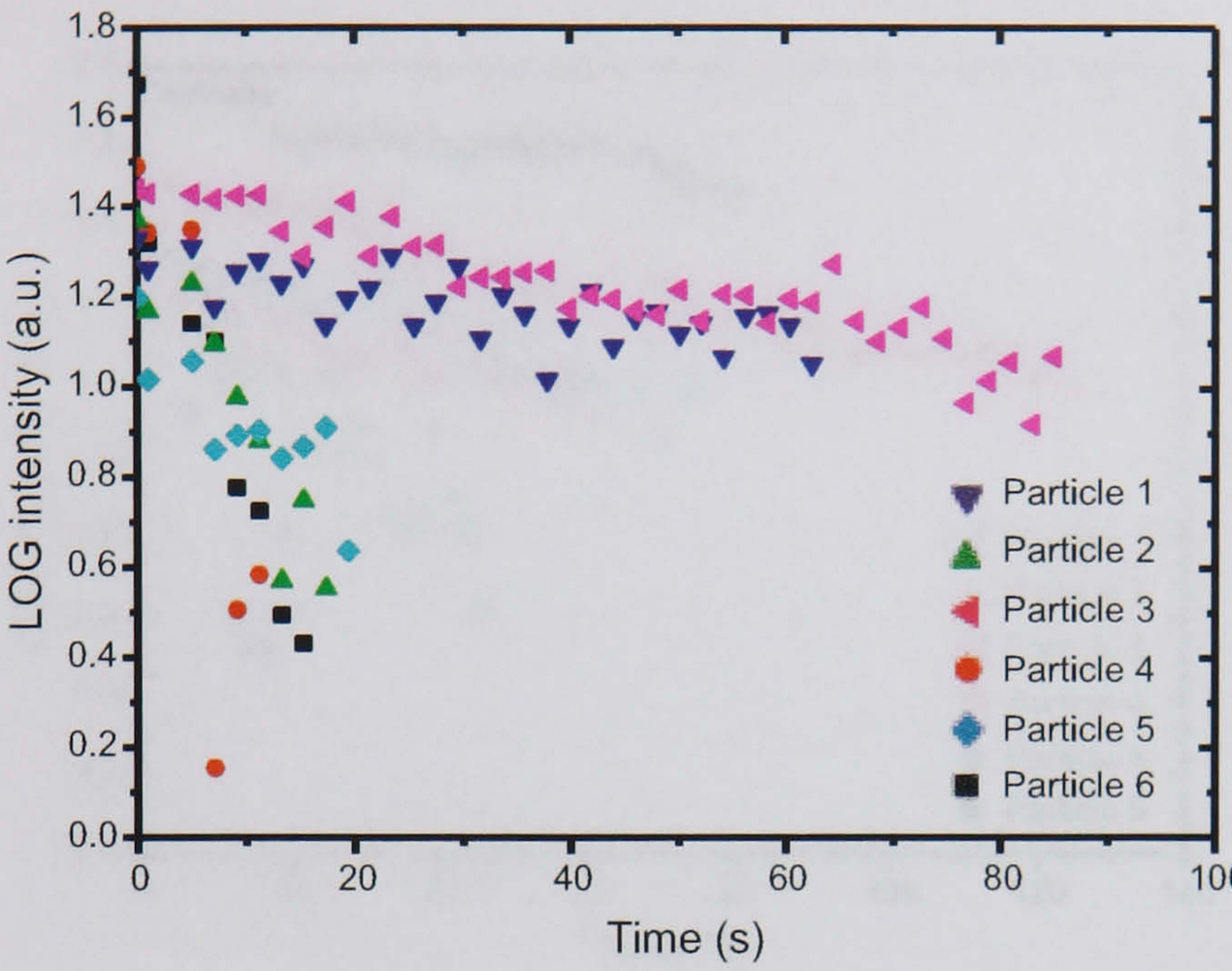

Figure 5.3: The decay rate of the intensity of the SERRS emission values for the 1352 cm^{-1} Raman shifted peak for several partially dye and silver coated particles trapped in a 365 mW IR laser beam passed through a KTP crystal. Refer to Section 5.4.2 for more details.

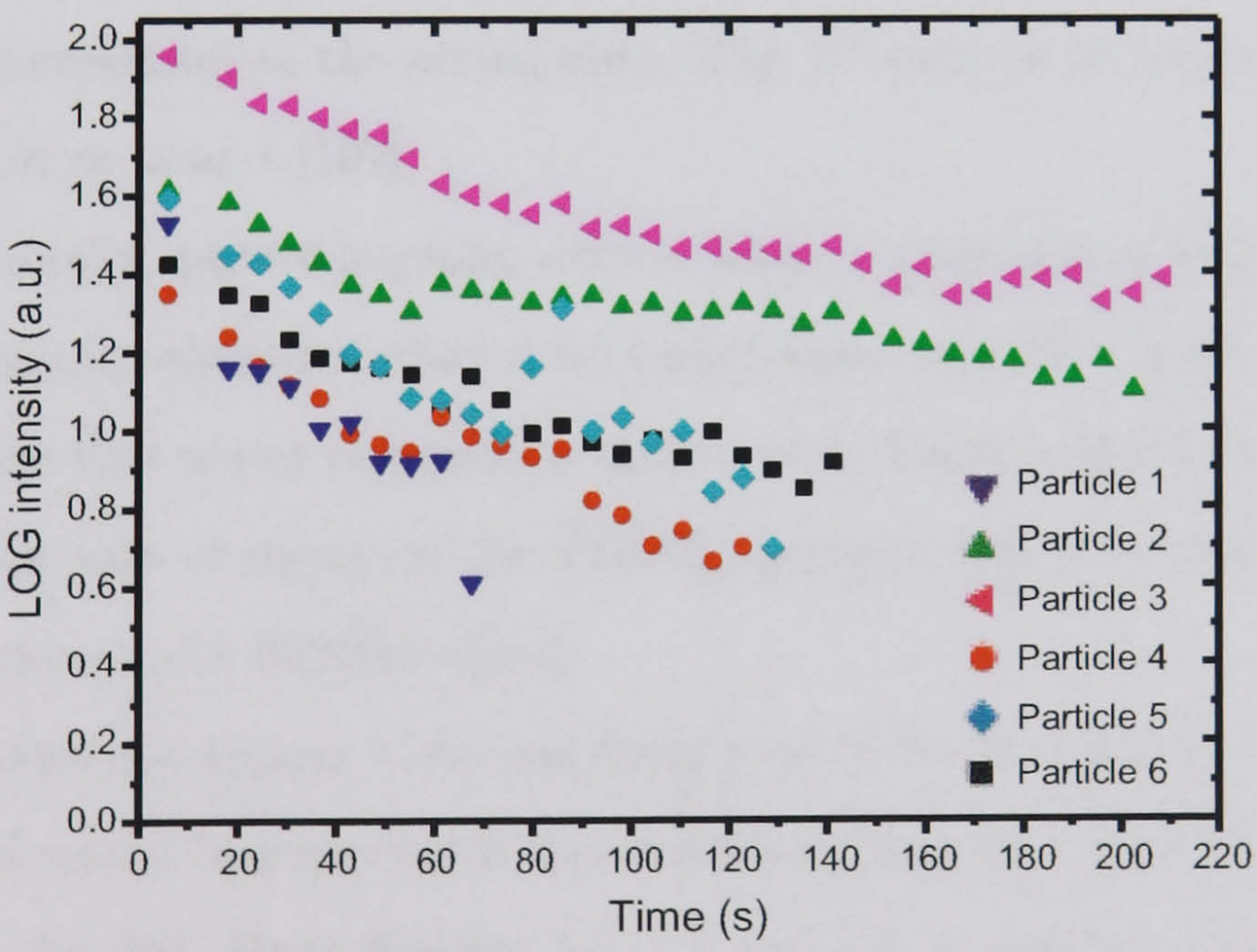

Figure 5.4: The decay rate of the intensity of the SERRS emission values for the 1352 cm^{-1} Raman shifted peak for several partially dye and silver coated particles trapped in a 436 mW IR laser beam passed through a KTP crystal. See Section 5.4.2 for further details.

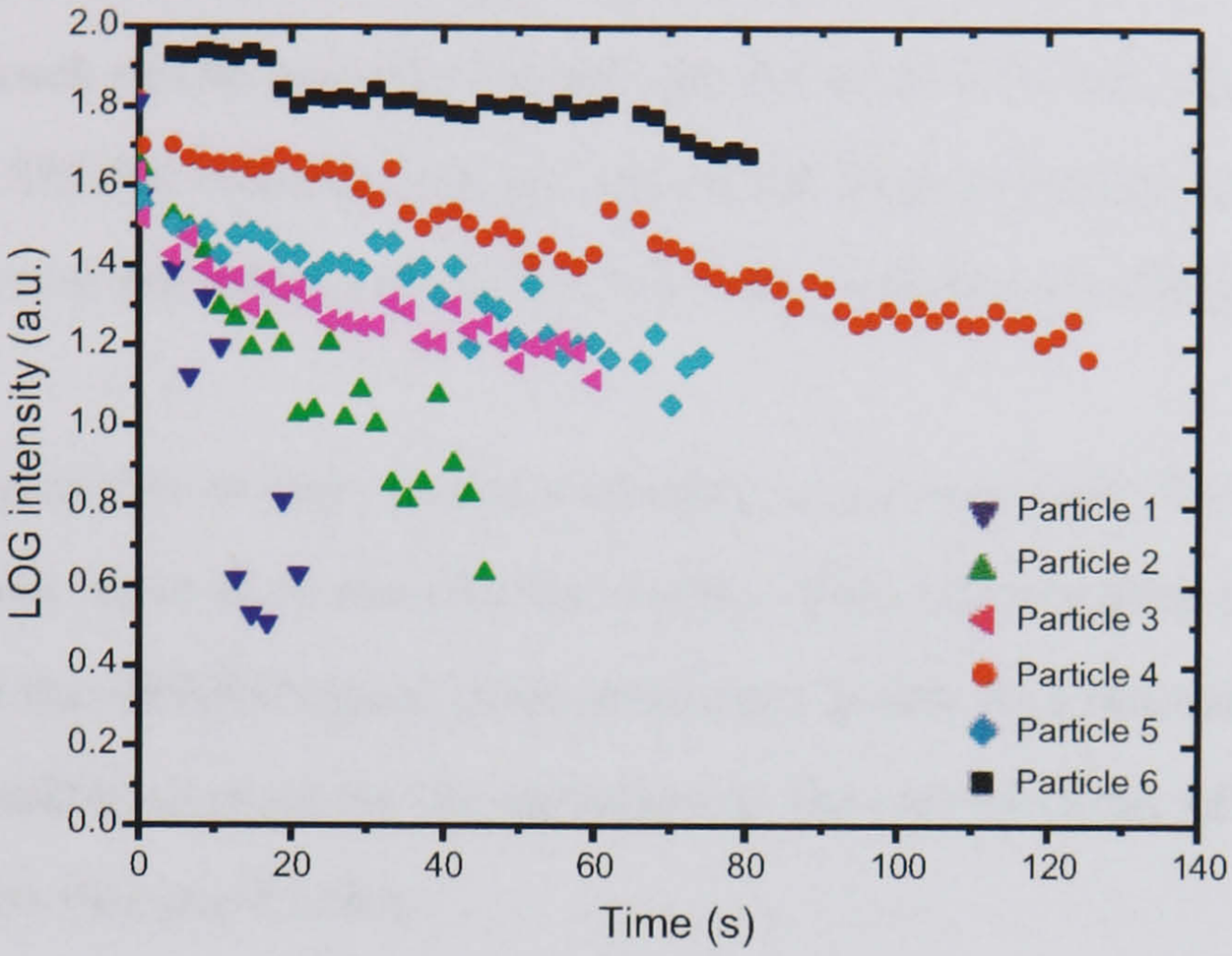

Figure 5.5: The decay rate of the intensity of the SERRS emission values for the 1352 cm^{-1} Raman shifted peak for several partially dye and silver coated particles trapped in a 510 mW IR laser going through a KTP crystal. See Section 5.4.2 for more details.

trendline correspond to the actual data. The R^2 value is at its most reliable when it is at or near 1 [107].

Traditionally, photobleaching occurs when a fluorophore is irreversibly, photochemically altered so that it no longer fluoresces [108], although it is a phenomenon that is not completely understood. There may be other factors affecting the rate of decay of the SERRS emission (photodecomposition or photobleaching) of a SERRS signal.

There does not appear to be one decay rate of the intensity of the SERRS emission as would be expected if the photobleaching rate was totally dependent upon the dye. From Figures 5.3, 5.4 and 5.5, it appears that there are a selection of photobleaching rates for each input laser power which indicate that there are different enhancements involved in the process of photobleaching the SERRS signal. The different intensities of the different trapped par-

ticles suggest that there are different amounts of dye and/or silver on the surface of each of the partially coated spheres while the different rates of decay of the SERRS emission suggest that there may be an increase of oxygen within the sample over time which can lead to faster photobleaching rates [109].

The first source of error is that the decay may not actually be exponential, in which case there is an error in the model. This also suggests that the rate of decay of the SERRS signal varies with laser power in a non-trivial matter. Further possible reasons for the variation in the rate of decay of the SERRS emission are discussed below.

Variability within SERS

The variability of the SERS amplitude is a well known but not completely understood phenomena.

Glass *et al* [80] observed that, for different dyes adsorbed onto silver islands, that the maximum luminescence intensity was obtained when the dye absorption maximum overlapped the maximum of the metal plasmon resonance. The maxima of this resonance was shifted by varying the thickness of the silver film between 0-10 nm. The minimum luminescence intensity, for a dye adsorbed onto different silver thicknesses, was up to 80% less than the maximum luminescence intensity. Decreases in luminosity were observed when the metallic layers were made thinner or thicker than 7 nm. See Chapter 2.3.7 for more detail on Mie theory and how it effects the lambda max for different metal thicknesses.

It is clear that, from the TEM images of the particles shown in Figure 3.4, that the thickness of the colloidal silver deposits on the surface of the sphere

vary in size between zero nm and 100 nm. This can shift the surface plasmon resonance with respect to the incident excitation light as explained in Chapter 2.3.7. Furthermore, the dye molecules can orient themselves horizontally or vertically onto the metal surface. This could be sufficient to change the photochemistry of the surface enough to result in different photobleaching rates due to enhanced or increased radiative and non-radiative decay paths.

The fluorescence of a molecule on SERS-active surfaces was thought to be dependent on three factors: the enhanced electromagnetic field, enhanced absorption and the nonradiative processes which transfer the excitation from the excited molecule to the metal through several decay channels [50].

Inspired largely by SERS, the effect of surface geometry on the decay rate of a molecule close to a small metal sphere was studied [110, 111, 112, 113]. Collectively, the results implied that, close to the metal sphere, the decay rate varied as $1/d^3$ where d is the molecule-metal separation. It was also found that the decay rates depended on the size and shape of the metal particle, the orientation of the molecule on the surface and the molecule-metal separation in a non-trivial manner [110]. The fastest decay rate was found not to be at the metal surface but at a small (nm) distance above it. Experimental results showing this have been reported [82].

As with enhanced fluorescence, Nitzan and Brus [111, 112] realised that the optimum position for the rapid photobleaching (photodecomposition) of molecules adsorbed onto a metal surface may not be directly on the surface but a short distance above it [50].

Vasilev *et al* [114] studied the photobleaching of a chromophore close to a metal surface in 2004. They concluded that the metal interface influenced the chromophore in two ways. Firstly, the excitation rate was altered due to

the local enhancement of the electromagnetic field and secondly, the electromagnetic decay rate was altered. It was found that there was a maximum photobleaching rate at a short distance above the metal, 25 nm. The metal-enhanced emission lead to a longer chemical lifetime when the chromophore was closer to the metal, while further from the metal, the photobleaching rate decreased due to decreasing excitation rates. In short, they found that for distances less than 20 nm, the strongly increased electromagnetic decay rate allowed the chromophore to undergo more excitation-emission cycles before photobleaching while the longer lifetime for larger distances was as a result of a decrease in excitation rate.

The enhanced photobleaching of single molecules in a dual wavelength optical trap has also been investigated [115]. These results concluded that single molecule fluorescence spectroscopy within optical tweezers demonstrated increased photobleaching rates due to the additional photobleaching of the fluorophore by the trapping laser beam. It was postulated that additional channels for the photobleaching of dyes became available when used in an optical tweezers configuration.

Walk off effects of the KTP crystal

It is already known that several factors can influence the photobleaching rates of molecules. The most obvious way to increase the rate is to increase the excitation intensity. However, there is evidence that two photon excitation enhances photobleaching rates compared to one photon excitation [116, 117]. Other possible factors that could affect the SERRS response, giving us a range of photodegradation rates, include the orientation of the metal and dye with respect to the small amount of incident excitation light. This last

point is important because the green and IR light in this experimental setup may not be exactly co-focal. Once focussed, the IR and green focal points are separated in the optical tweezers trapping plane by ca. 2 μm as illustrated in Figure 5.6. This is due to the walk off effects of the birefringent KTP crystal

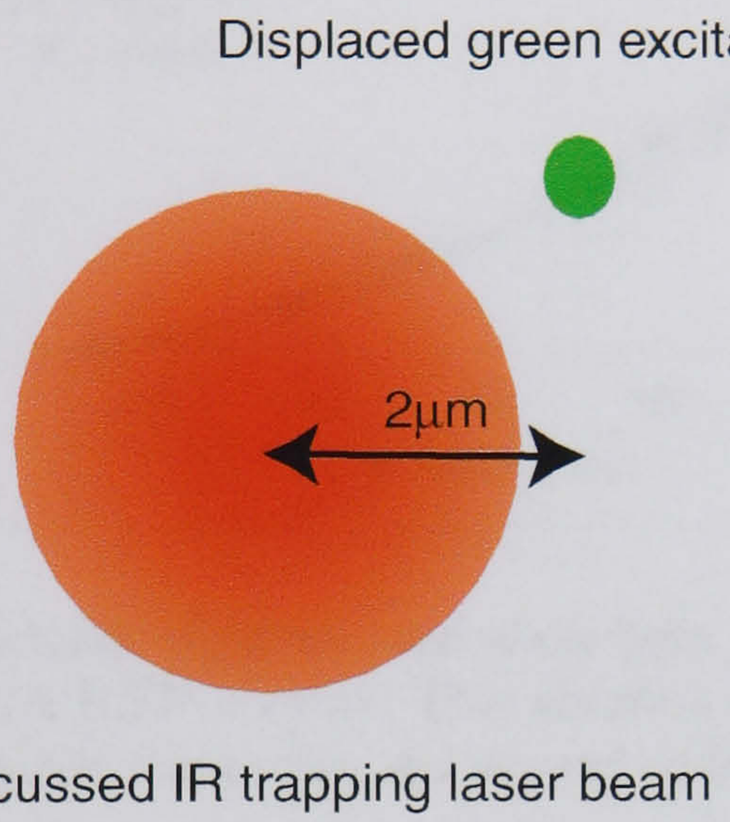

Figure 5.6: The focal points of the IR trap and the green excitation light are displaced within the optical tweezers by less than 2 μm due to the walk off between different wavelengths through the frequency doubling KTP crystal. Refer to Section 5.4.2 for further details.

as mentioned in Section 5.2. As the 1.5 μm diameter, partially silvered particles are trapped in the IR laser beam, the green excitation light lies on the periphery of the silver and dye coated bead. This means that the excitation intensity is not uniform across the whole of the trapped particle.

The particles may also be inadvertently damaged due to the high laser power and scattered light within the high NA optics used in the setup. This could cause radiation induced heating and therefore lead to surface degradation. If a particle only has a thin layer of silver on its surface rather than a large deposit, the laser might just penetrate the silver and damage it, resulting in a faster photobleaching rate.

5.5.3 SERRS spectral response to trapping power

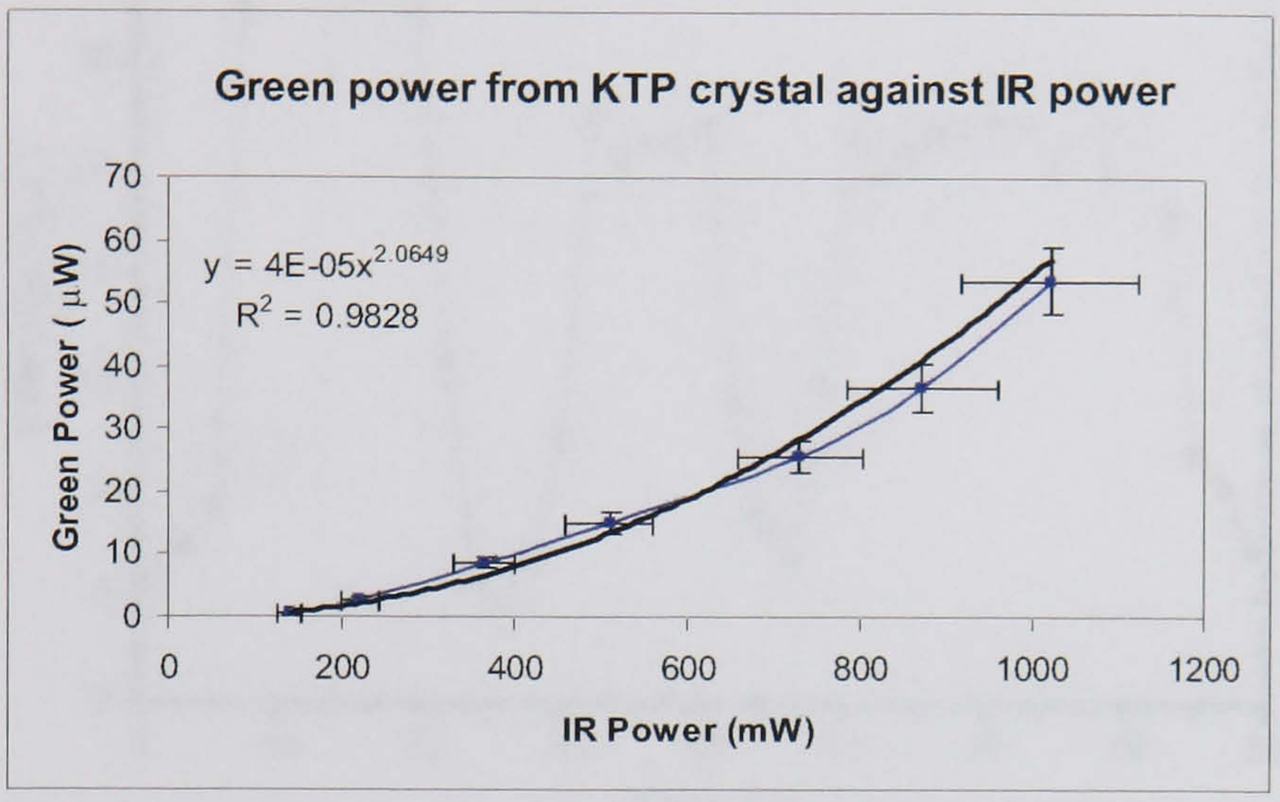

Figure 5.7: The intensity of green excitation light generated for an IR input laser beam through a KTP crystal. This shows a square relationship as expected since two photon excitation is a second order effect. See Section 5.4.3 for more details.

From the calibration curve, Figure 5.7, it can be seen that μW of green excitation power are generated from mW of IR power passing through the KTP crystal with a squared dependence, $Green\ excitation\ power\ (\mu W) = 4\times10^{-5}\ (IR\ power\ (mW))^{2.0649}$. This is due to the fact that second harmonic generation is a second order effect. The R^2 value here of 0.9828 is close to 1, suggesting a reasonable fit between the trendline and the data. Errors of $\pm10\%$ were assumed for the power measurements in both the IR and green power and was to compensate for the fluctuations in the input IR laser power.

The resulting SERRS intensity for the 1352 cm^{-1} Raman shifted peak is shown in Figure 5.8 for a single particle that was trapped, released and re-trapped using a 2s integration time. The particle escaped the trap when the co-focal laser beam was blocked using a beam stop at an intermediate position before the beam entered the back of the objective lens. When the

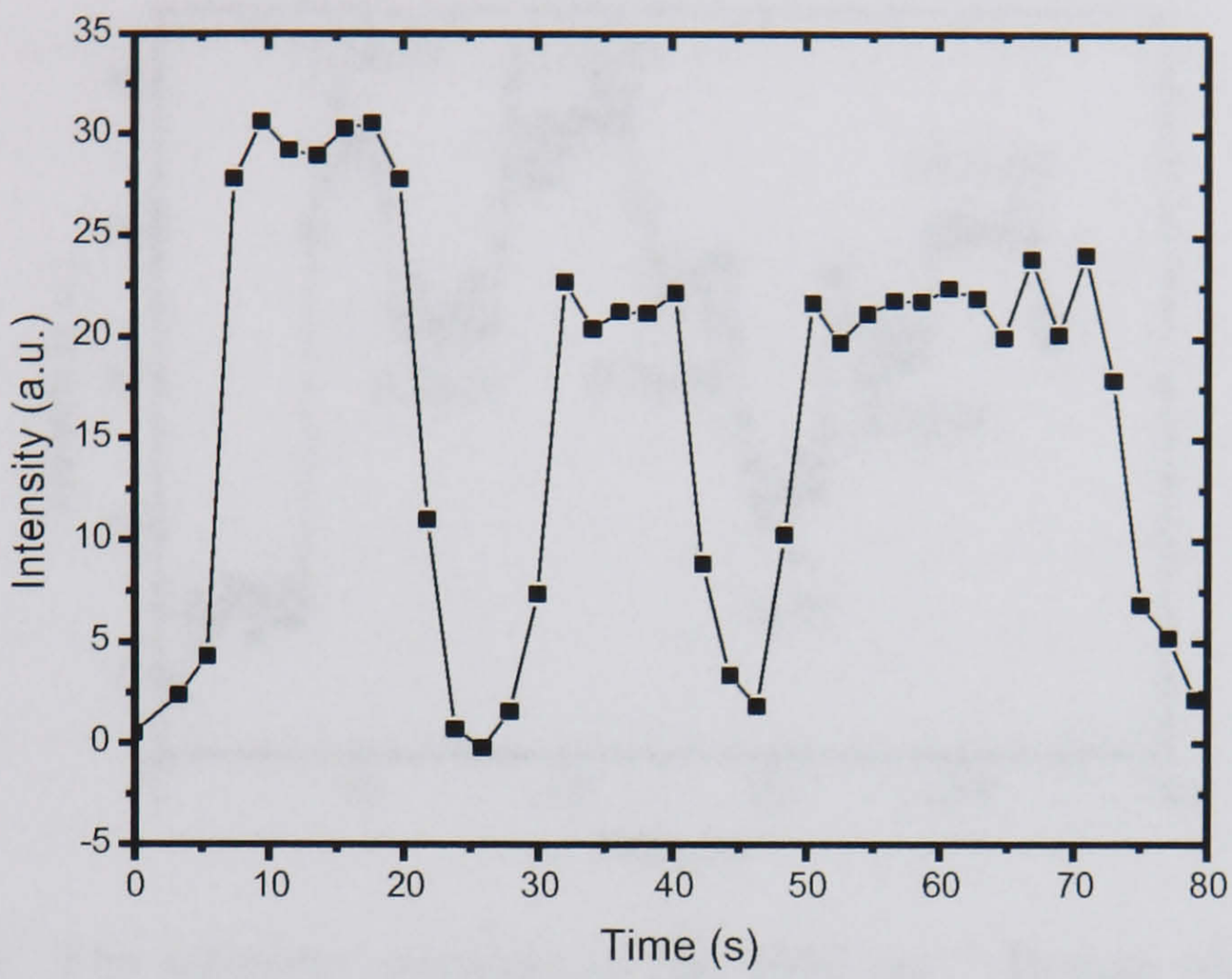

Figure 5.8: The intensity response of the 1352 cm^{-1} Raman shifted peak taken from a SERRS active particle trapped in a 436 mW IR laser beam with 10.9 μW of green light after passing through a KTP crystal. The particle was trapped, released and re-trapped. See Section 5.4.3 for more details.

bead was not in the optical trap, the intensity decreased to noise levels. Upon re-trapping, the signal returned to the intensity value prior to its release and continued to photobleach.

Figure 5.9 shows the changes in SERRS intensity for a small trapped cluster. The IR power was varied from zero W to 510 mW, 365 mW, 510 mW, 365 mW, 222 mW, 365 mW and finally back to 510 mW. This introduced zero W, 15.3 μW, 9.3 μW, 15.3 μW, 9.3 μW, 3 μW, 9.3 μW and 15.3 μW of green excitation light into the sample. The intensity "fall off" for a cluster was less rapid than that for a single trapped particle, and as a result it was possible to vary the trapping power of the laser beam and see the SERRS signal vary correspondingly. It was possible to vary the green excitation laser power from 15.3 μW, to 9.3 μW, repeat this and see the SERRS signal, on

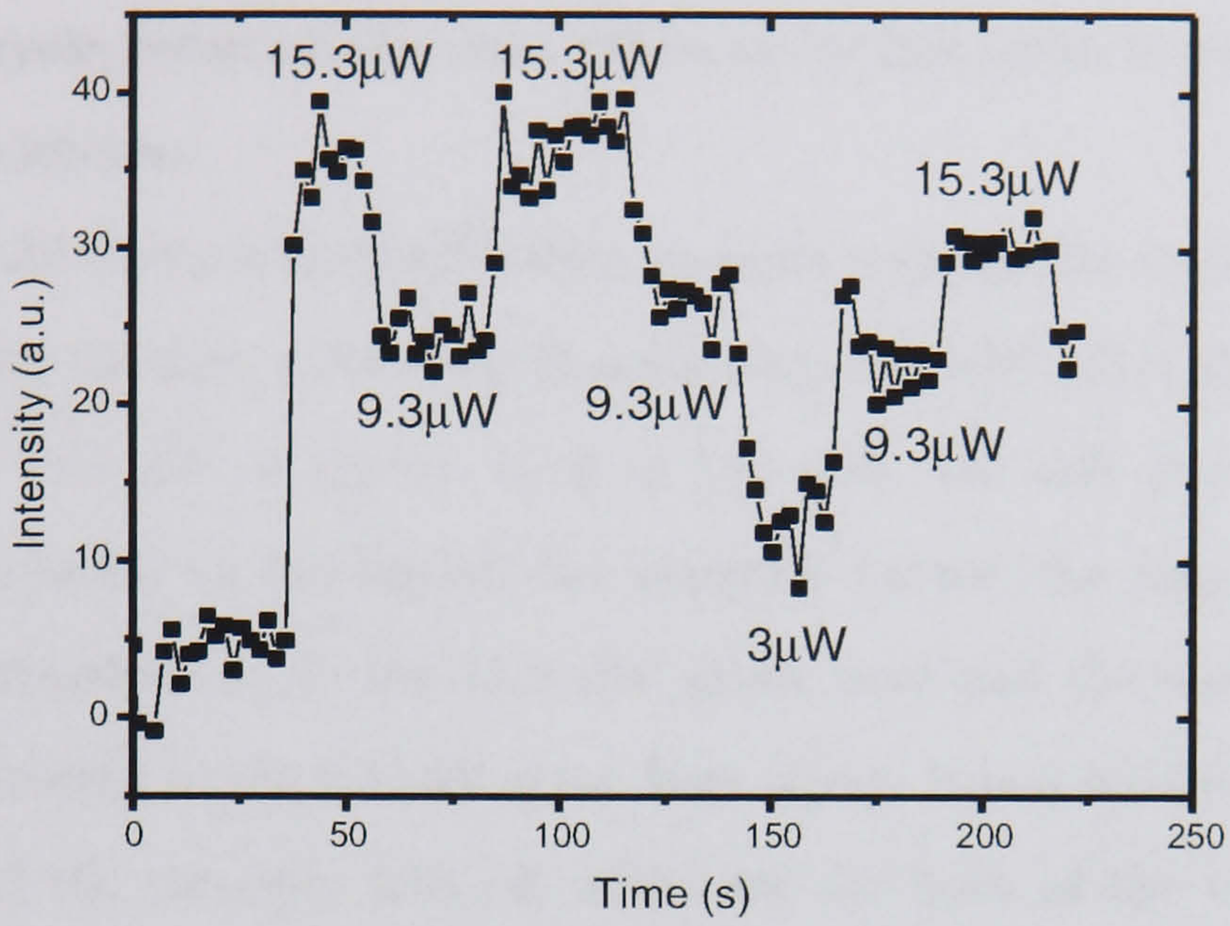

Figure 5.9: The intensity response of the 1352 cm^{-1} Raman shifted peak of an optically trapped SERRS active cluster taken using IR laser passed through a KTP crystal, from a trapped cluster with the green excitation power varied from 15.3 μW, 19.3 μW, 15.3 μW, 9.3 μW, 3 μW, 9.3 μW to 15.3 μW with an integration time of 2s. See Section 5.4.3 for more details.

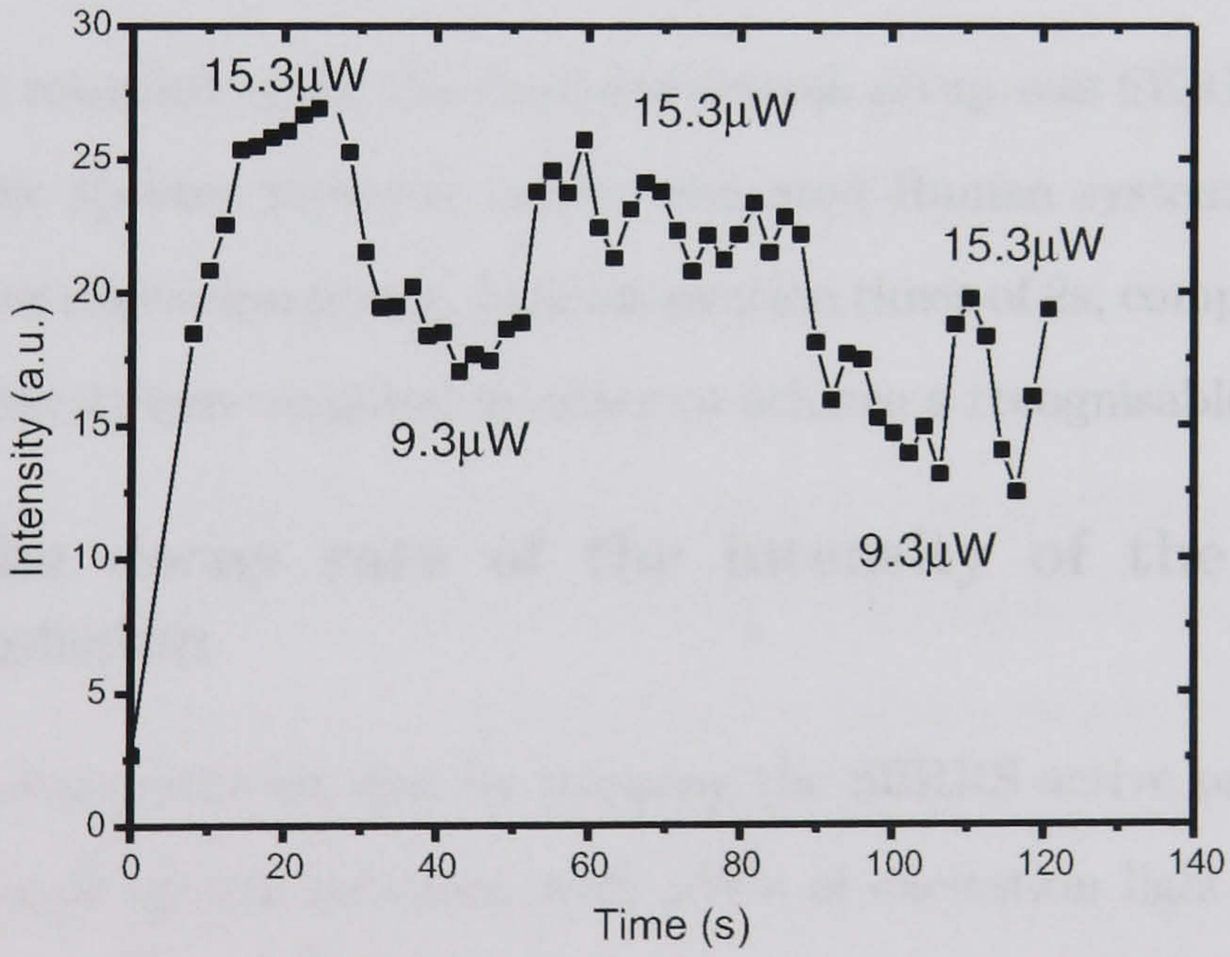

Figure 5.10: The intensity response of the 1352 cm^{-1} Raman shifted peak of an optically trapped SERRS active paricle taken using IR laser passed through a KTP crystal. Single trapped particle with green excitation power varied from 15.3 μW, 9.3 μW, 15.3 μW, 9.3 μW and back to 15.3 μW with a 2s integration time. See Section 5.4.3.

the second cycle, return to the same values as the first cycle, before the signal became less intense.

Figure 5.10 shows a similar SERRS intensity response for a single trapped particle where the laser power was changed from 510 mW (15.3 μW of green), to 365 mW (9.3 μW of green), back to 510 mW, 365 mW and finally 510 mW. It is possible to distinguish two separate curves, the higher intensity response corresponding to the 15.3 μW green laser and the lower intensity one corresponding to the 9.3 μW green laser input. It was interesting to note that both of the intensity falls off with time for both of the curves taken using the 15.3 μW and 9.3 μW green beams.

5.6 Conclusions

5.6.1 SERRS in dual wavelength optical tweezers

The spectra recorded using the dual wavelength setup was SERRS and was similar to the spectra recorded in the dedicated Raman system. However, due to the low excitation power, long integration times of 2s, compared to 100 ms in Chapter 4, were required in order to achieve a recognisable spectrum.

5.6.2 The decay rate of the intensity of the SERRS emission

It has been demonstrated that by trapping the SERRS active particles in a dual wavelength optical tweezers, with μW's of excitation light introduced for mW's of trapping light, it was possible to excite a SERRS signal that lasted for up to 4 minutes.

The decay rate of the intensity of the SERRS emission varied between 2 ms^{-1} and 67 ms^{-1} for an incident laser power trapping different particles,

suggesting that the rate of decay of the SERRS signal varied with laser power in a non-trivial matter. The rate of decay of the SERRS emission may not be an exact exponential decay as a result.

5.6.3 SERRS spectral response to trapping power

It has been shown that the intensity of the SERRS response is indeed sensitive to the input trapping, and respective excitation. power. By varying the trapping power between 436 mW and zero mW, it was possible to observe that the SERRS active particle did not recover to its maximum intensity once trapped, released and re-trapped. By trapping clusters, and a single particle, and varying the input power over the lifetime of the particle, it was possible to see that the intensity varies linearly with the green excitation power.

5.6.4 Conclusion

It has been shown that, by introducing small quantities of 532 nm light into an infra-red optical trap via a frequency doubling KTP crystal, it was possible to record a SERRS signal from the trapped particle that was sustainable over a period of a few minutes. This ability to trap partial metallic beads to create a combined SERRS and optical tweezers system provides an attractive platform for microsystems and microfluidic technologies in which sensory particles can be independently manipulated both with respect to each other and/or other entities. Furthermore, the use of an IR laser makes the whole system more biologically friendly than if a visible wavelength laser was used, resulting in less damage to the sample. By combining the spectroscopic nature of SERRS with the ability to trap and manipulate these beads, it will in future be possible to develop new platforms, such as biological probes, that can readily compete with those being developed using fluorescence.

The work presented in this Chapter has resulted in one journal publication:

- Pamela Jordan, Jonathan M. Cooper, Graeme McNay, Frances T. Docherty, W. Ewen Smith, Gavin Sinclair and Miles Padgett, "Surface enhanced resonance Raman scattering in optical tweezers using co-axial second harmonic generation", Optics Express, 13, 11, 4148-4154 (2005).

Chapter 6

Holographic optical tweezers

Optical tweezers use tightly focussed beams of laser light to trap and move micron sized objects within a microscope. Holographic, i.e. diffractive, optical components can be introduced into the tweezers and used to split the beams so that many objects can be trapped simultaneously. In addition to introducing lateral displacements, holograms allow particles to be displaced axially along the laser beam, giving full 3D control of trap positions.

6.1 Introduction

Limitations have previously existed as to the applications of optical tweezers as only one particle could be usefully trapped in a single laser beam. The adaptation of optical tweezers to trap two or more objects has previously been demonstrated by rapidly scanning a laser beam to trap and independently manipulate small numbers of objects [118, 4]. However, these methods were restricted by the refresh times of the individual traps (if this becomes too long, either thermal, or other, convective perturbation of the object allows it to escape). Diffractive optical elements (DOEs), such as holograms, overcome these problems as they allow a single laser beam to be reshaped into an array of multiple beams, each of which gives an independent, permanent trap.

6.2 Holographic optical tweezers

A fixed geometry of multiple optical traps can be produced using holographic or diffractive optics to transform a single laser beam into a corresponding array of beams. For example, preformed DOEs have been used to form large tweezing arrays in 2D containing upwards of 100 trapped objects [119]. The recent advent of spatial light modulators (SLMs) allows the generation of multiple traps that can be reconfigured to video, or higher, frame rates. The commercial availability of spatial light modulators means that the DOE is computer addressable such that, with suitable algorithms, each element of the tweezing array can be manipulated independently [120, 121, 122]. Where previous methods, such as the galvo or acousto-optic scanner, have been limited to 2 dimensions, a spatial light modulator can introduce focal power, which shifts the axial position of the trap away from the focal plane of the objective lens, allowing manipulation in 3D [123]. DOEs also offer several advantages in that they can act as a lens, beam splitter or a combination of both. They also allow several lenses to exist in the same area simultaneously. Since DOEs are effectively holographic optical components, the use of SLMs in this way is sometimes referred to as holographic optical tweezers (HOTs) [124].

6.2.1 What is a hologram?

The theory of holography was invented by Denis Gabor in 1947, although it was not until the invention of the laser in 1960 that the first hologram, of a toy train and a bird, were made in 1962 by Leith and Upatnieks [125, 126].

Holography is a method of recording and displaying a 3-dimensional image of a 3D object on a 2D, or flat, surface. Well known techniques such as

photography record a 2D intensity distribution of a 3D object on a flat, photosensitive surface. Because only the intensity distribution is recorded, any information on the phase relationships between the waves scattered off an object are lost. Holography is different in that both the phase and the amplitude of the scattered waves are recorded. Only a brief explanation will be given here, but full mathematical details of holography and wavefront reconstruction can be found in many texts e.g. [106, 127].

In traditional holography, the phase and amplitude of the scattered waves are recorded using a coherent light source, such as a laser, to create an "intensity hologram". This light source is split into a reference and an object wave as shown in Figure 6.1. The reference wave illuminates the photographic plate directly, while the light scattered off the 3D object forms the object wave. These two beams form an interference pattern, and it is this interference pattern that is recorded on the photographic plate. The use of a spatially and temporally coherent light source results in an interference pattern that is stable with time. Unlike photography, the interference pattern that is recorded does not resemble the 3D object in question and hence is in a coded form, see Figure 6.2.

One category of holography that is of particular interest, in the context of the remainder of this Chapter and Chapter 7, is Fourier holography. In this type of holography there is a Fourier relationship between the hologram and the reconstructed image. Within optical tweezers, the phase and intensity distribution (complex amplitude) at the hologram (displayed on the SLM) is the inverse Fourier transform of the spot pattern at the image (or sample) plane as is discussed later in the Gerchberg Saxton approach to computer generated holograms, Section 6.4.

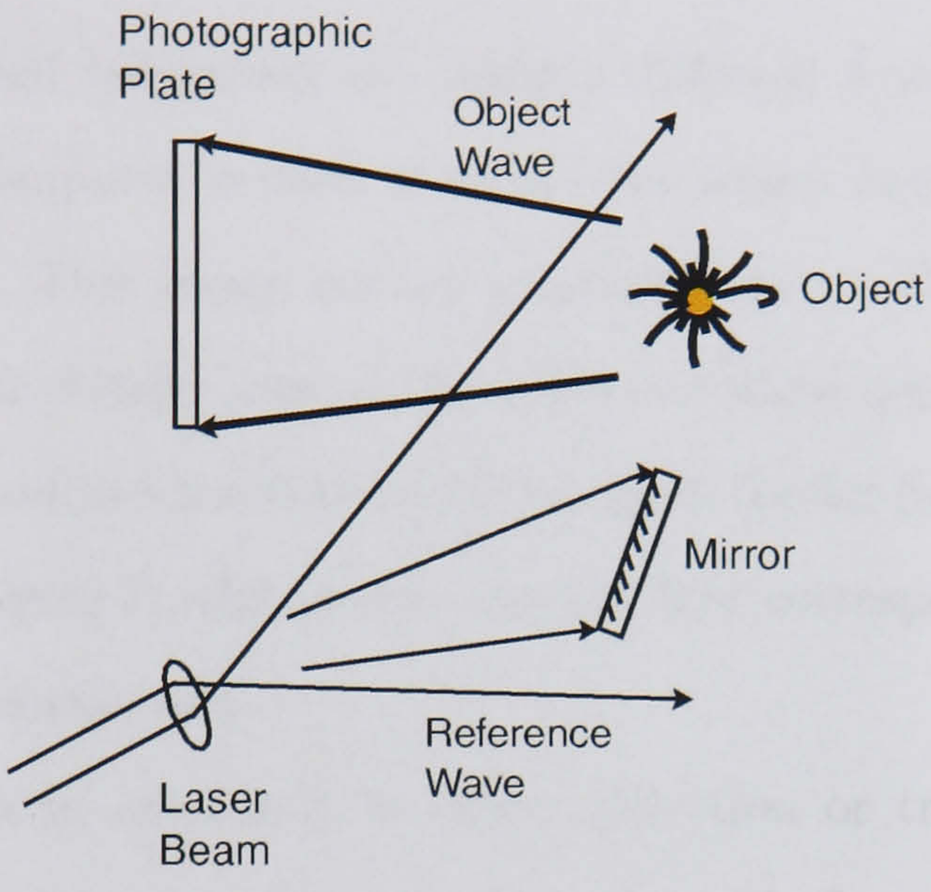

Figure 6.1: The photographic plate records the interference pattern produced by the light waves scattered off the object and a reference wave reflected off the mirror in order to produce a hologram as described in Section 6.2.1.

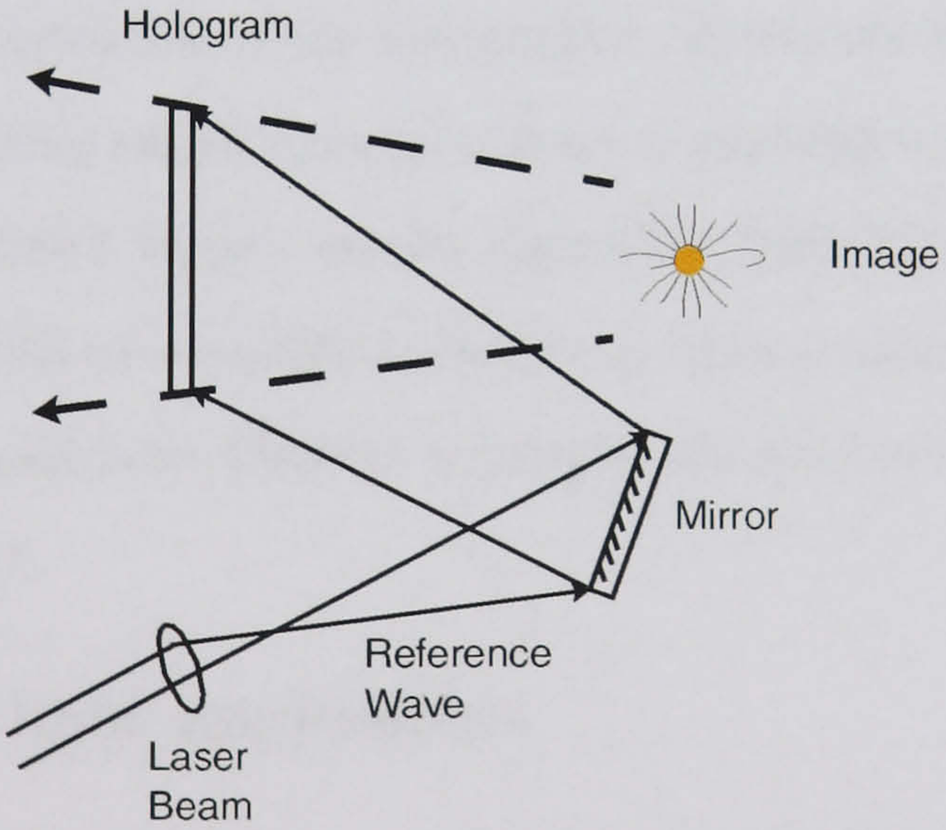

Figure 6.2: To reconstruct the hologram, a reference wave is used to illuminate the processed photographic plate. Light diffracted from the hologram makes it look as though it came from the original object, see Section 6.2.1.

6.2.2 Computer generated holograms

Computer generated holograms are slightly different from traditional holograms in that a computer is used to create the phase mask required to give the desired image. This image is then imprinted onto a 2D medium such as an SLM. The laser source acts as the reference wave recreating the object wave and hence produces the desired 3D image in the far field. In the context of the optical tweezers configuration, the far field corresponds to the image plane within the sample cell.

Holograms can be produced in either reflection or transmission mode. Reflection holograms reconstruct the desired profile from light reflected off the surface while transmission holograms reconstruct the desired profile once the light has passed through the hologram. The remainder of this Chapter is concerned with computer generated phase holograms used in reflection mode.

The algorithm used to calculate the desired pattern and transfer it to the SLM is key to the operation of the holographic optical tweezers. Holograms can be calculated using simple superpositions of gratings and lenses, or, for example, using a direct binary search algorithm [128, 129], a Gerchberg-Saxton algorithm [130] or a modified Gerchberg-Saxton algorithm [131, 123]. Each of these methods have different strengths and weaknesses as discussed in Sections 6.3 to 6.5.

6.2.3 Spatial light modulators

The holograms used here are required to enable the trapping of micron-sized objects. For this reason the holograms are phase modulated, and not amplitude modulated, so that there is no power loss. A phase-hologram can be thought of as a "phase mask" for the laser beam. This masks modifies the

phase of the input beam in order to create the multiple output beams. Holograms can be addressed to a spatial light modulator (SLM) which converts a computer intensity hologram into a phase hologram. Refer to Figure 6.3 for a picture of the Hamamatsu PAL SLM X7665 unit.

Figure 6.3: The Hamamatsu PAL SLM X7665 used in holographic optical tweezers as described in Section 6.2.2.

The SLMs achieve a spatially dependent phase delay by varying the optical path length through the liquid-crystal material [132] by applying a voltage across it. The resultant adjacent wavefronts then either constructively or destructively interfere producing the far-field pattern of choice. For more information on nematic liquid crystals as spatial light modulators refer to Khoo *et al.* [133] and Rakher *et al.* [134].

There are further considerations to take into account within holographic optical tweezers. Typically, for the holograms used in Chapters 6.6.3 and 7, the SLM is divided into 256 $\times$ 256 logical pixels even though the front end of the SLM is not actually pixellated. Additionally, every output beam is focused through a high numerical aperture microscope objective to a diffraction-limited spot corresponding to the trapping position. See Figure 6.4. When using a hologram to change the profile of the single mode, the size of the incident laser beam was expanded to about 1 cm in diameter to

fill the active area of the SLM. The SLM and the laser beam were aligned so that the centre of the expanded laser beam coincides with the centre of the hologram pattern.

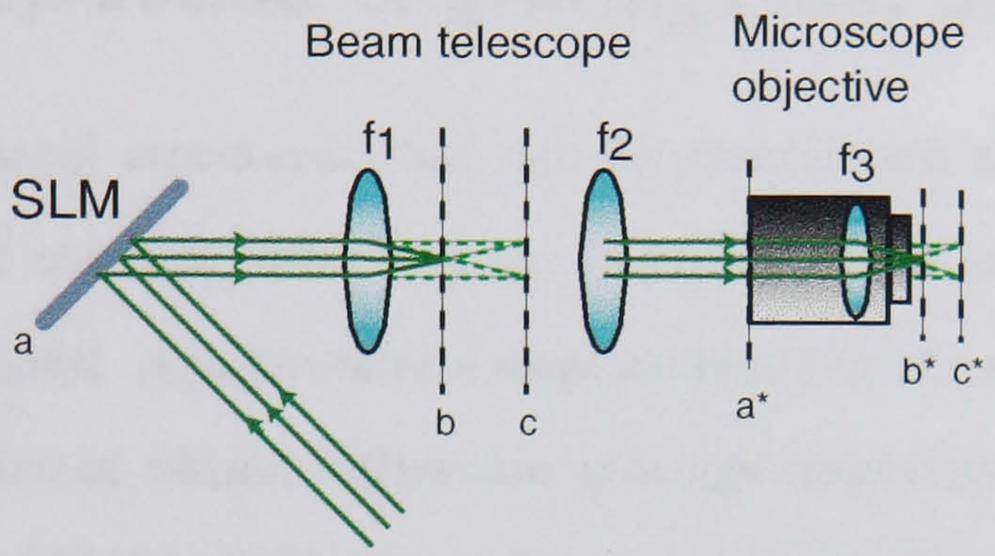

Figure 6.4: The focusing of the incident laser beam into separate beams using the SLM. The plane of the SLM, a, is imaged onto the back of the objective lens plane a^*, while the planes containing the 3D foci, b and c, are imaged into different planes in the focal region of the microscope, b^* and c^*. Section 6.2.2 describes this in more detail.

When choosing an SLM for use within optical tweezers it is important to choose an SLM that is optimised for use at the wavelength of the trapping laser. A high diffraction efficiency (greater than 40%) is desired to divert as much power into the first diffraction order as possible. An update rate of 25 frames per second will be sufficient to allow the optical tweezers traps to be manipulated in real time.

Various algorithms exist for the design of DOEs for the generation of arbitrary beams [135, 136]. However, several factors can affect the optimal use of HOTs. Firstly, the number of traps available is limited by the power of the incident laser beam (each trap requires a few mW of power and typical losses within the optical system amount to 50%). Secondly, the field of view is limited by the CCD camera, to 50 μm $\times$ 50 μm in our case. Lastly, the decrease in trapping efficiency, as the trapping beam is moved further away

from the zero order, can be attributed to using the objective lens away from its design conjugates and to the resolution of the SLM [137].

6.3 Superposition of gratings and lenses

The simplest crystal structures that can be created are the ones that are symmetric about the zero order and use holograms that are superpositions of gratings and lenses. Axial or lateral displacements can be achieved by using Fresnel zone plates or blazed diffraction gratings respectively. The concept is to add up the different fields from the respective gratings or Fresnel zone plates, ignoring the intensity whilst keeping the phase distribution.

By reflecting the expanded laser beam off a diffraction grating, the incident beam is split into a series of diffracted orders. The zeroth order corresponds to the original beam and the other orders are labelled outwards from this central position as ±1,±2,±3... etc. To put equal amounts of power into both the first and minus-first order, a square wave (binary grating), blazed from 0 to π over a distance $x = \Lambda$, where Λ is the period of the grating, would be used, as illustrated in Figure 6.5.

"Blazing" of these holograms, i.e. by applying a mapping function, for a specific wavelength allows the user to put more power into a preferential order. For example, the pattern of the grating can be designed so that it is the first-order diffraction that contains the beam or beams of interest. This is done by blazing the hologram using a wedge from 0 to 2π over a distance $x = \Lambda$, also illustrated in Figure 6.5.

For movement in both the x and y planes, a blazed diffraction grating produces the desired effect, whilst movement in the z direction is achieved through changing the focal length of a Fresnel lens. Reflecting the expanded

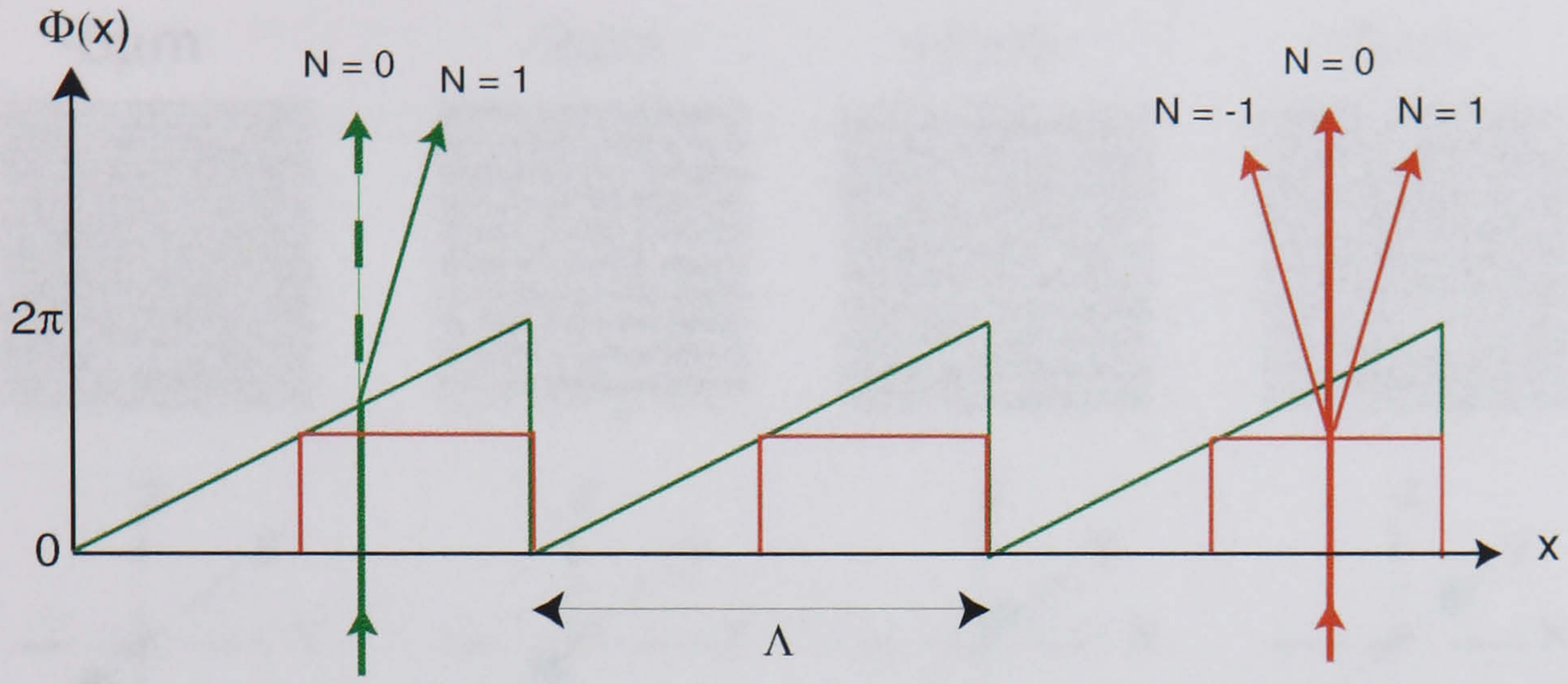

Figure 6.5: Blazing the power of the laser into different orders. The green laser beam is blazed from 0 to 2π once over a distance $x = \Lambda$ and results in the majority of the beam being diffracted into the first order. The red beam is a binary grating and shows that equal amounts of power are diffracted into both the first and minus first orders. See Section 6.2.2 for more details.

laser off a "blazed" Fresnel zone plate makes it possible to move the focus of the laser beam above or below the natural focal point of the objective lens by changing the focal length of the Fresnel lens. Figure 6.6 illustrates such blazed holograms that produce displacements of ± 2 and ± 5 μm's in each of the x, y and z directions.

These simple binary gratings can be used to produce traps at the corners of a square centered around the zero order by combining two binary gratings at 90° to each other. However, the use of such holograms is restricted to symmetric patterns making it unsuitable for creating arbitrary structures. For more complex patterns a hologram written using either a Gerchberg Saxton algorithm, see Section 6.4, or a direct binary search algorithm, see Section 6.5, is required.

Limitations in the spatial resolution and phase response of the grating result in some of the light being diffracted into other orders, producing extra

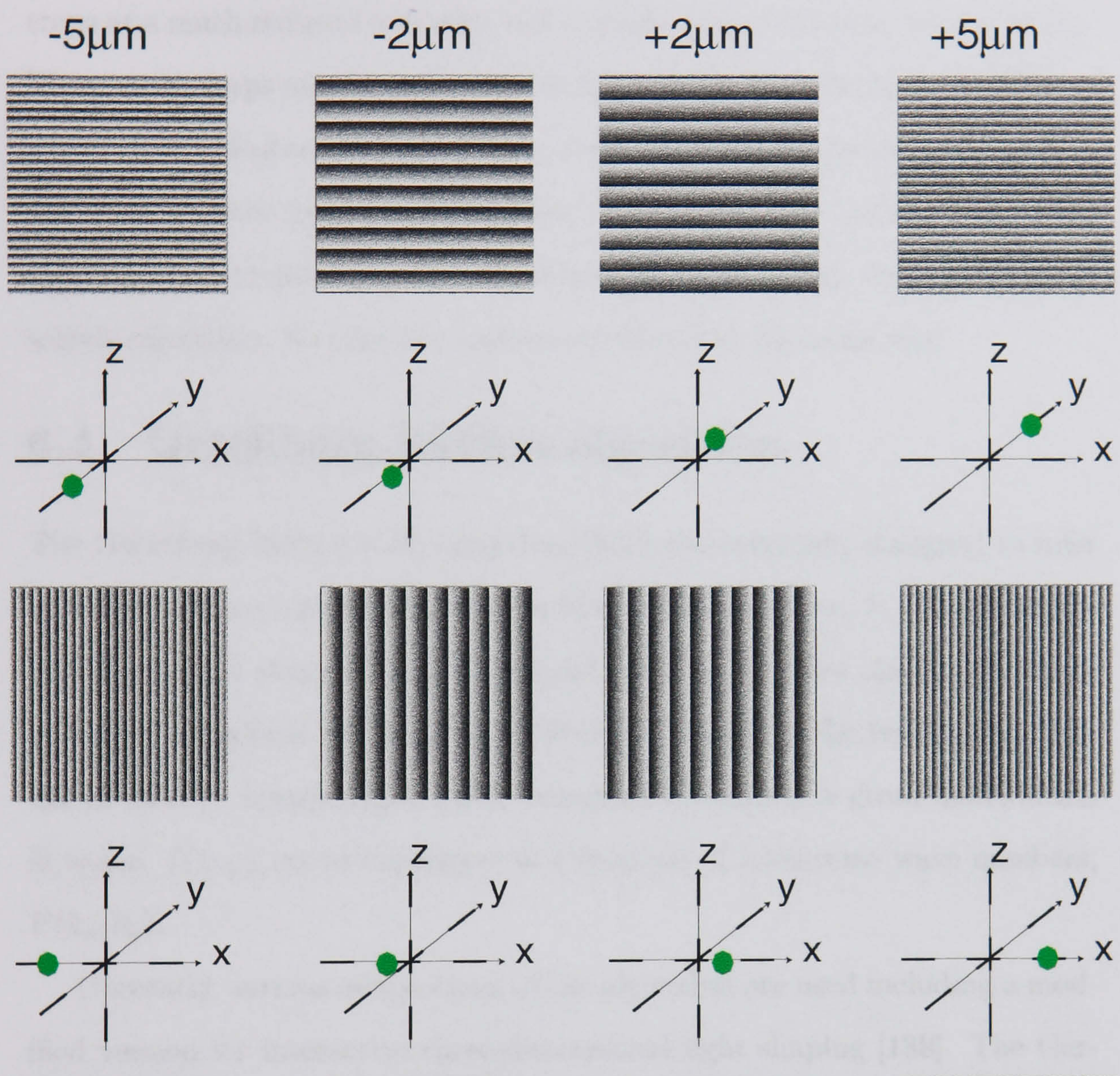

Figure 6.6: The effect of different types of holograms on an incident laser beam. The blazed diffraction grating can move a trap to any position on the x or y axis, the Fresnel lens moves traps up and down in the z direction. Refer to Section 6.2.2 for more information.

traps at a much reduced intensity, and a single trap at the zero order position. These extra traps may be removed through the use of a spatial filter or beam stop, or the hologram design can be modified to displace the desired intensity distribution away from the zero order of the laser beam. Similar limitations exist for the Gerchberg Saxton algorithm, Section 6.4, and the direct binary search algorithm, Section 6.5, and are overcome in the same way.

6.4 Gerchberg Saxton algorithm

The Gerchberg Saxton (GS) algorithm [130] was originally designed to infer an electron beam's phase distribution in a transverse plane, P, from intensity distributions in plane P and in a second plane Q. It relies upon there being a Fourier transform relationship between the waves in the two planes. The use of Fourier transforms (within holography) enables a given distribution in space, $f(x, y)$, to be expressed as a function of transverse wave numbers, $F(k_x, k_y)$.

Currently, various adaptations of the algorithm are used including a modified version for interactive three-dimensional light shaping [138]. The Gerchberg Saxton algorithm is an iterative Fourier-transform algorithm where the pattern in the plane of the focussed microscope objective is the Fourier-transform of the pattern imprinted to the laser beam at the SLM.

By applying the Gerchberg Saxton algorithm to light, it is possible to calculate a phase distribution $\Phi_P(x, y)$, at plane P, that turns the intensity distribution $I_P(x, y)$ into a desired intensity distribution $I_Q(x, y)$ at plane Q.

Figure 6.7 shows a flow diagram of the Gerchberg Saxton algorithm for light distributions in two dimensions.

In the case of holographic optical tweezers, the laser initially has an intensity distribution of I_P and a flat phase relationship at the diffraction (SLM) plane. The phase and intensity of the beam at the image (sample) plane I_Q can be found by taking the Fourier transform of the complex amplitude (phase and intensity) of the beam at the diffraction plane, as illustrated in Figure 6.7.

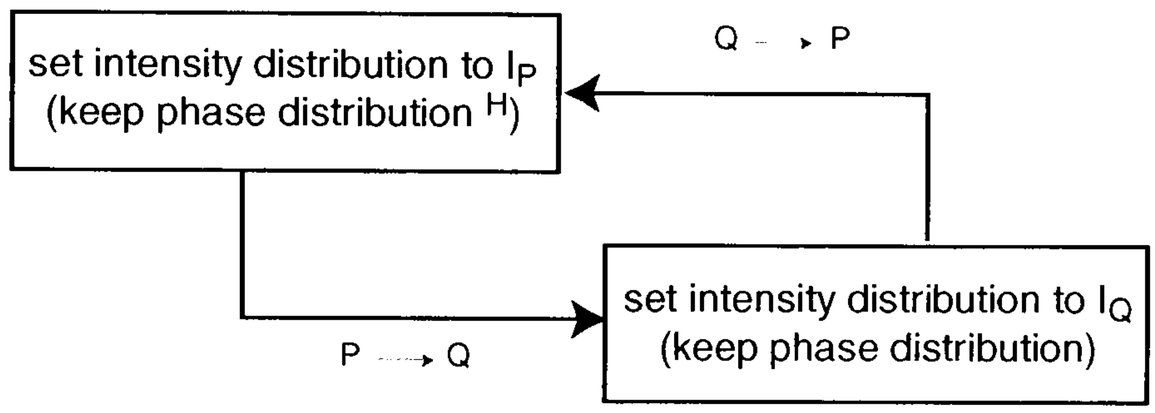

Figure 6.7: Flow chart for the GS algorithm for intensity shaping in one plane. The arrows marked P → Q and Q → P indicate the mathematical operations that transform the amplitude profile in plane P to that in plane Q and vice versa. These are the Fourier and inverse Fourier transforms. The phase distribution marked ^{H} converges to the phase hologram. See Section 6.4 for more details.

However, the intensity distribution I_Q in the image plane is often not the desired one, so it is "replaced" with the desired one whilst keeping the phase relationship. Now, if the inverse Fourier transform is taken, the new complex amplitude at the diffraction plane can be calculated. Once again, the intensity distribution at the diffraction plane may not be correct and so must be replaced with I_P (since optimization is for phase only, all intensities in the hologram plane must be set to the intensity of the incident laser beam, which is usually a Gaussian or uniform distribution) whilst maintaining the phase distribution. This process is repeated until the process converges, usually within a few iterations. The resulting phase distribution at the diffraction

plane imparted to the laser beam usually produces a good approximation of the desired intensity output I_Q in the image plane.

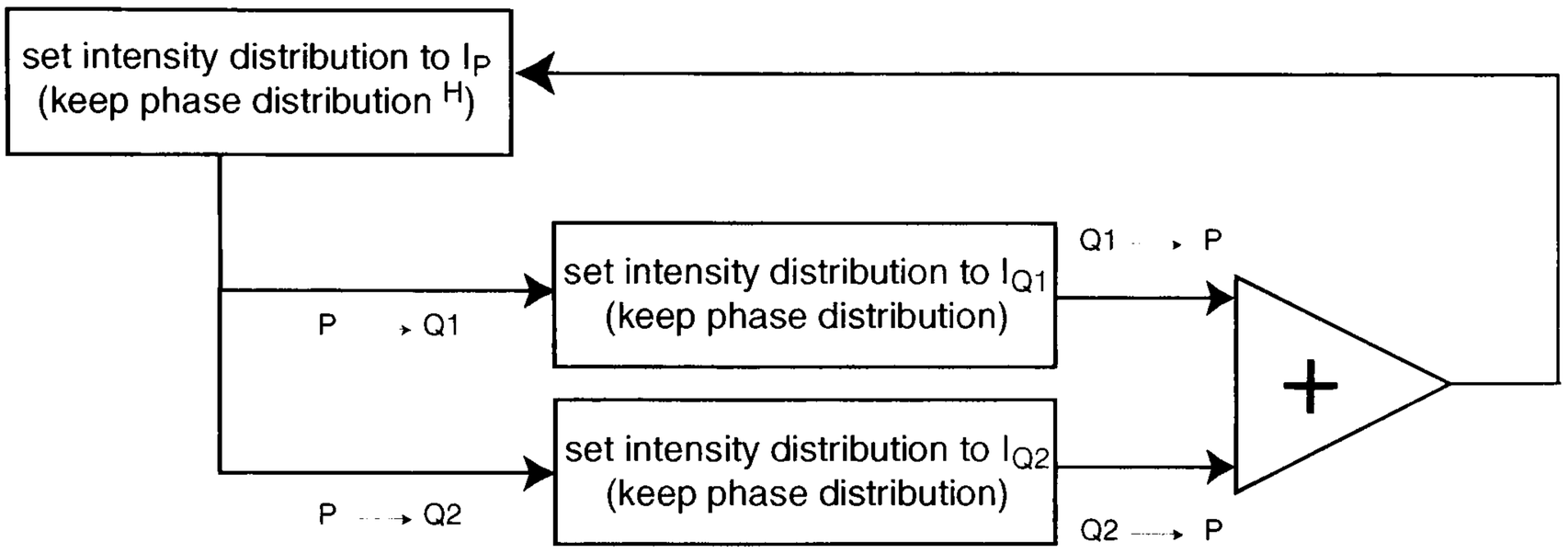

Figure 6.8: Flow chart for the GS algorithm for intensity shaping in multiple planes. The arrows marked $P \rightarrow Q1$, $P \rightarrow Q2$, $Q1 \rightarrow P$ and $Q2 \rightarrow P$ indicate the mathematical operations that transform the amplitude profile in plane P to that in plane Q and vice versa respectively. The phase distribution marked ^{H} converges to the phase hologram. See Section 6.4.

Section 6.6.3 deals with the manipulation of particles in 3 dimensions within optical tweezers. The 2D Gerchberg Saxton algorithm mentioned above can easily be extended to the generation of bright spots (optical traps) in more than one plane, see Figure 6.8. To extend the Gerchberg Saxton to 3D, the light has to be propagated not just into the far field and back again, but into any arbitrary plane [139]. The complex amplitudes in planes Q_1 and Q_2 are assessed by taking the Fourier transform of the phase and intensity distribution of the diffraction plane. For each image plane, the intensity distributions are replaced with the desired values whilst maintaining the phase relationships. These complex amplitudes are then summed before beam propagation backwards and the intensity distribution back at the diffraction plane replaced with the correct value, again keeping the phase relationship.

The Gerchberg Saxton algorithm is also referred to as an error reduction algorithm as the error between the desired and actual intensities must decrease or remain constant after every iteration [130]. It is also not restricted to creating symmetric patterns.

To use the modified Gerchberg Saxton algorithm interactively, Dr Johannes Courtial developed a computer program that ran continuously through the loop shown in Figure 6.8, allowing the intensity distributions at arbitrary positions in three dimensions to be controlled. Each individual intensity maximum corresponds to an optical trap, the position of which can be moved independently in real time. Using a 2.9 GHz dual processor computer, typical holographic patterns represented by a 256×256 array can be calculated in about 0.5s, which is fast enough for interactive use.

6.5 Direct binary search algorithm

The direct binary search (DBS) algorithm [128, 129] is another method used for hologram design. In this case, the hologram's performance on producing focussed beams at arbitrary positions in multiple planes defines a figure of merit. Random changes at random positions are made to the hologram design and if the change results in an improvement to the figure of merit, the change is kept, otherwise it is discarded.

In this particular DBS algorithm, the hologram is divided into "N" pixels. Ideally, the aim is to produce a "phase mask" where only the phase of each pixel in the array is manipulated. To begin with, each pixel is assigned a random phase. The target intensities, I_{Tk} ($k = 1, 2, ..., M$ where M is the number of target positions), are calculated using the initial intensity of the input beam and the phases associated with each pixel. An error function ε,

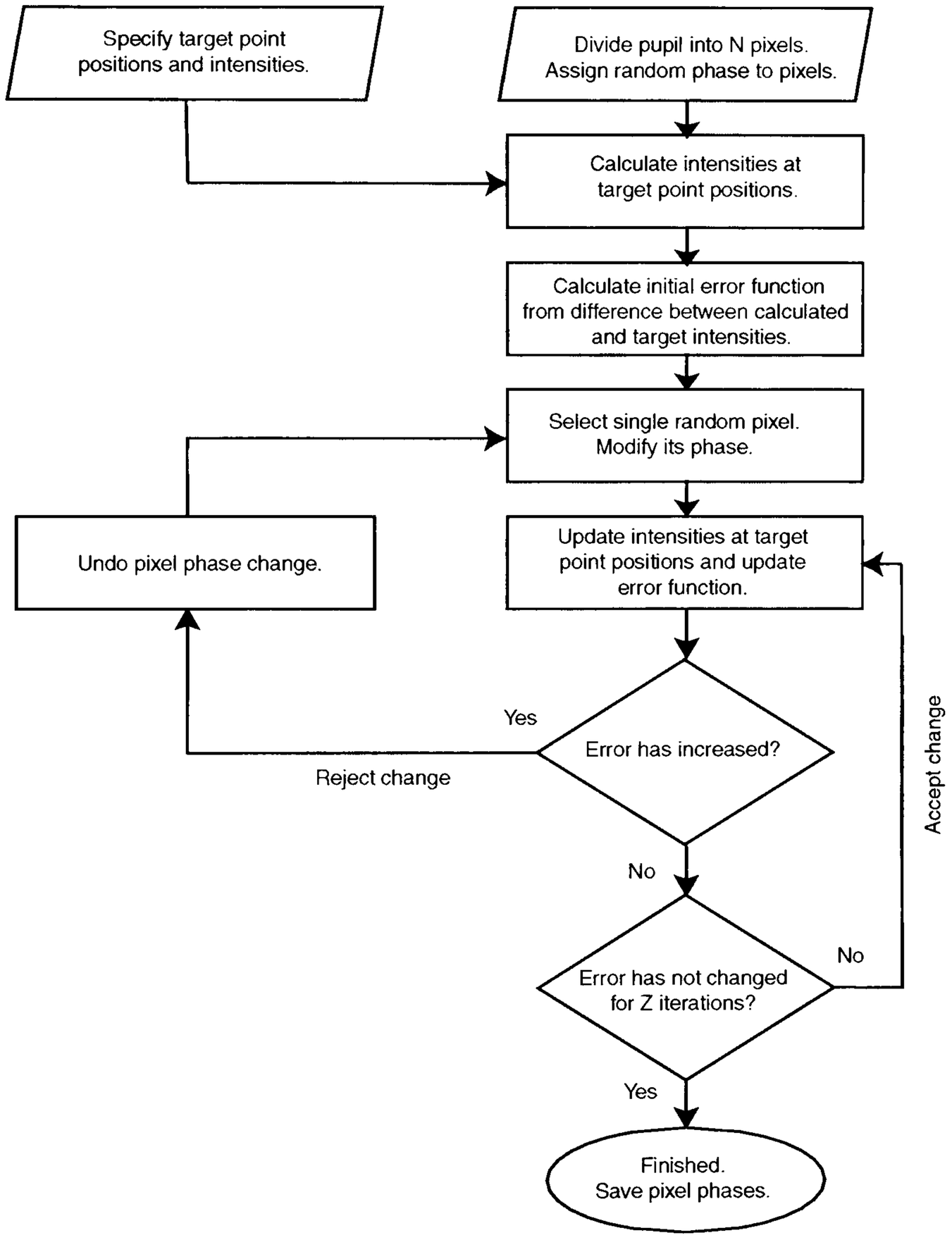

Figure 6.9: Flow chart for the direct binary search optimization. The magnitude of the pixel transmittances is fixed at unity and only the pixel phases are manipulated. See Section 6.5 for full details.

as a figure of merit, is then calculated from the desired target intensities, I_{Tk}, and the generated intensities, I_k, for example, in the form [129]

$$\varepsilon = \sum_{i=1}^{M} (I_{Tk} - I_k)^2 \tag{6.1}$$

where M is the number of target positions.

A more complex version of this error function exists where different target points can be weighted in order to emphasize specific regions, see [129].

A pixel is selected at random and its phase is adjusted to test all the discrete values possible. The error function is evaluated and if there is an improvement in the error the change is kept, otherwise it is discarded. This process is repeated until ε becomes smaller than a predetermined value or does not change for a predefined number of iterations. Repeated iterations of this process gradually lead to an optimized hologram design.

A major problem of producing 3D structures in the optical tweezers arises when two traps have the same lateral displacement but are displaced axially. In these cases it is probable that the trapped beads will fall into one trap, which could be a limiting factor on the structures that could be formed. One solution is to ensure that there is a region of zero intensity between two adjacent traps in the same lateral plane. This can be performed using annular beams for simple algorithms, which produce an unchanged trap close to the beam focus, but have an on-axis intensity that falls to zero away from the trapping plane. In the case of the random binary search algorithm, the zero intensity requirements can be incorporated into the figure of merit.

This method of hologram production is slow and therefore cannot be used interactively in the same manner as the Gerchberg Saxton algorithms. However, its use is not restricted to symmetric patterns with the user being

able to define intensity peaks and intensity nulls. It is worth emphasising that this gives enhanced trap performance as it is possible to produce intensity minima between two optical traps vertically displaced from one another which helps prevent stacking of objects in the vertical direction.

The random binary search algorithms were written by Dr John Laczik, from the University of Oxford.

6.6 3D manipulation of microparticles

Prior to this work, the holographic optical tweezers were characterised [137], and the maximum lateral displacement of the 1st order was shown to be of the order of 40 microns. This was limited by the spatial resolution of the spatial light modulator. Additionally, the axial displacement, which was limited by using the objective lens away from its design conjugates, was of the order 60 μm. Increasing the laser power into each trap would increase the relative strength of the optical trap, but the magnitude of Q depends on factors such as the degree of focussing and any abberations. The SLM can be used to compensate for spherical abberations in the objective lens, producing optimum trap strengths for specific trapping distances into the sample and may allow larger structures to be created.

Micro-crystal structures were created within the optimum trapping volume using holographic optical tweezers to position and hold objects in three dimensions. The spatial light modulator (SLM) was used to produce multiple optical traps, corresponding to the positions of lattice sites in crystal structures. These structures, which vary from simple cubic to diamond, were then manipulated or scaled about arbitrary axes.

The background experimental work for this section of work was carried out with Jonathan Leach and Gavin Sinclair both from the University of Glasgow although the results presented here, with the exception of Figure 6.14, are unique to this thesis. Dr Johannes Courtial from the University of Glasgow wrote the Gerchberg Saxton algorithms and Dr John Laczik from the University of Oxford wrote the Direct Binary Search algorithms used in these experiments.

6.6.1 Experimental setup and materials

The apparatus illustrated in Figure 6.10 was adapted for the real time manipulation of 3D structures. The trapping laser was a frequency doubled, commercial Nd:YVO_4 laser (100 mW, 532 nm). The laser was coupled into the microscope with a dichroic mirror positioned between the object and tube lens, giving approximately 30 mW of power into the trapping plane. The sample cell was mounted on a piezoelectric (PZT) stage, which allowed 100 microns of travel in 3-dimensions and could be controlled either manually or from a voltage source. The output beam from the laser was collimated to 10 mm diameter and projected at near normal incidence on an optically-addressed spatial light modulator, operated in reflection mode. The SLM used was a PAL-SLM X7665 purchased from Hamamatsu. It is an optically addressed, nematic liquid crystal with VGA (640 $\times$ 480 pixels) resolution, 40% diffraction efficiency and a near video update rate of 25 frames per second. An afocal telescope images the plane of the SLM to the plane of the main beam steering mirror of the tweezers, which is itself re-imaged, via a dichroic mirror, to the rear aperture of the objective lens with a magnification of 0.22 so that the aperture of the SLM slightly overfills the back aperture

of the objective lens. The beam steering mirrors allowed the trap positions to be moved into the centre of the visual field. The intermediate focus of the afocal telescope allowed any unwanted diffraction orders from the SLM to be removed using a spatial filter. The basic apparatus setup is shown in Figure 6.10.

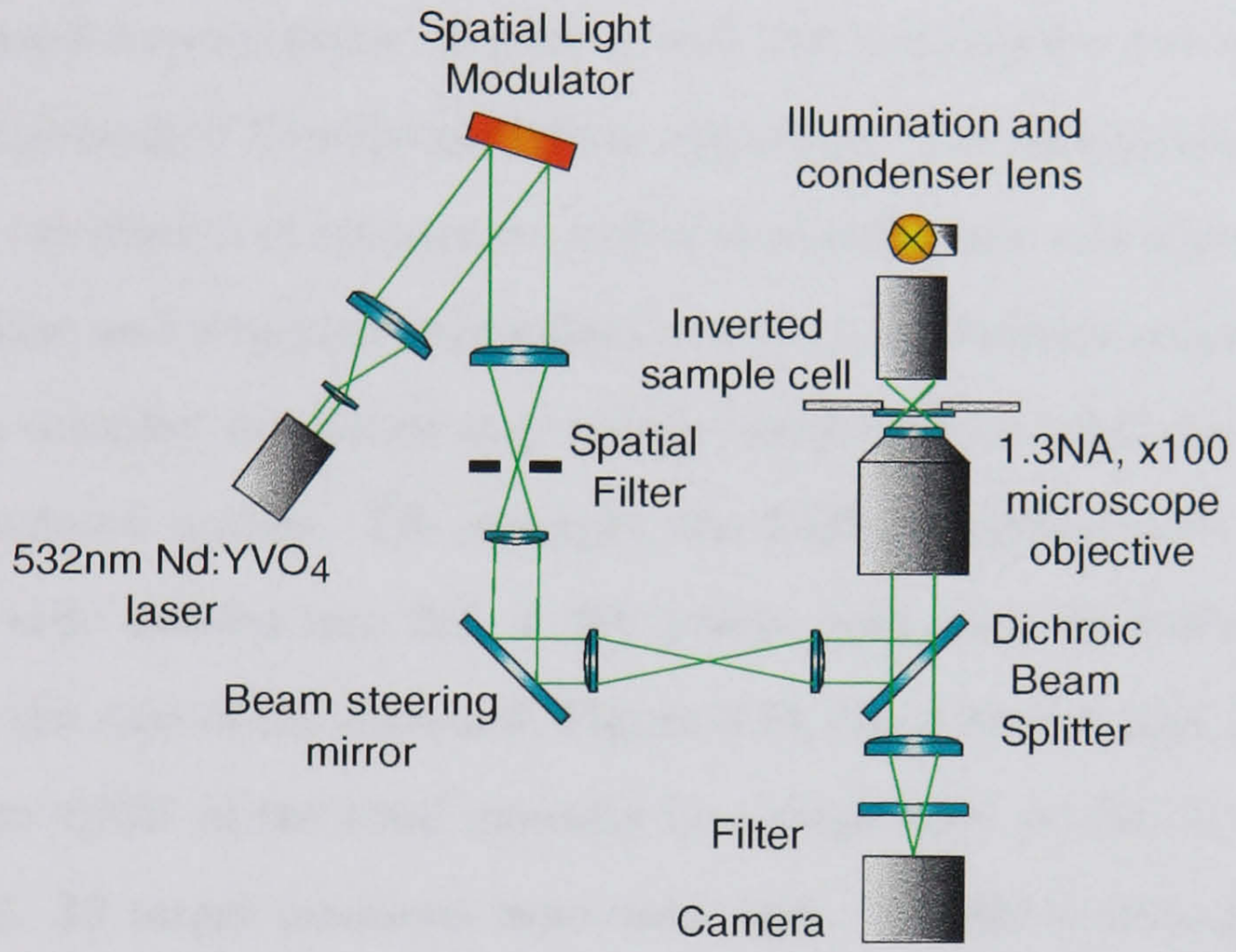

Figure 6.10: This figure shows the basic experimental apparatus setup for the holographic optical tweezers as described in Section 6.6.1.

Figure 6.4 shows how different planes from the SLM are focussed to different points in the sample cell. For the more complex structures, such as the diamond structure, the 100 mW laser was replaced by a 1.5W laser ("Excel", Photonics Solutions, Germany). This higher power laser enabled more power to be directed into each trap.

2 μm diameter silica spheres were purchased from "Bangs Laboratories".

6.6.2 Methods

3D micro-crystal structures were created using holographic optical tweezers. By applying the appropriate method of hologram creation, it was possible to form multiple beam foci to construct several unit cell structures. Different approaches towards generation of the holograms were adopted ranging from a simple superposition of grating and lens components through to the widely implemented Gerchberg Saxton algorithm. The simple approach enables the calculation of symmetric crystal structures that can adjust the lattice constant and structure orientation in real time, whereas non-symmetric and more complex structures may require more sophisticated algorithms of a pre-calculated nature. For example, the DBS holograms used in Chapter 6.6.3 were divided into 256 × 256 pixels, each with 16 different phase levels. In the case of the diamond, Figure 6.14, the desired target intensities were set to 4.75% of the total intensity in a single spot produced by a clear lens pupil. 18 target positions were used, and 250,000 iterations were required to calculate the pattern using a standard single CPU 2.9 GHz PC in approximately 20s. Thus, these crystal structures could be scaled or rotated about arbitrary axes, as shown here, or could be made permanent by gelling them into position as demonstrated in Chapter 7.

6.6.3 Results and discussion

The simplest 3D structure created was a body centered cubic crystal, see Figure 6.11. Here, 2 μm silica spheres form the lattice points of the cube which has a unit length of 10 μm. The top 4 beads of the cube were manipulated independently of both the central bead and the bottom four beads. By changing the hologram it was possible to move the upper four beads from 4

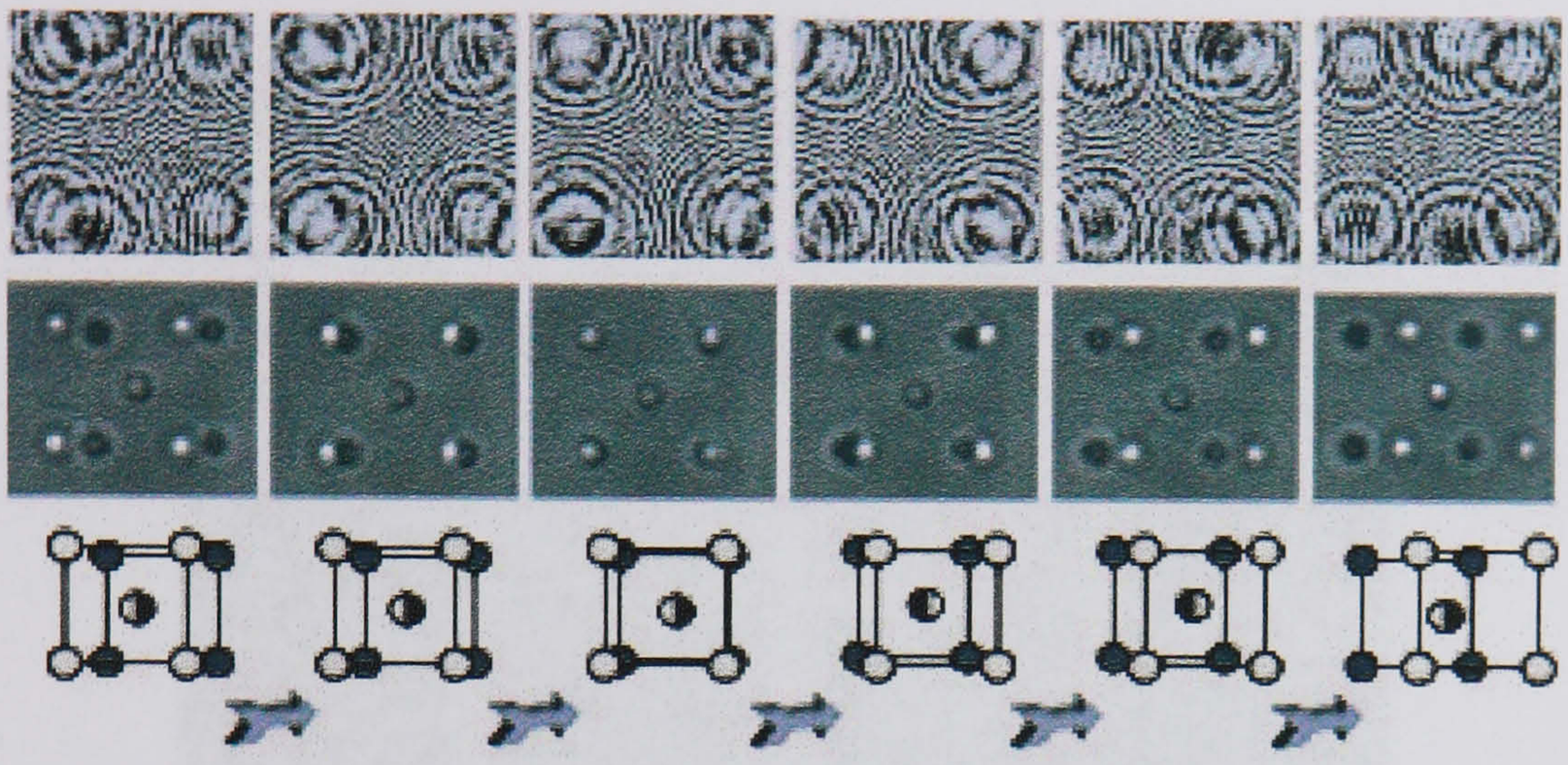

Figure 6.11: A body centred cubic structure composed of 2 μm silica spheres, where the top four beads are moved independently of the rest of the structure. Here the top layer is moved from being left of centre, to directly above the bottom layer to being right of centre. The cube has a side length of 10 μm. The holograms were superpositions of grating and lens components. See Section 6.6.3.

μm left of centre, to above the bottom four beads to form the cubic structure, and finally right of centre by 4 μm in real time.

Figure 6.12 shows the real time manipulation of entire cubic structures using grating and Fresnel lens combinations. Figure 6.12 is a simple cubic structure, made with 2 μm silica spheres, that grows from a unit cell length of 3 μm to 8 μm. This technique can also be used to provide real time adjustment of the structure so that it can be oriented into any particular direction or continuously rotated about an arbitrary axis.

For the following, more complex structures, a more sophisticated hologram design was implemented. The random binary search approach, as discussed in Chapter 6.2.2, was employed to create a tetrahedral structure that was rotated head over heels, from a series of pre-determined holograms, as demonstrated in Figure 6.13. Here four 2 μm spheres separated by 5 μm in each direction defined the structure. Figure 6.14 illustrates 18 trapped silica

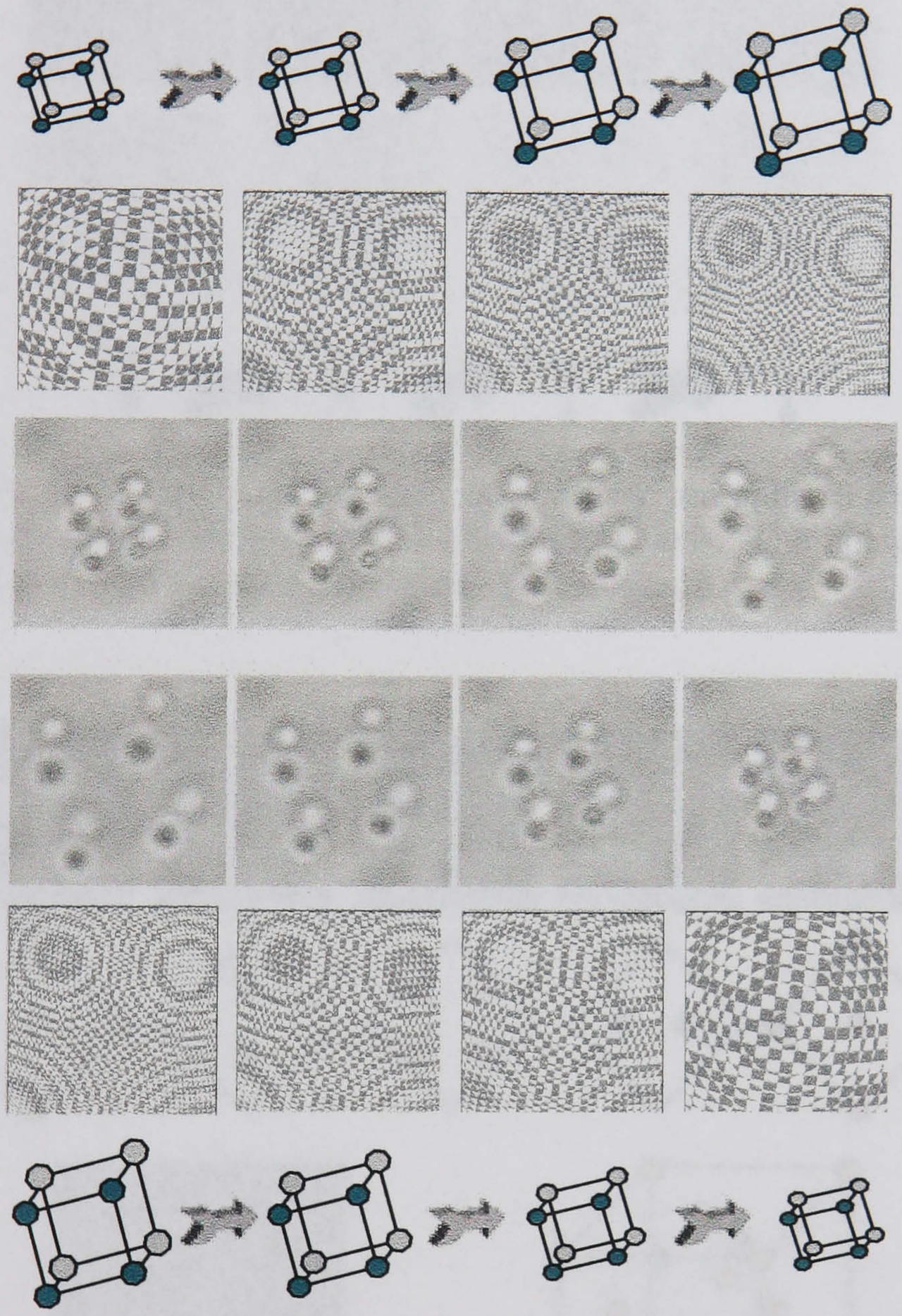

Figure 6.12: Demonstration of a 3D simple cube being expanded and contracted in real time. The holograms were superpositions of grating and lens components. The cube starts with a 3 μm side and grows to a 8 μm side, before deflating down to a cube with 3 μm unit length. Refer to Section 6.6.3 for further information.

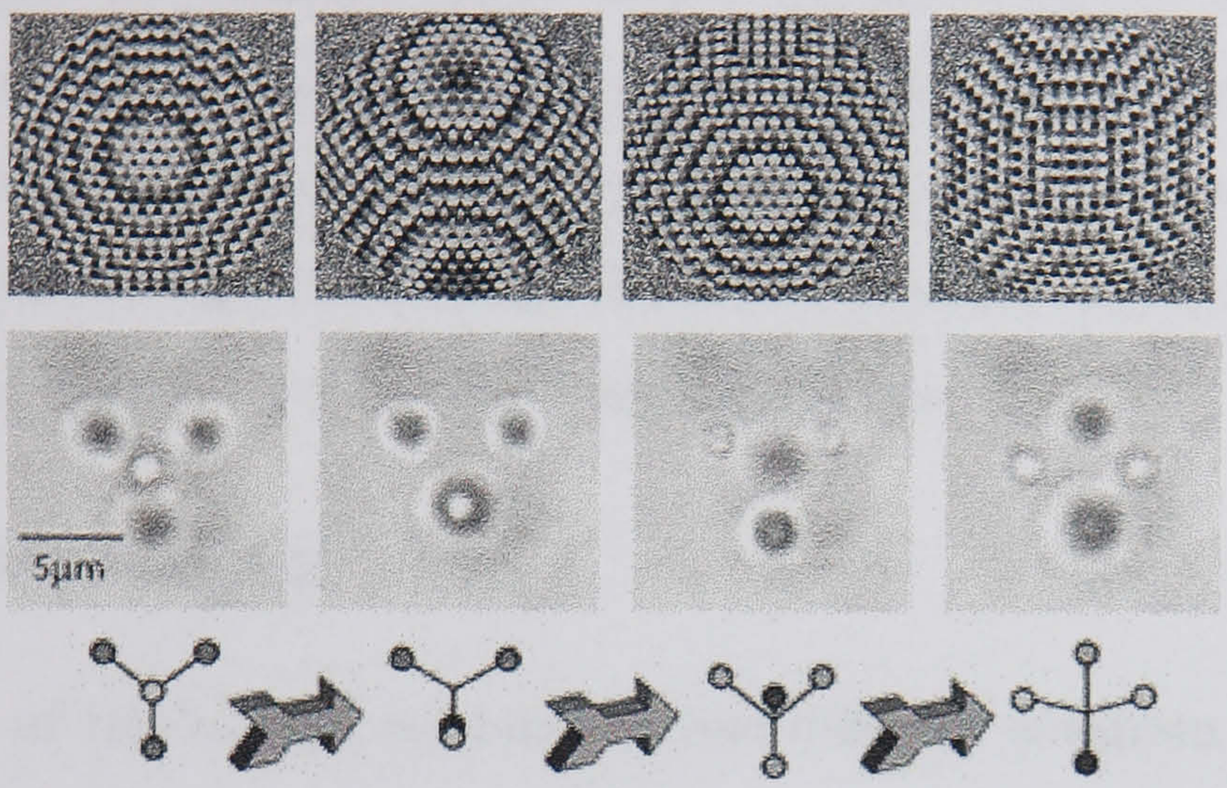

Figure 6.13: A 3D tetrahedron made from four 2 μm spheres separated by 5 μm in each directions and rotated about the x axis. The holograms were produced by a binary search algorithm. See Section 6.6.3.

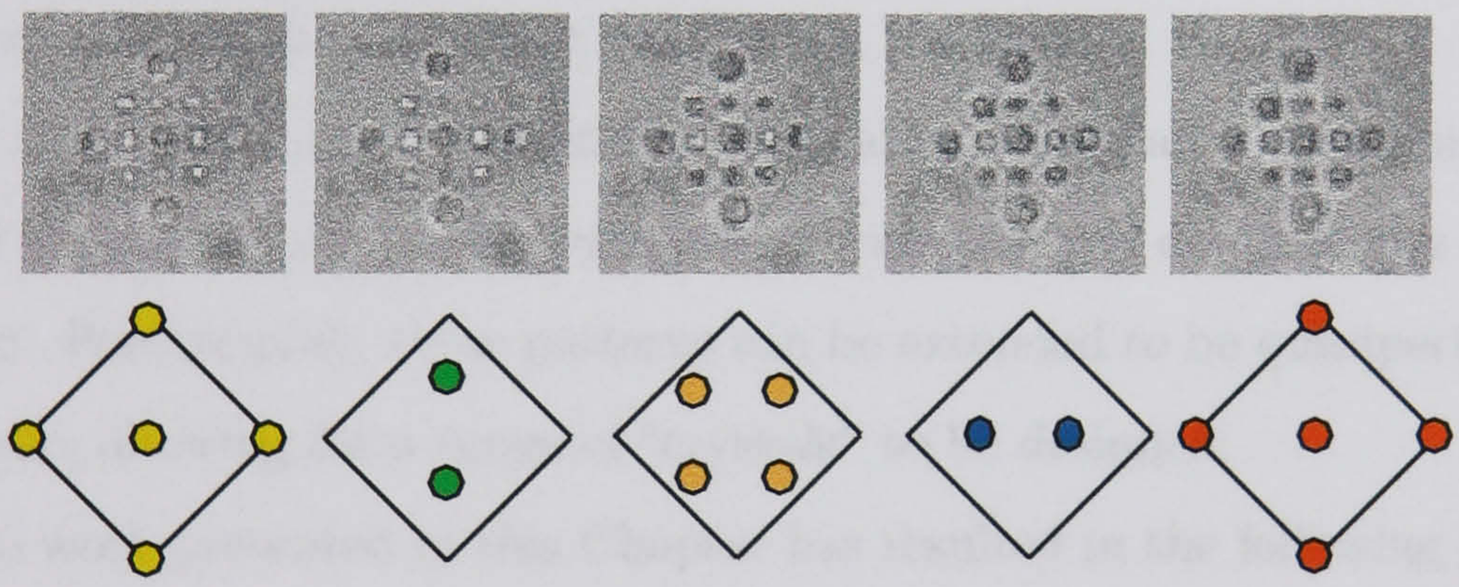

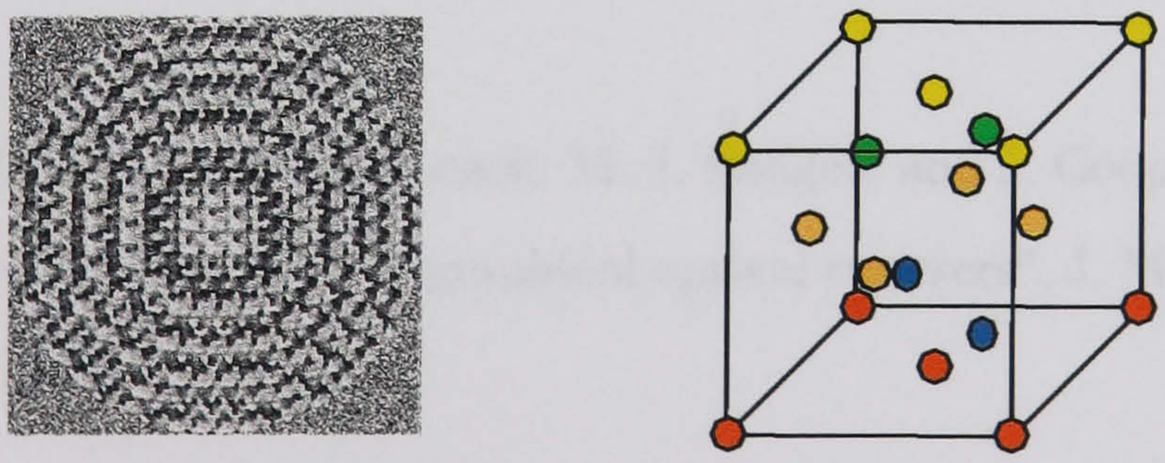

Figure 6.14: A diamond unit cell created by a binary search algorithm, written by Dr Z. L. Laczik from Oxford University, consisting of 18 silica spheres in 5 planes with a unit length of 12 μm. Each layer in the structure is separated by 3 μm as described in Section 6.6.3.

spheres to give the diamond lattice with a unit cell length of 15 μm. This image was not manipulated in real time, although the image sequence shows the complete structure being lifted so that each of the five planes comes into focus in sequence. The first and last layers have spheres trapped in the same lateral positions but are separated axially by 12 μm.

6.7 Conclusion

The advent of spatial light modulators, and different hologram algorithms, gives users the option to split a light beam into several light beams and manipulate them independently of each other in real time. This will not only enable current optical tweezers applications to be optimised, but will also offer exciting prospects for new technologies such as lab-on-a-chip, where micro-manipulation of multiple objects is a key issue.

By their very nature, holographic optical tweezers can be computer controlled in order to adjust the symmetry, periodicity and depth of any desired pattern. Furthermore, these patterns can be extended to be quasiperiodic or aperiodic, allowing for a range of "crystals" to be designed.

The work presented in this Chapter has resulted in the following journal publications:

- G. Sinclair, P. Jordan, J. Leach, M. J. Padgett and J. Cooper, "Defining the trapping limits of holographical optical tweezers", J. Mod. Opt. 51, 409-414 (2004).

- Jonathan Leach, Gavin Sinclair, Pamela Jordan, Johannes Courtial, Miles J. Padgett, Jon Cooper and Zsolt J. Laczik, "3D manipulation of particles into crystal structures using holographic optical tweezers", Opt. Express 12, 220-226 (2004).

- Gavin Sinclair, Jonathan Leach, Pamela Jordan, Graham Gibson, Eric Yao, Zsolt John Laczik, Miles J. Padgett and Johannes Courtial, "Interactive application in holographic optical tweezers of a multi-plane Gerchberg-Saxton algorithm for three-dimensional light shaping", Opt. Express 12, 1665-1670 (2004).

- Gavin Sinclair, Pamela Jordan, Johannes Courtial, Miles Padgett, Jon Cooper and Zsolt John Laczik, "Assembly of 3-dimensional structures using programmable holographic optical tweezers", Opt. Express, 12, 22, 5475-5480 (2004).

Chapter 7

Permanent 3D micro-structures created using holographic optical tweezers

It is possible to create permanent 3D structures by manipulating micron-sized particles, or cells, contained within a solution comprising monomer precursors using an optical tweezers, and setting them in a matrix by the initiation of the polymerisation process. These structures remain intact for many days after the laser beam has been removed, making it easy to transfer the sample to another location and image it ex-situ using confocal or multi-photon imaging.

7.1 Introduction

As discussed in Chapter 6, holograms in the form of SLMs are now available that can be updated at video frame rates allowing the trap positions to be modified in real-time. The flexibility of holographic optical tweezers enables any structural arrangement to be produced.

Previously, the structural integrity of an array of manipulated objects relied on the continued presence of the laser beams. Such an arrangement

may therefore be inconvenient for a variety of reasons, including local heating of the environment which may modify or perturb biological structures (such as cell or molecular arrangements) and the need to remove the sample and either image or modify it ex-situ (away from the trap).

This Chapter investigates the permanent 2D and 3D setting of microstructures within a gelatin matrix. Objects trapped and set include silica spheres, fluorescent spheres and *E. coli*. Once set within the polymer matrix, the fluorescent spheres were imaged, ex-situ, under a confocal microscope. The same was done for *E. coli* tagged with a fluorescent marker. Finally, the bacterially viability of the *E. coli* within the gelatin matrix was studied.

Prior to this work, a scanning optical tweezers has been used to trap multiple objects in a 2D geometry within a monomer-containing solvent. Subsequent photopolymerisation locked the objects in place [140]. Furthermore, optical tweezers using a method to create large two-dimensional patterns with a view to locally directing three-dimensional epitaxial growth has been demonstrated [141].

7.2 Experimental setup and materials

7.2.1 Optical tweezers setup

The experimental setup used here was the same as the configuration described in Chapter 6.6.1, and was based around an inverted microscope with a x100 oil immersion objective lens with a trapping laser and a spatial light modulator. Details for the apparatus used for each experiment is given in Sections 7.3.1 – 7.3.5.

7.2.2 Confocal and multi-photon imaging

Confocal imaging relies on a point illumination source being imaged onto the sample. The reflected, or scattered, light is re-imaged onto an adjustable pinhole as illustrated in Figure 7.1. Typically, this is achieved through the use of a focused laser beam. Only light from the sample plane is imaged whilst light from other planes is not. By using this method much of the out-of-focus light is eliminated.

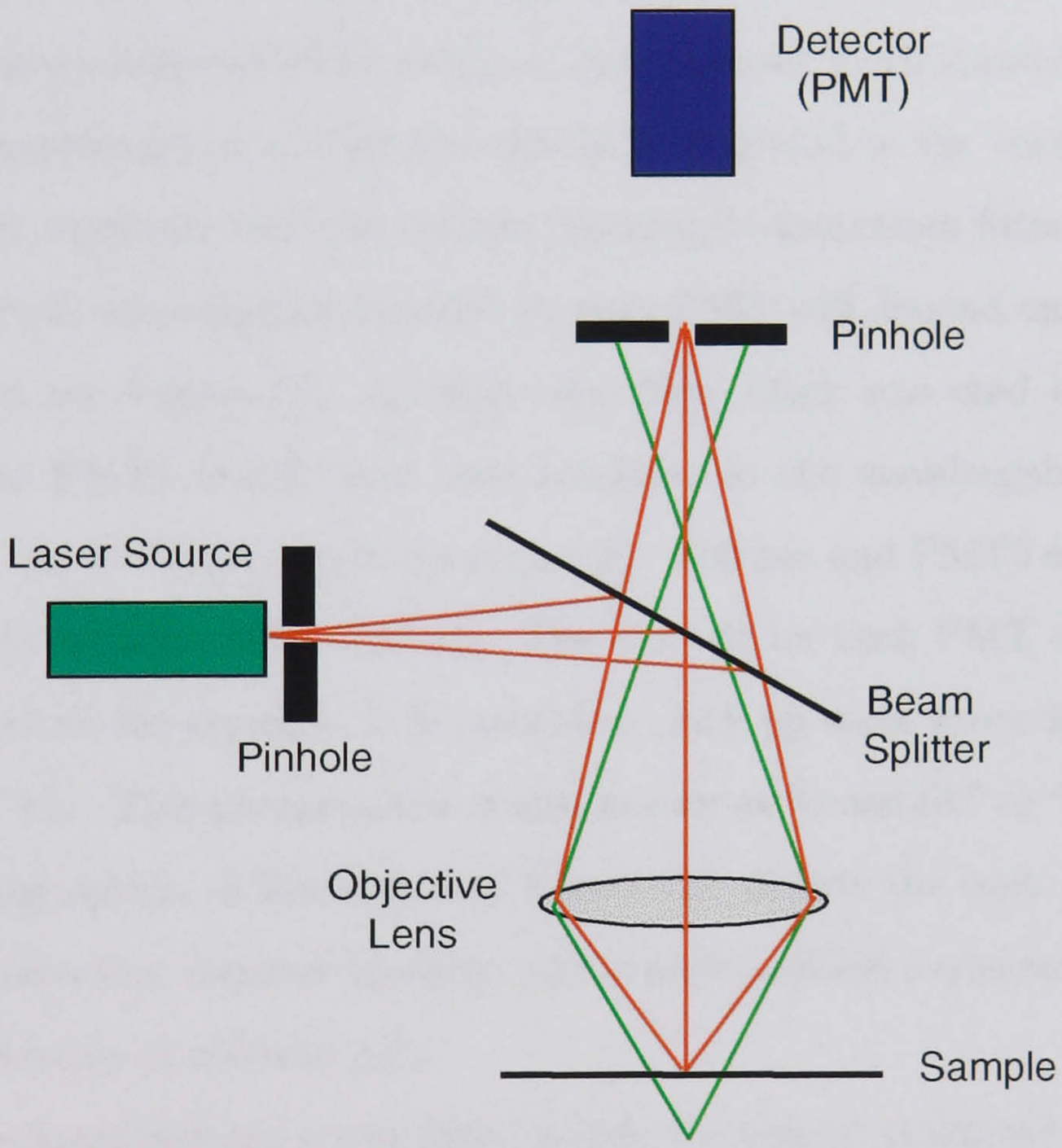

Figure 7.1: Illustration of how a pinhole confocal microscope works. Only light from the sample plane is imaged, much of the out-of-focus light is eliminated. See Section 7.2.2 for details.

Photon multiplier tubes (PMTs) or charge coupled detectors(CCDs) can be used to measure the intensity of an emitted signal by counting the incoming photons and amplifying the signal if the sample is fluorescent or contains a fluorescent dye. Filters can also be inserted into the beam, prior to the light entering the detector, to filter out the excitation light and let through only the emitted fluorescent light. As a result, no Rayleigh scattered light is incident on the PMTs. The particular setup used here comprises three wavelengths (647, 488 or 568 nm) of a Krypton/Argon laser, with each wavelength reflected onto a different PMT using dichroic mirrors. Each scan lets through only one wavelength at a time and this light is guided to the corresponding PMT tube, equipped with the correct blocking/transmittion filter.

The actual wavelengths detected by each PMT will depend on the set of filters used, see Figure 7.2. A triple cube filter block was used here which means that PMT1 would have been sensitive to the wavelengths between 350 – 520 nm, PMT2 sensitive between 520 – 600 nm and PMT3 sensitive to wavelengths between 600 – 700 nm. The cut offs for each PMT will not be well defined so, for example, it is possible to pick up some green light in the blue PMT etc. This phenomenon is also known as "crosstalk" or "bleeding".

Scanning optics, as illustrated in Figure 7.2, directs the laser beam over the whole area that requires imaging, and at each position a computer records the the intensity of emitted light.

The confocal imaging setup (Strathclyde University, Glasgow) was based around an MRC-1024ES which houses the PMTs and scanning optics. The microscope used was a Nikon eclipse E600FN microscope with a Nikon CFI60, Plan Fluor x100, 1.3NA series oil immersion lens. See Figure 7.3.

Multi-photon imaging can also be performed using the same equipment but using a different laser. Multi-photon imaging uses a laser that, in general,

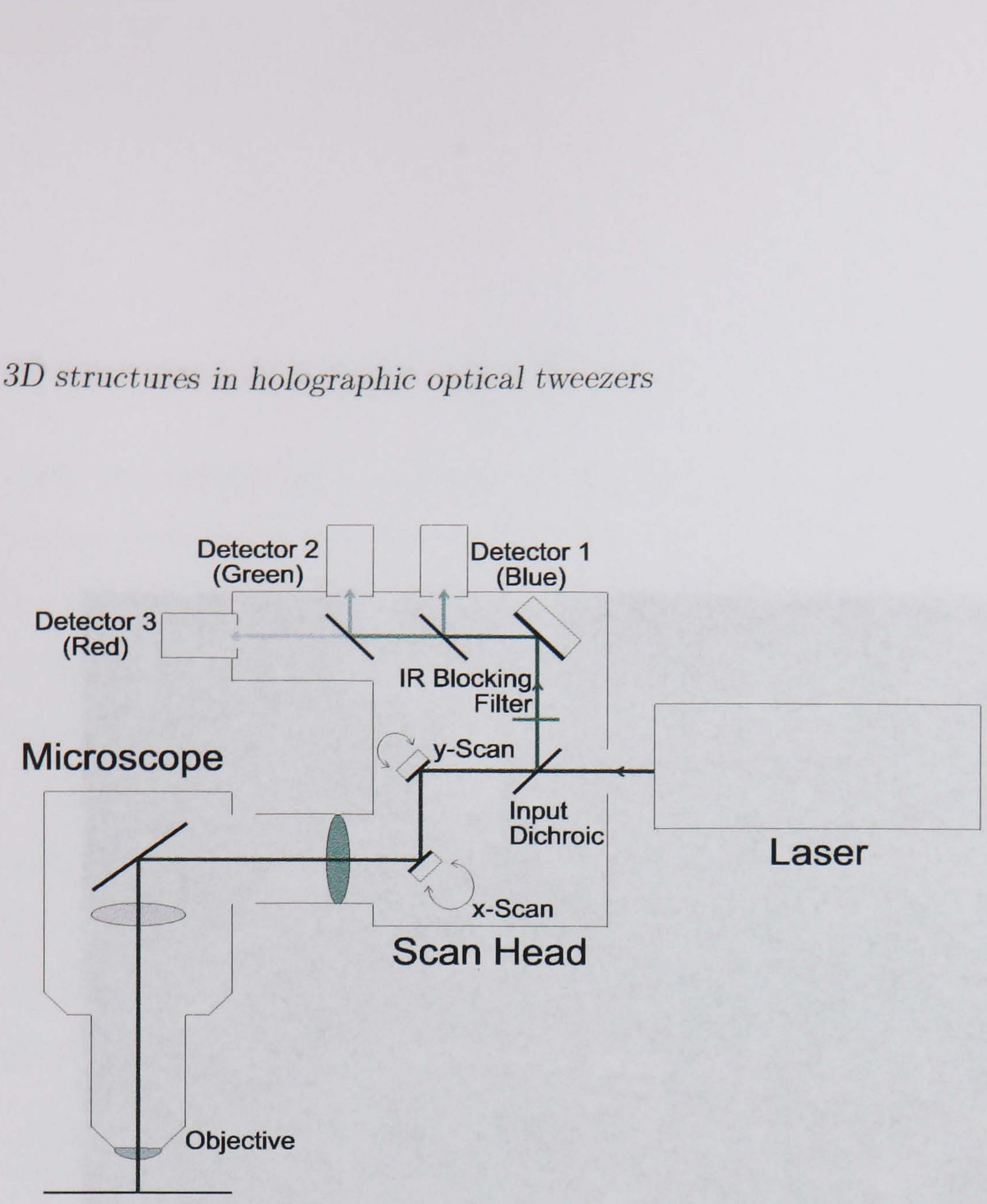

Figure 7.2: Schematic diagram of the confocal microscope with scanning optics used for confocal and multi-photon imaging as described in Section 7.2.2.

emits at a longer wavelength than those used for confocal imaging and is pulsed in the MHz region. This type of imaging relies on there being two-photon excitation at the focal point of the laser. As the probability of two-photon excitation scales with the second power of intensity, it follows that the most probable location for excitation, and hence imaging, occurs at the focal point of the incident laser beam. This results in only a very small volume being excited and the pinhole required for confocal imaging is no longer necessary.

The multi-photon imaging was performed using a femto-second pulsed Coherent Mira 900 Ti-Sapphire laser tunable between 700 – 900 nm. The system was pumped by a Coherent Verdi, Vanadate crystal and the wavelength tuning was achieved by adjusting a birefringent prism in the optical

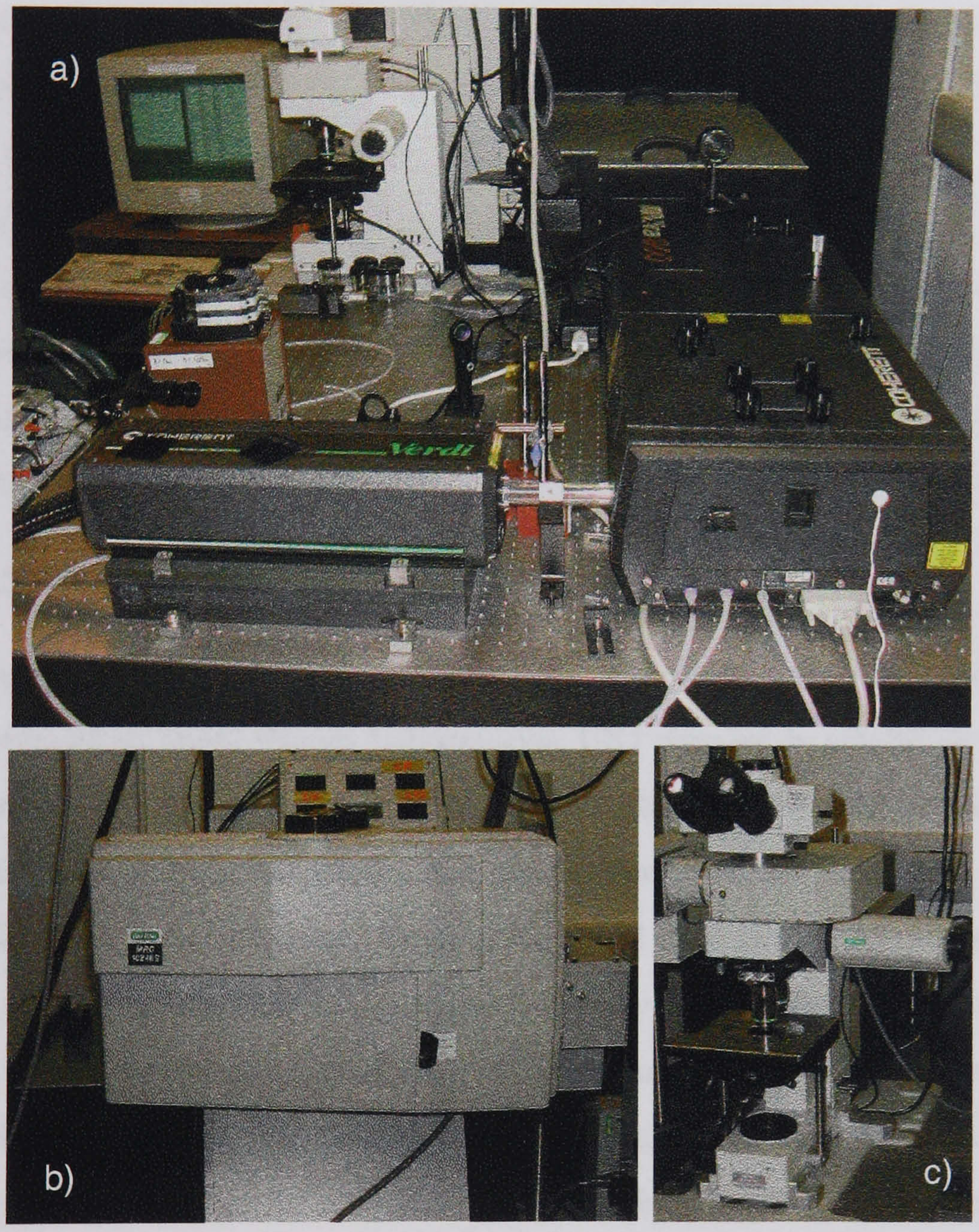

Figure 7.3: Confocal and multi-photon imaging setup. Figure (a) shows the housing of the Coherent Mira 900 laser and the Krypton/Argon laser, (b) shows MRC-1024ES that houses the PMT's and scanning optics and (c) is the Nikon microscope. Refer to Section 7.2.2.

path. The multi-photon imaging was performed using a 780 nm wavelength. The acquisition software was LaserSharp 2000, Version 5.2 build 823 and the images were analysed using PicViewer v2.4 with samples being viewed through a x100 oil immersion objective lens. For a detailed discussion on confocal microscopy see reference [142].

All the confocal imaging was performed in collaboration with Dr John Girkin and Dr Amanda Wright at the Photonics Department at the University of Strathclyde, Glasgow. The only exception to this was the bacterial viability experiment, where the samples were imaged at Göteborg University, Sweden in collaboration with Prof Dag Hanstorp and Dr Mattias Goksör.

7.2.3 Materials

A number of different particles have been set in this experiment. 2 μm diameter silica beads (Bangs Laboratories, UK) were set in gelatin, as were 1.8 μm diameter polystyrene fluorescent beads (Sigma, UK, product number L-0905) which absorb at 470 nm and are fluorescent at 505 nm.

HB101 *E. coli* (PRomega, Product No L1011) and HB101 *E. coli* tagged with a fluorescent marker were also used. In order to make the *E. coli* fluorescent, it had to be tagged, or labelled, with a primary and secondary marker. A primary antibody was bought from Virostat, (*E. coli*, all antigens rabbit, unconjugated, product number 1001) to which a secondary fluorescent antibody could be attached. The secondary antibody used was a labelled goat anti-rabbit IgG antibody, with fluorescent dye conjugate Alexa Fluor 532, (Molecular Probes, UK, product number A-11009). This particular dye absorbs at 531 nm and emits at 554 nm. Nutrient broth, LB (Luria bertani) broth, TBS (Tris buffered saline, made from 20 mM Tris pH 7.4 and 150 mM

NaCl) and PBS (Phosphate buffered saline, made from 20 mM sodium phosphate pH 7.4 and 150 mM NaCl) buffers were also used in the preparation of the samples (Sigma, UK).

The *E. coli* samples were prepared by Dr Paul Blackburn from the Chemistry Department, University of Glasgow.

For the bacterial viability experiment, a different strain of *E. coli* was used. MC4100 *E. coli* stock (in house, Chalmers University, Gothenburg, Sweden) was added to LB nutrient broth (Merck, Germany) for preparation of the *E. coli* samples. The MC4100 strain was chosen as it lacks the flagella that enables most *E. coli* to move around, and so is ideal for long time studies. Propidium iodide (Molecular Probes, UK) was used to stain the *E. coli*. Propidium iodide is a nucleic acid stain. Its absorption maximum is 535 nm and its fluorescent maximum is 617 nm.

The gelatin used for all experiments was "Pig skin" gelatin and was a gift from Unilever, Netherlands. The only exception to this was the bacterial viability experiment, Section 7.4.5, where the gelatin used for setting the bacteria was "Favrit Gelation", bought in Sweden.

7.3 Methods

7.3.1 Permanent setting of silica microparticles

Holograms consisting of simple superpositions of different gratings and lenses were imaged onto a PAL-SLM X7665 (Hammamatsu Photonics) to create the desired pattern for the silica spheres to be trapped in. The SLM is an optically addressed, nematic liquid crystal with VGA (640 × 480 pixels) resolution, 40% diffraction efficiency and a near video update rate of 25 frames per second. In the two examples illustrated in Section 7.4.1, the

zero order was left in and used as part of the final structure. The tweezers system, as described in Section 7.2.1 using a 100 mW, 532 nm Nd:YVO_4 laser , was used to trap 2 μm diameter silica spheres suspended in a 3% wt liquid gelatin solution into the desired pattern. Again, a simple algorithm combining diffraction gratings and Fresnel lenses was used to form the desired trapping patterns. Once trapped, the spheres were left isolated for 4 hours with the laser switched on, giving 30 mW of power in the trapping plane distributed between all the traps, until the gelatin set. The exact gelation time was dependent on the concentration and the temperature of the solution.

7.3.2 Permanent setting of fluorescent microparticles

This experimental setup comprised a variable power, maximum ouput 1.5W, 532 nm Nd:YAG laser ("Excel", Photonics Solutions) and an LCR-2500 SLM (Holoeye Photonics). The Holoeye SLM is an electronically addressed nematic liquid crystal with 1024 $\times$ 768 pixel resolution and a maximum refresh rate of 75 frames per second. The diffraction efficiency in the first order is also in excess of 40%. 5 μl of 1.8 μm diameter polystyrene fluorescent beads (Sigma, product number L-0905) which absorb at 470 nm and are fluorescent at 505 nm, were suspended in a gelatin solution consisting of 0.4g gelatin mixed with 12 ml of water. The optical tweezers were then used to trap the spheres in the desired 2D or 3D pattern. Again, a simple algorithm combining diffraction gratings and Fresnel lenses was used to form the desired trapping patterns with the zero order forming part of the structure. Once trapped, the spheres were left isolated for a few hours with the laser switched on until the gelatin set. Typically, 75-100 mW of power in the trapping plane was used to trap the configurations. Once the micro-structure had set, the

laser was switched off and the structure was protected from evaporation by adhering a cover slip onto the top of the sample cell in order to seal it.

Once the sample was set and sealed, it was imaged ex-situ using confocal microscopy.

7.3.3 Permanent setting of unlabelled *E. coli*

The experimental setup comprised a 1064 nm variable power, maximum power 3W, laser (Quantum Venus) and an X8267 SLM (Hammamatsu Photonics). An infrared laser was employed as it does not cause as much damage to biological objects as a green (532 nm) laser does. This is because biological objects are not as absorptive to IR wavelengths.

HB101 *E. coli* growth steps were performed at 37°C, 200 rpm. One colony of *E. coli* strain HB101 was selected from an LB plate and grown overnight in 5 ml LB. 200 ml of this overnight culture was then used to inoculate 20 ml LB and this culture was grown to exponential (log) phase[1].

1 ml samples of *E. coli* (HB101), that was cultured overnight, were placed into cuvette's and spun down at 200 rpm to form pellets. Each pellet was then re-suspended in 1 ml of TPS buffer, and a subsequent 1/10 dilution made.

0.3g gelatin was added to 15 ml water before mixing 10 μl of the 1/10 diluted *E. coli* with 400 μl of the gelatin mixture. 200 μl of the resulting mixture was placed into the sample cell of the optical tweezers.

[1]Log phase is when the bacteria are multiplying optimally, and there will be very few dead cells. It is measured using optical density at 600 nm (OD600). Stationary phase occurs when the culture either runs out of nutrients or struggles in its toxic excretions and death phase is when the bacteria are dead. The timescales vary according to the culture conditions but typically it takes around 4 hours to get to log phase (with above dilutions from a fresh plate), log phase lasts perhaps 2 hours as does stationary and death phase. In log phase *E. coli* can double every 15-20 minutes (growth is exponential 1 becomes 2 then they become 4 then they become 8 etc...)

A modified Gerchberg-Saxton algorithm was used in order to create a hologram to produce a body centered rectangular structure in the far field.

The bacteria were trapped at the centre and corners of the cuboid using 130 mW at the trapping plane. The sample took 3 hours to gel due to higher than average temperatures in the lab.

7.3.4 Permanent setting of labelled *E. coli*

HB101 *E. coli* was cultured overnight using the method described in Section 7.3.3. 4 × 100 μl samples were taken from the culture and placed into aliquots and centrifuged (200 rpm) for 5 minutes to form concentrated *E. coli* pellets. One of these pellets was taken and excess liquid removed. The pellet was then suspended in 1 ml of PBS buffer (PBS buffer consists of 20 ml sodium phosphate and 150 ml sodium chloride). A subsequent 1/10 dilution was made. This was then centrifuged again, and resuspended in 1 ml of PBS buffer. 10 μl of the primary antibody was added and the sample left for 10 minutes, to allow the anti-body to react with the *E. coli*, and then centrifuged. Again, excess liquid was removed and the resulting pellet resuspended in 1 ml of PBS. 10 μl of the secondary antibody was then added and left for 10 minutes before being centrifuged. The final pellet was suspended in 10 μl of PBS ready for use in the optical tweezers.

3 μl of this resulting tagged *E. coli* solution was added to 400 μl of 0.3g gelatin and 15 ml water solution. This sample was placed in the optical tweezers.

A modified Gerchberg-Saxton algorithm was used in order to create the hologram of the desired structure and this was optically addressed to the SLM, which in this case was the "No. 5" shape found on a dice.

The laser used was a 1064 nm variable power, maximum output 3W (Quantum Venus) in conjunction with an X8267 SLM (Hammamatsu Photonics). The optical tweezers traps were loaded with *E. coli* using a 198 mW at the trapping plane. Once all the traps were filled, the power was reduced to 175 mW and left for 10 minutes before further reducing the power down to 105 mW. The laser beam was left on for 1 hour at this power until the gelatin set.

Once the gelatin had set, the sample was sealed with a cover slip and then imaged using a confocal microscope.

7.3.5 Bacterial viability in gelatin solution

50 μl of MC4100 *E. coli* stock (in house, Chalmers University, Gothenburg, Sweden) was added to 30 ml of LB nutrient broth (Merck, Germany) and incubated in a glass beaker at 37°C for 12 hours. 1 ml of this cultured *E. coli* sample was added to 30 ml of fresh LB nutrient broth for experimental use.

0.6g of gelatin (Gelatin "Favrit Gelation", Sweden) was added to 10 ml RO water at 80°C and kept warm until the gelatin dissolved. 75 μl of the 0.6g gelatin solution was mixed with 75 μl of the *E. coli* and nutrient broth solution in a 1.5 ml aliquot, resulting in a 3% wt/v mixture. 1 ml of the resulting gelatin and *E. coli* mixture was added to 1.5 μl propidium iodide (Molecular Probes) and incubated in darkness for 10 mins. Sample cells consisted of 120 μm deep spacers (Molecular Probes) on glass microscope slides. 8.5 μl of gelatin, *E. coli*, nutrient broth and propidium iodide mixture was placed onto the glass slide in the spacer and a cover slip sealed the chamber.

For studying the bacterial viability of the *E. coli* in gelatin, two samples of 1.5% wt/v, 3% wt/v and 5% wt/v were prepared using *E. coli* from the stationary growth phase [6]. To investigate the effect of using *E. coli* in its exponential growth phase, two further samples using 3% wt/v gelatin and *E. coli* mixture were prepared.

The stained *E. coli* samples were imaged using a confocal microscope. The 488 nm line of an Ar+ laser was used to excite the propidium iodide dye used to stain the *E. coli*. It was possible to use the microscope with or without fluorescence.

7.4 Results and discussion

7.4.1 Permanent 3D structures

Images of the 2 μm silica spheres were taken once the gelatin had set and the trapping beam had been switched off. Figures 7.4 and 7.5 are examples of a series of images taken at different depths in two permanently set structures, illustrating the 3D nature of the geometrical arrangements.

Figure 7.4 consists of a set of 5 diagonal steps, each bead being separated from it's neighbour by 2 μm in the x direction, 1.5 μm in the y direction and 3.25 μm in the z direction. A picture of the hologram used to produce the image is also shown.

Figure 7.5 demonstrates the permanent setting of a pyramid structure along with the hologram used to create the structure. The structure itself comprises a base, made from four spheres set in a 3 μm $\times$ 3 μm square, with the apex of the pyramid positioned 4 μm above the centre of the square base. Both examples successfully demonstrate the ability to permanently set pre-defined 3-dimensional structures in a gelatin host.

Figure 7.4: Illustration of the 3-dimensional nature of the 5 steps, along with a picture of the hologram used to create the structure. Pictures 1 to 5 are images taken from the actual structure. Picture 1 is focussed on the bottom bead, picture 2 is focused on the second bead from the bottom, picture 3 is focussed on the middle bead, picture 4 is focussed on the second bead from the top and picture 5 is focussed on the top bead. See Section 7.4.1 for more information.

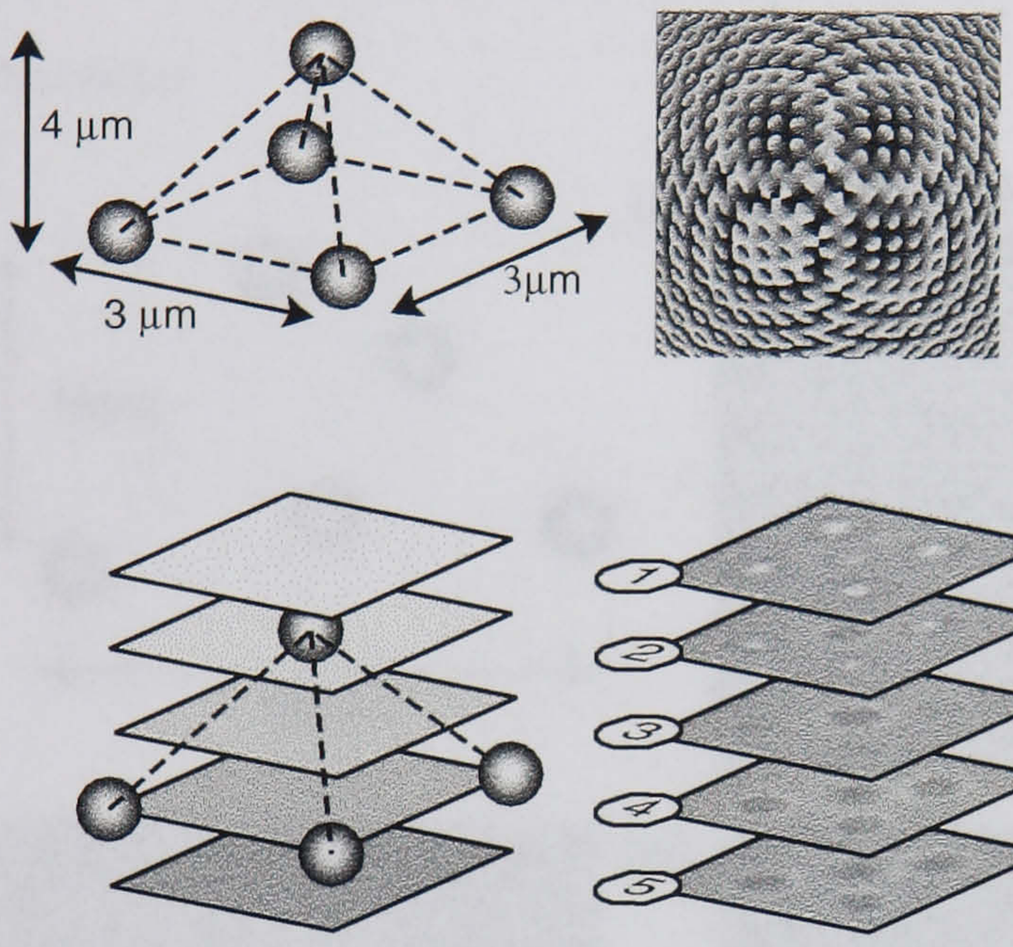

Figure 7.5: Illustration of the 3-dimensional nature of the pyramid, and the hologram used to create the structre. Pictures 1 to 5 are images taken from the actual structure. Picture 1 is taken with the camera focus above the pyramid, picture 2 is focussed on the top bead in the pyramid, picture 3 is taken in between the top bead and the base beads of the pyramid, picture 4 focuses on the 4 base beads and picture 5 is focussed below the structure. Refer to Section 7.4.1 for details.

7.4.2 Fluorescent permanent 3D structures

Images of the fluorescent spheres were taken once the gelatin had set and the trapping beam had been switched off. Figures 7.6 and 7.7 are examples of a series of images of two structures taken in both the optical tweezers and the confocal microscope.

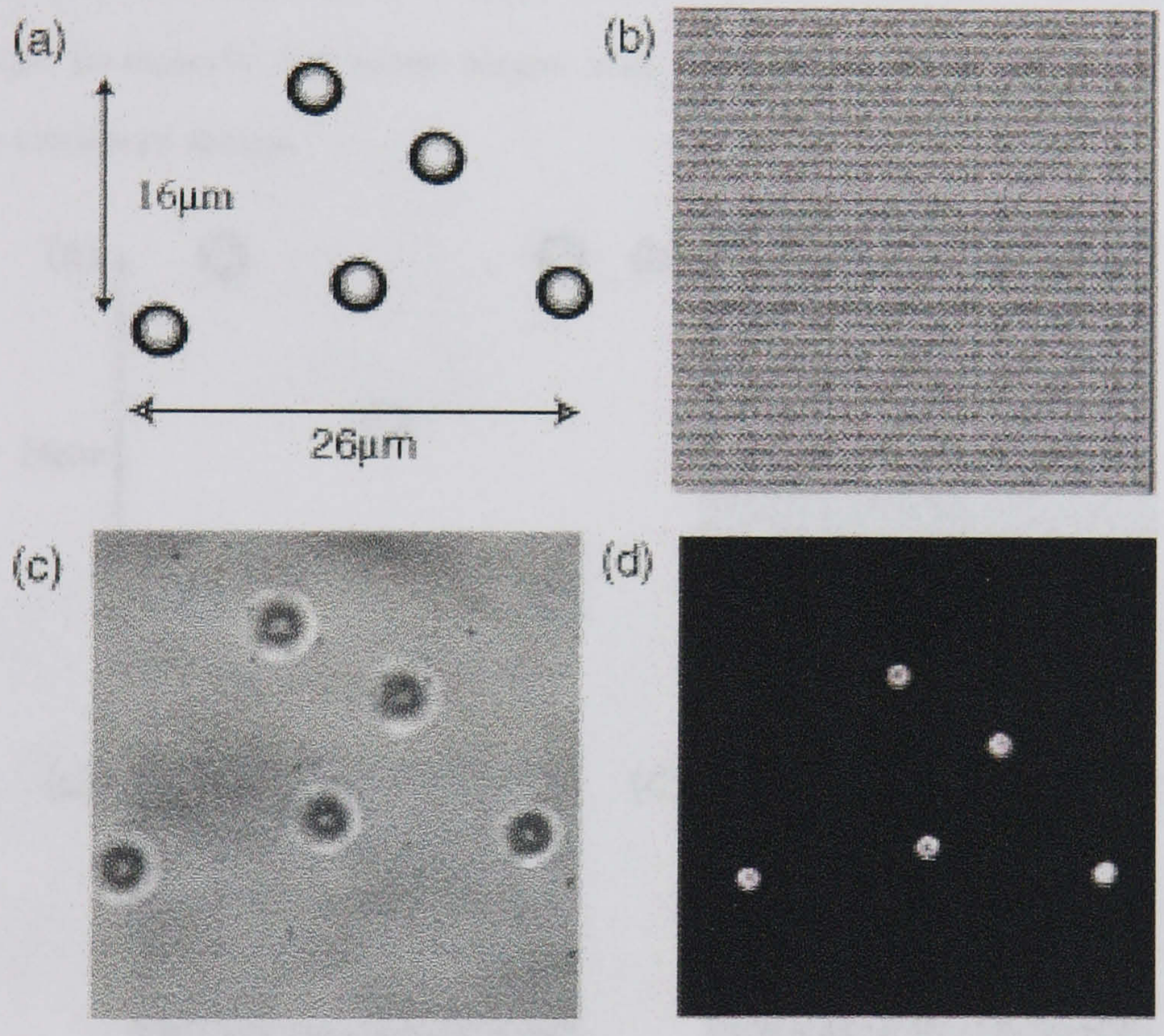

Figure 7.6: A 2D arrow shape of 1.8 μm sized spheres that are, if the bottom middle sphere is taken to be position (0,0), positioned at (-13,0), (13,0), (7,7) and (0,16) and illustrated in (a), (b) is the the hologram used to create the structure, (c) is the image taken in the optical tweezers and (d) is the confocal image confirming the structure in a confocal microscope using a x100 objective lens. Refer to Section 7.4.2.

Figure 7.6 shows a 2 dimensional arrow shape of 1.8 μm diameter spheres that has set 13 μm above the cover slip of the sample cell. A schematic diagram of the structure is shown in Figure 7.6(a). If the bottom middle

sphere is taken to be position (0,0) and the bottom row lies diredtly along the x axis, there are beads positioned at (-13,0), (13,0), (7,7) and (0,16). The hologram used to place the beads in these positions is also shown, Figure 7.6(b). However, upon polymerisation the structure became disfigured, Figure 7.6(c). There is also a picture of the same structure taken in the confocal microscope, Figure 7.6(d), and it can be seen that the fluorescent beads are in exactly the same shape and position as pre-determined in the optical tweezers setup.

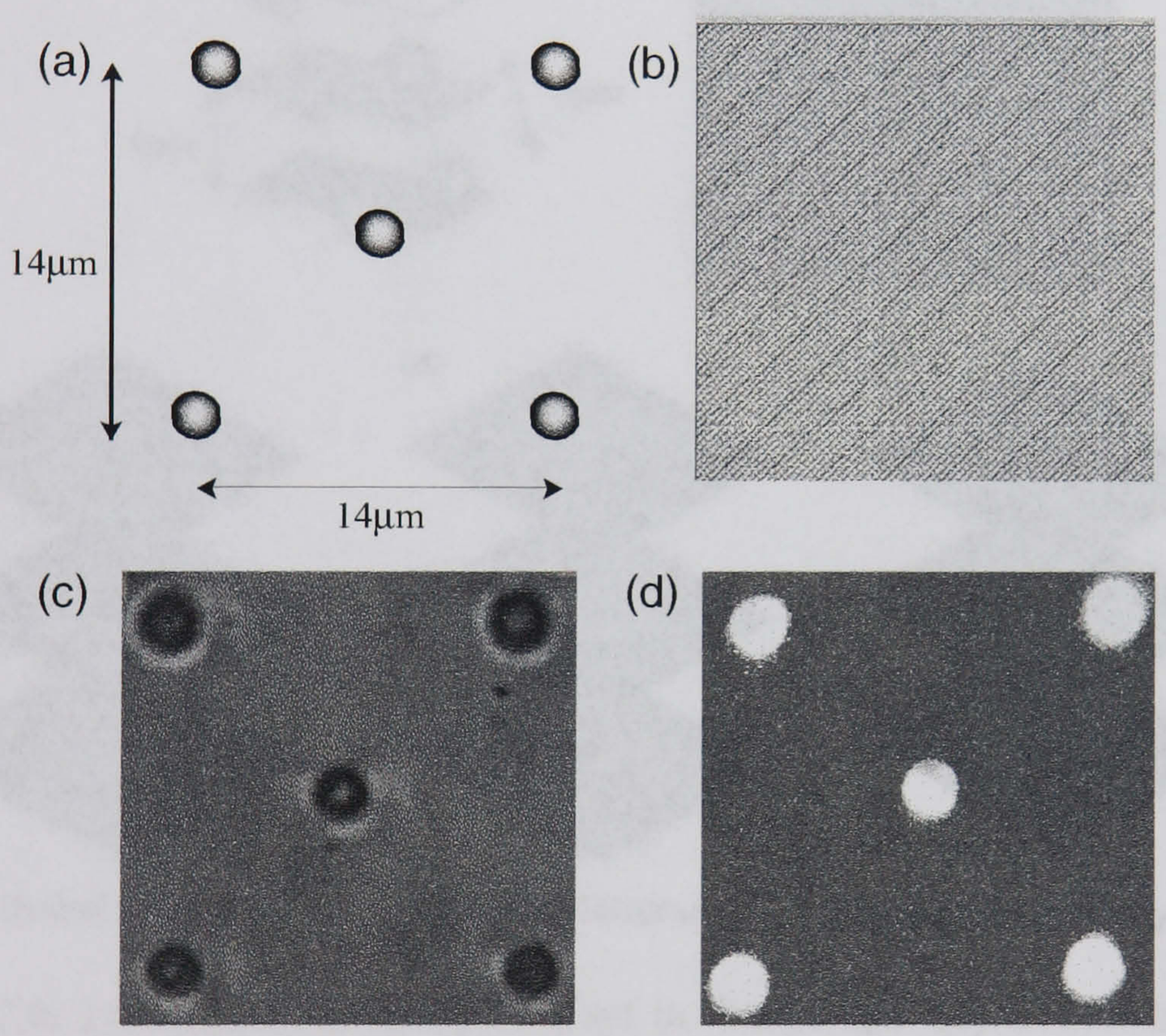

Figure 7.7: 1.8 μm fluorescent spheres produce a 14 μm $\times$ 14 μm square with a sphere at its centre, (a). Again, the hologram that produces this pattern is illustrated, (b), and the images obtained from the optical tweezers, (c), and confocal microscope, (d) using a x100 objective lens. See Section 7.4.2 for details.

Figure 7.7 shows the shape of the number 5 as it appears on a dice, the schematic of which is shown in Figure 7.7(a). The 1.8 μm fluorescent spheres

produce a 14 μm $\times$ 14 μm square with a sphere at its centre. Again, the hologram that produces this pattern is illustrated, Figure 7.7(b), and the images obtained from the optical tweezers, Figure 7.7(c), and the confocal microscope, Figure 7.7(d), confirms that the structure can be imaged under a different system and that the fluorescent spheres are not photobleached by the trapping laser light.

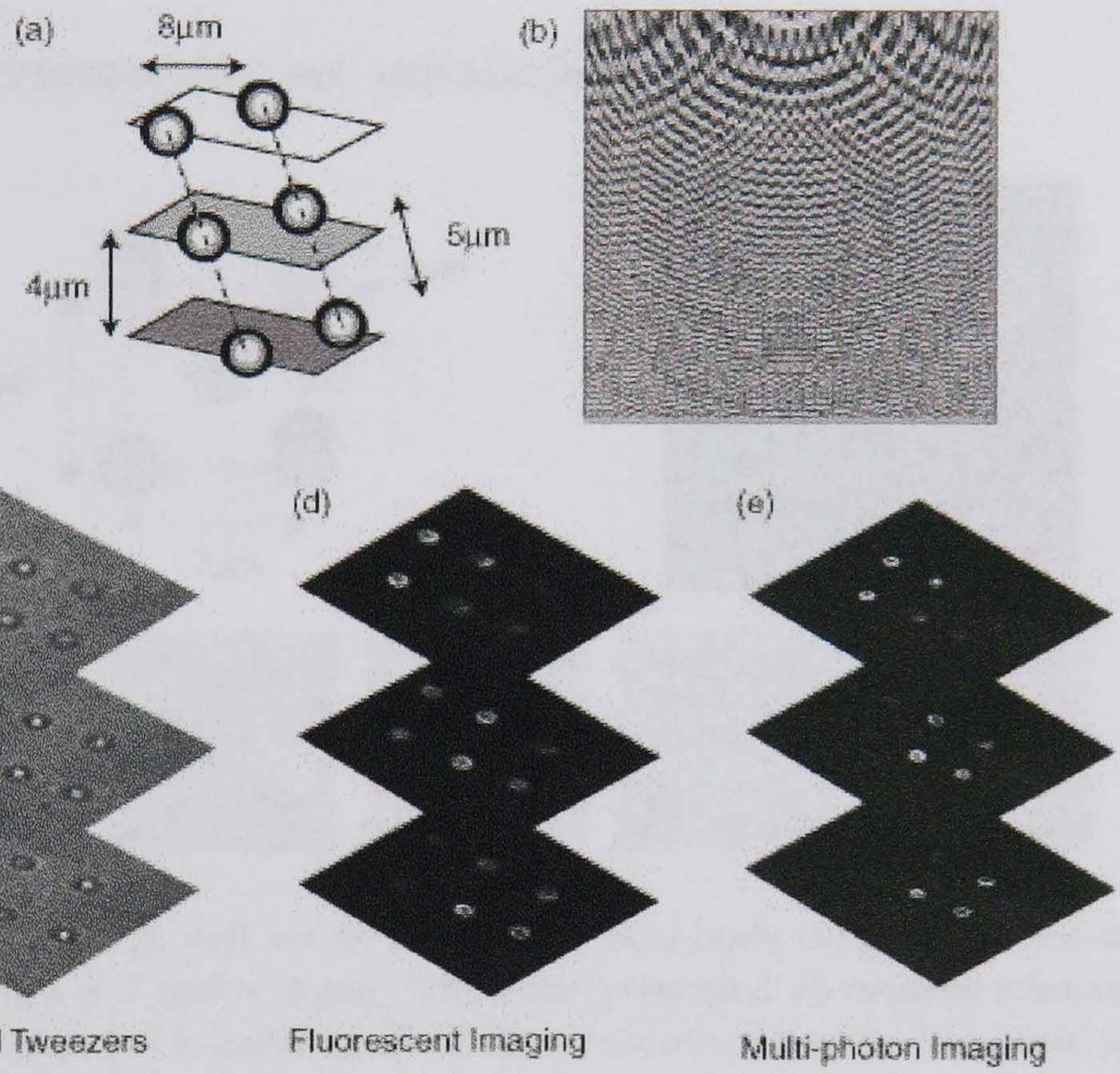

Figure 7.8: 1.8 μm fluorescent spheres set in three steps. (a) is the schematic of the structure and (b) is the hologram used to create it. Column (c) shows the images taken from the optical tweezers, (d) the images from the fluorescence imaging and (e) from the multi-photon imaging using a x100 oil immersion objective lens. Refer to Section 7.4.2.

In Figure 7.8 the zero order of the laser beam was removed using a beam stop at an intermediate beam waist before the laser entered the back of the microscope objective. Six spheres were trapped in pairs in three different

planes, separated by 8 μm in the x direction and 3 μm in the y direction and 4 μm in the z direction. The schematic of the structure is illustrated in Figure 7.8(a) with the hologram used to create the desired structure shown in Figure 7.8(b). Images of the permanently set structure were taken using the optical tweezers, Figure 7.8(c), the confocal microscope, Figure 7.8(d) and using multi-photon imaging, Figure 7.8(e).

7.4.3 Permanently set unlabelled *E. coli*

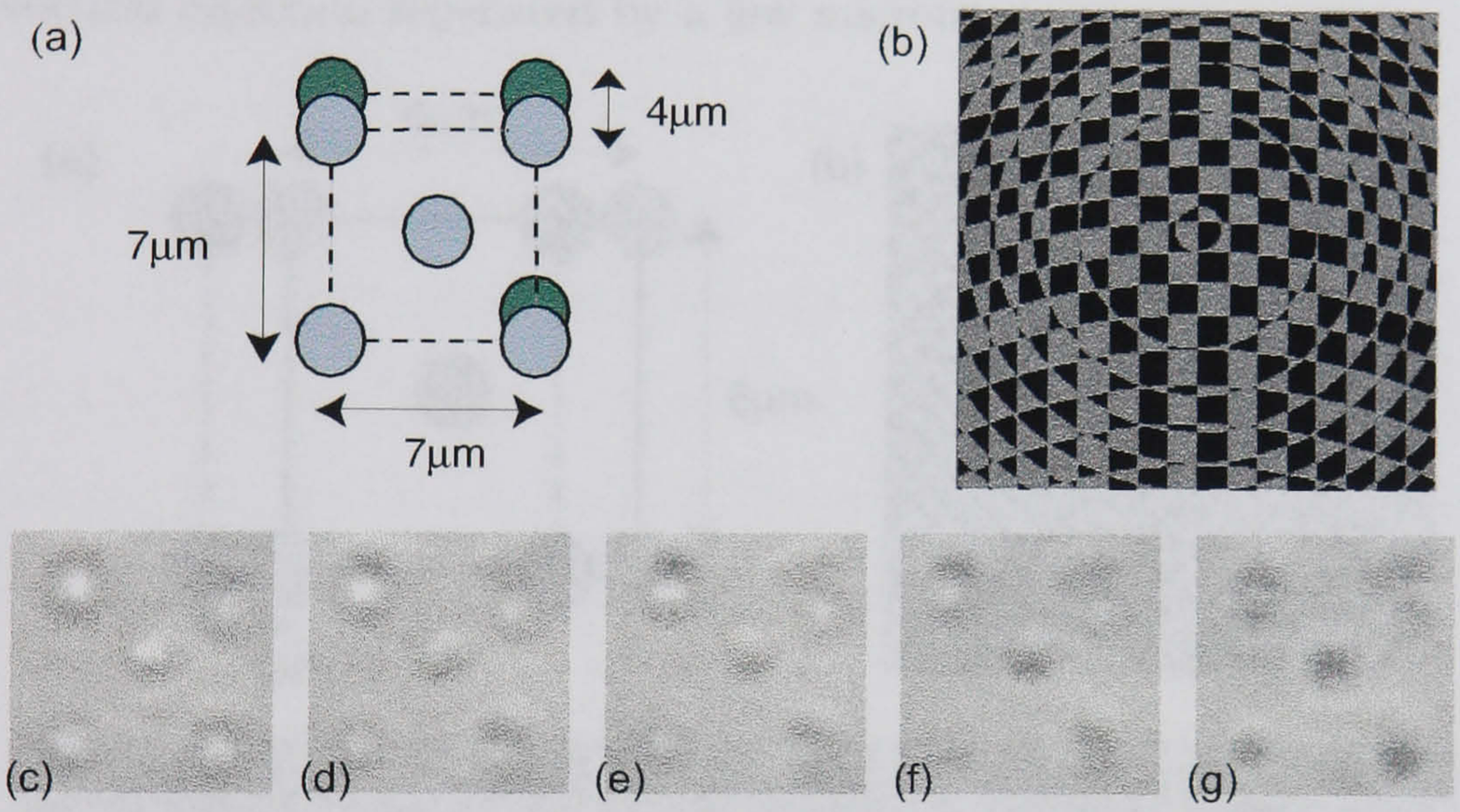

Figure 7.9: HB101 *E. coli* set at the corners of a body centered lattice with dimension 7 μm $\times$ 7 μm $\times$ 4 μm. The cube is rotated 10 degrees relative to the x-axis. Figure (a) is a schematic of the structure, (b) is the hologram used to make the structure whilst Figures (c) through (h) are images of the scan through of the structure at various depths. There are two *E. coli* trapped directly above one another in the z direction at each corner except for the bottom left hand corner where there is only one *E. coli* trapped on the upper plane of the cube. This was done to help visualise the difference between a single trapped *E. coli* and two *E. coli* trapped in the vertical direction separated by a few microns. See Section 7.4.3.

The zero order was left in place in order to create a trap at the centre of the rectangular lattice. The cube was rotated 10 degrees relative to the

x-axis to help image the *E. coli* that was trapped on the bottom plane of the cube. Figure 7.9(a) is a schematic of the structure, 7.9(b) is the hologram used to make the structure whilst Figures 7.9(c) through 7.9(g) are images of the structure at various depths as it was scanned in z using the PZT stage. There are two *E. coli* trapped directly above one another in the z direction at each corner except for the bottom left hand corner where there is only one *E. coli* trapped on the upper plane of the cube. This was done to help visualise the difference between a single trapped *E. coli* and two *E. coli* trapped in the vertical direction separated by a few microns.

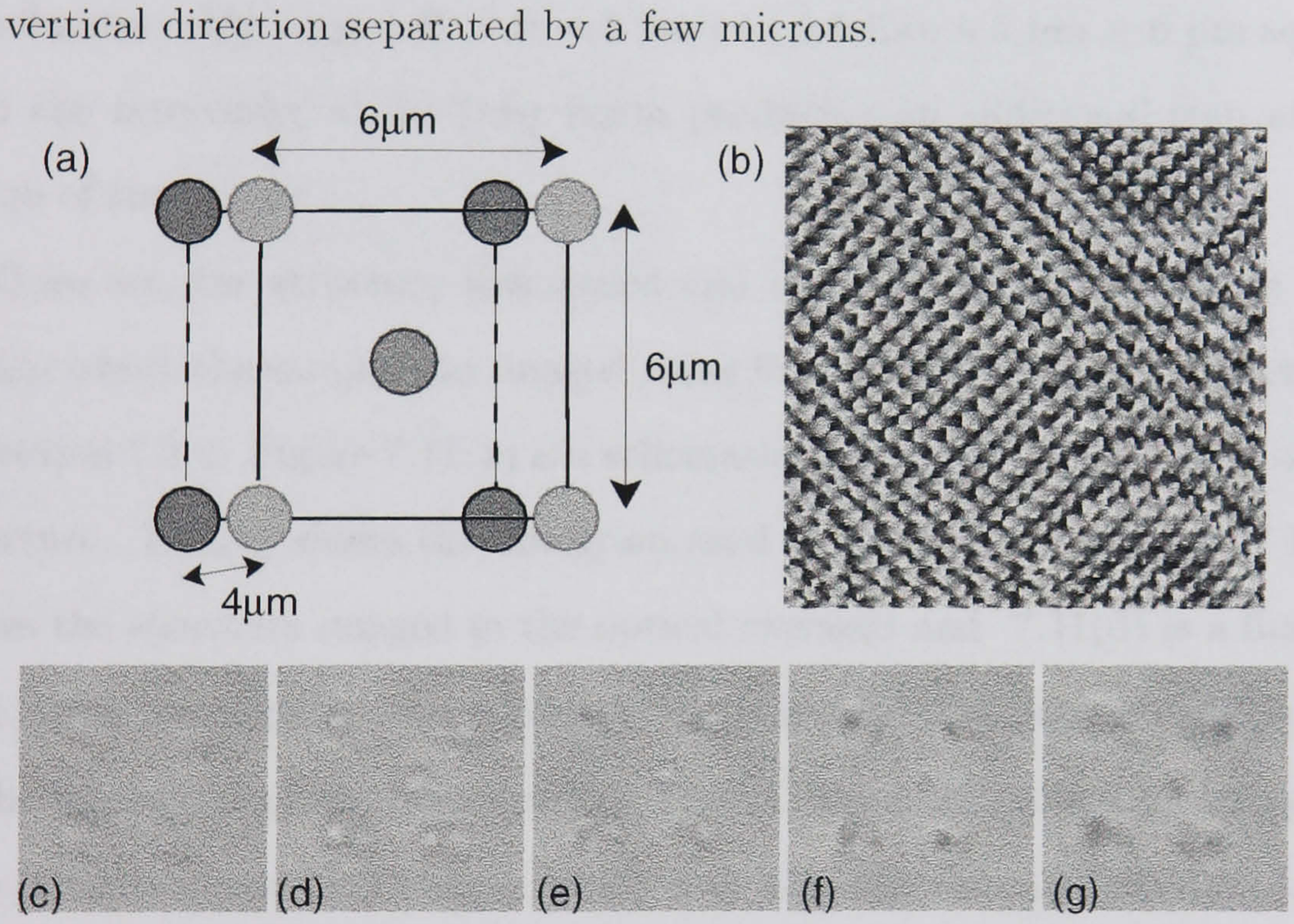

Figure 7.10: HB101 *E. coli* set at the corners of a body centered lattice with dimension 6 μm × 6 μm × 4 μm. Figure (a) is a schematic of the structure, (b) is the hologram used to make the structure whilst Figures (c) through (g) are images of the structure at various depths. There are two squares creating the structure that are separated by 4 μm axially and by 1 μm in the x direction. The zero order creates the trap at the centre of the cube. See Section 7.4.3.

Figure 7.10 is another body centered cubic structure, this time with *E. coli* trapped at all nine lattice points. The *E. coli* was set at the corners of a

body centered lattice with dimension 6 μm $\times$ 6 μm $\times$ 4 μm. Figure 7.10(a) is a schematic of the structure. 7.10(b) is the hologram used to make the structure whilst Figures 7.10(c) through 7.10(g) are images of the structure at various depths. There are two squares creating the structure that are separated by 4 μm axially and by 1 μm in the x direction. The zero order created the trap at the centre of the cube.

7.4.4 Permanently set labelled *E. coli*

The fluorescently tagged *E. coli* was used to produce a 6 μm $\times$ 6 μm square with the zero order of the laser beam producing an additional trap at the centre of the square.

Once set, the structure was sealed and transported to Strathclyde University where the sample was imaged using fluorescence imaging as described in Section 7.2.2. Figure 7.11(a) is a schematic diagram of the geometry of the structure, 7.11(b) shows the hologram used to create the structure, 7.11(c) shows the structure imaged in the optical tweezers and 7.11(d) is a fluorescent image recorded in the confocal setup. It is clear that there are differences in the intensities of the fluorescence. The *E. coli* trapped and set using the zero order is particularly weak, which may also have been effected by being trapped in the zero order of the laser beam and was probably photobleached. The zero order has considerably more power in it than the others used for trapping.

7.4.5 Viability of *E.coli* in gelatin

E. coli taken from the exponential growth phase and mixed with nutrient broth and gelatin to produce a 3% wt/v sample was imaged at various times.

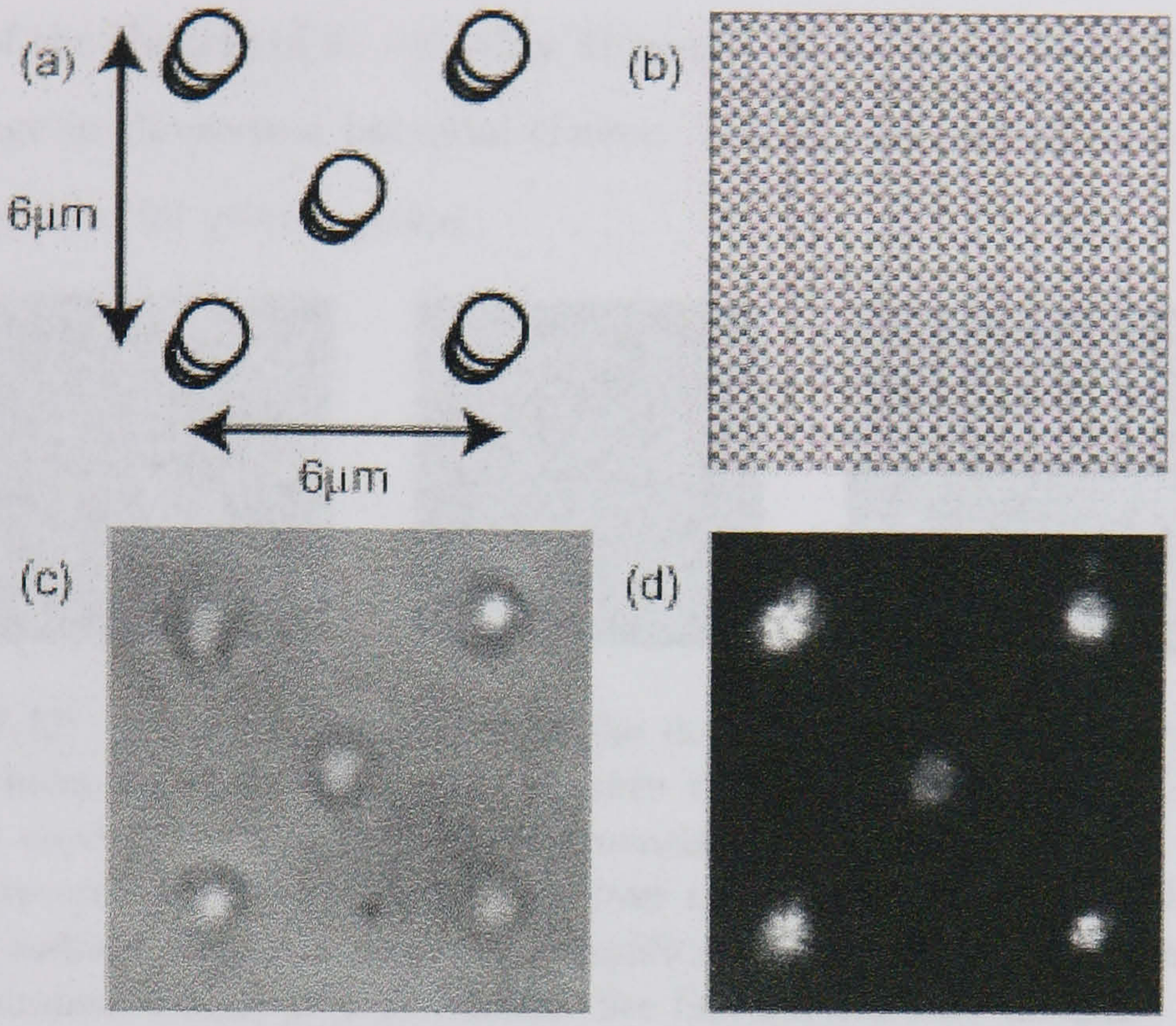

Figure 7.11: Tagged *E. coli* set in the shape of a number 5 on a dice. Figure (a) shows the geometry of the structure, (b) shows the hologram used to create the structure, (c) shows the structure imaged in the optical tweezers and (d) is a fluorescent image recorded in the confocal setup. See Section 7.4.4 for details.

Propidium iodide stains the bacteria and causes it to fluoresce when the cell membrane is damaged, making it ideal for identifying damaged or decayed *E. coli* cells within a population. It has no effect on *E. coli* that are intact [6].

Typically, accumulative scans were used in order to detect any propidium iodide fluorescence as the signal is initially very weak when the cell membranes are first damaged. Direct scans on these cells revealed no signal indicating no damage, hence the accumulative scans showed details of where the bacteria started to decay.

With reference to Figure 7.12 it can be seen that there was some decay

in one of the clusters of *E. coli* after 41 hours. At 45 hours there were signs of damage in the second bacterial cluster. The *E. coli* used here was taken in its exponential growth phase.

Figure 7.12: Fluorescence images of the decay of an *E. coli* cluster in 3% wt/v gelatin and nutrient broth mixture that was 41 hours old. The *E. coli* was used when it was in its exponential growth phase. It can be seen that there are bacteria starting to die over the entire area of the cluster in a random fashion. The damage is not significant and was only detected using an accumulation scan over 20 frames. See Section 7.4.5 for details.

Statistics taken on this sample after 45 hours indicated that 30% of the bacteria were decayed, 70% were alive and none were completely dead at this time (n=50).

Figure 7.13 shows fluorescence images of the decay of an *E. coli* cluster in 3% wt/v gelatin and nutrient broth mixture which was 52 hours old. Again, the *E. coli* used was taken when it was in its exponential growth phase. It can be seen that there are bacteria starting to decay over the entire area of the cluster in a random fashion. The damage was not significant as it was only detected using an accumulation scan over 20 frames.

Fluorescence images were taken comparing the decay of *E. coli* (taken from the stationary phase) in 1.5%, 3% and 5% wt/v gelatin and nutrient broth mixture after being set in the gelatin for 23 hours. This was compared to *E. coli* (taken just before the exponential phase of growth was reached) set

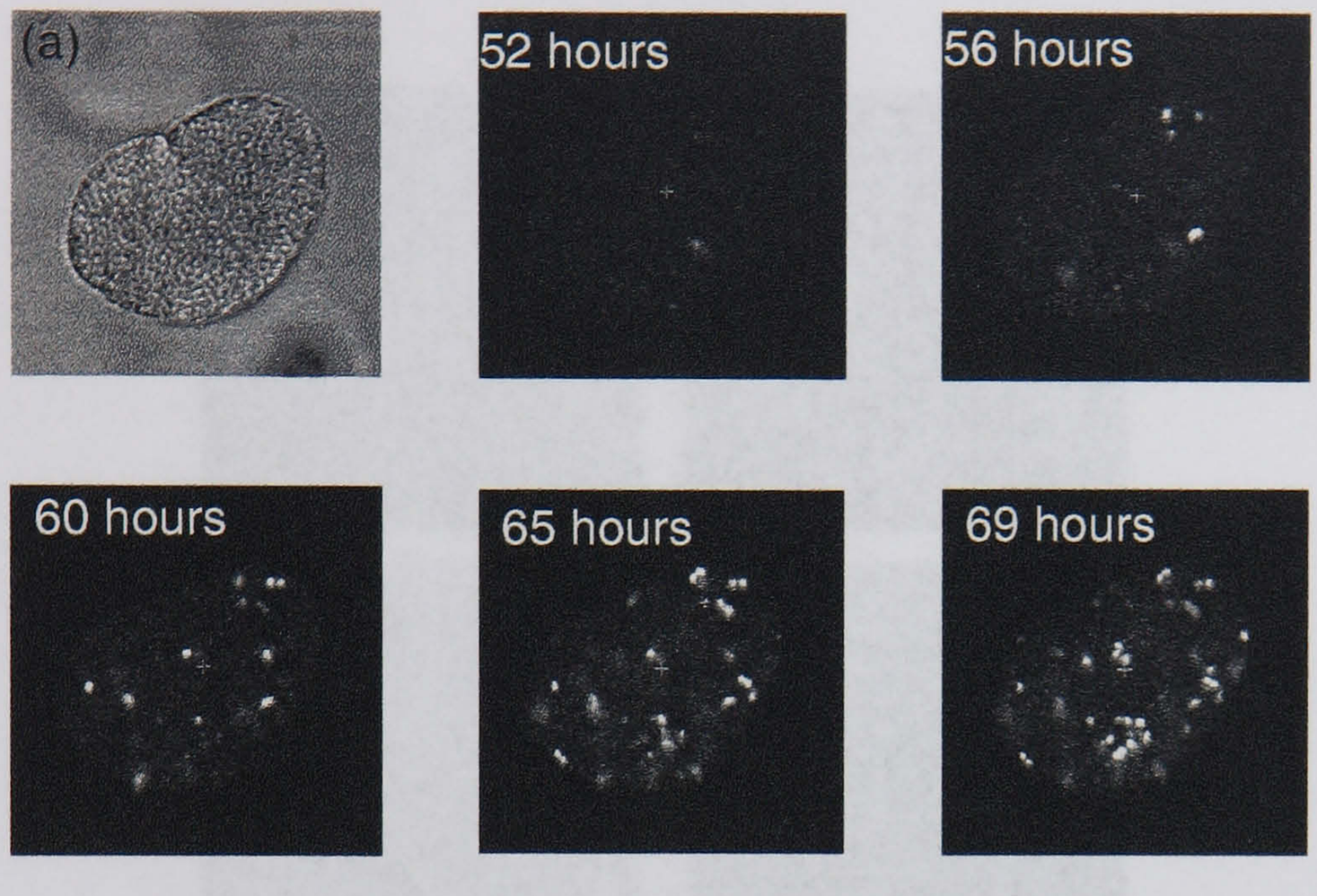

Figure 7.13: Fluorescent images of the decay of an *E. coli* cluster in 3% wt/v gelatin and nutrient broth mixture that was 52 hours old. The *E. coli* was used when it was in its exponential growth phase. It can be seen that there are bacteria starting to die over the entire area of the cluster in a random fashion. The damage is not significant and was only detected using an accumulation scan over 20 frames. Refer to Section 7.4.5.

in 3% wt/v gelatin. The damage was not significant and was only detected using an accumulation scan over 20 frames, refer to Figure 7.14.

With reference to the concentration of the gelatin the samples were suspended in, it was found that the *E. coli* (taken from the stationary phase) survived longest when the 5% wt/v solution was used. They started to decay after about 6 hours. This was followed by the 3% wt/v solution, where the bacteria started to decay after 4-5 hours, and then 1.5% wt/v solution, where the *E. coli* formed networks within the gelatin matrix and started to died relatively quickly i.e. after 90 minutes.

The *E. coli* in the 5% wt/v solution also multiplied the least. This was probably due to the fact that, at this concentration, the gelatin set very quickly and prevented the *E. coli* from multiplying. This may also explain

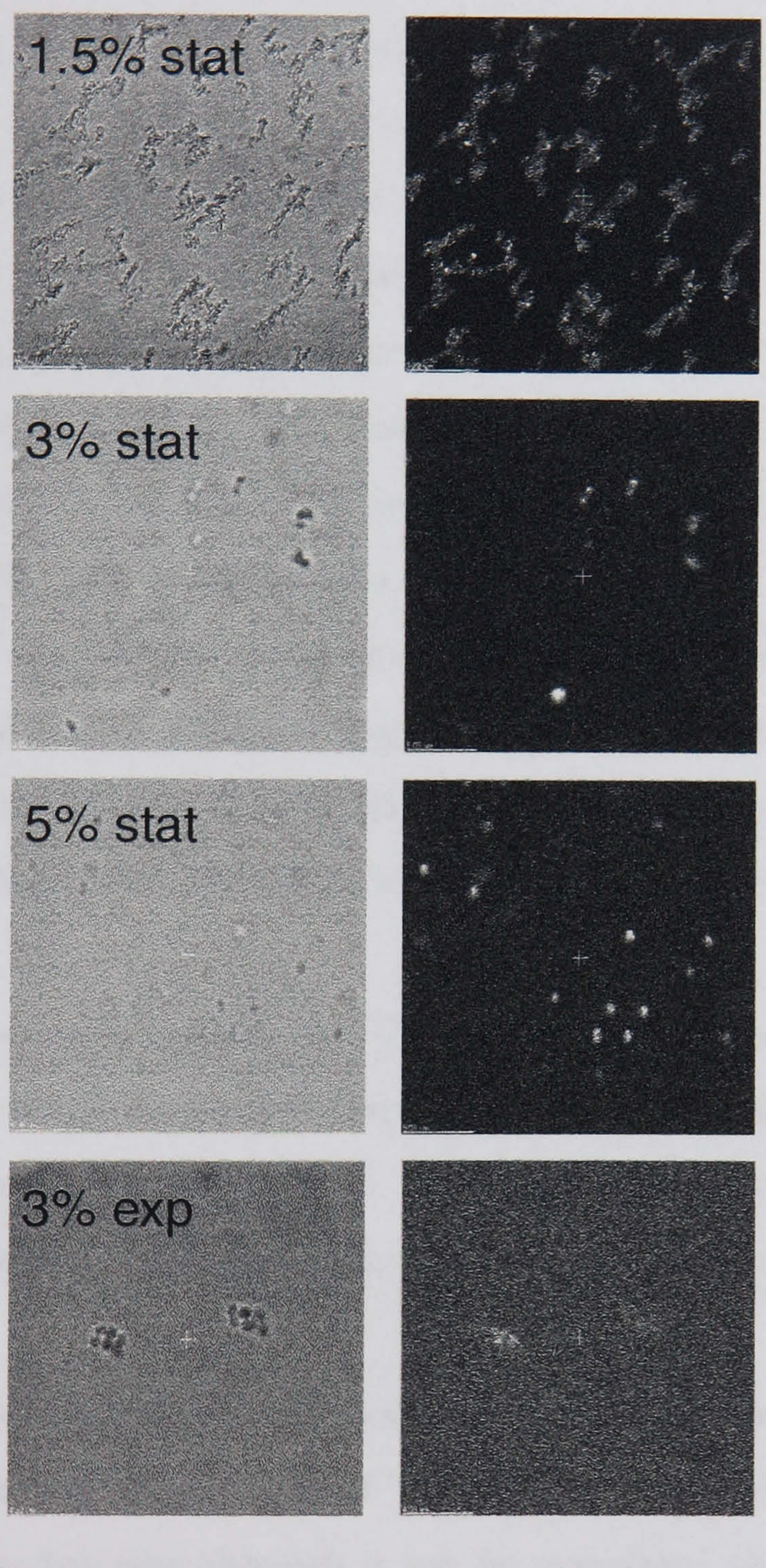

Figure 7.14: Fluorescence images comparing the decay of *E. coli* (taken from the stationary phase) in 1.5%, 3% and 5% wt/v gelatin and nutrient broth mixture after 23 hours. This is compared to *E. coli* (taken just before the exponential phase of growth was reached) set in 3% wt/v gelatin. The damage is not significant and was only detected using an accumulation scan over 20 frames. For more details see Section 7.4.5.

why the bacteria in these samples survived for longer, as the nutrients in the gel surrounding the bacteria would sustain a single *E. coli* for a longer period of time than a cluster of *E. coli*. The bacteria in the 1.5% wt/v sample on the other hand, were still in a liquid gelatin solution after 90 minutes. These *E. coli* aggregated together and died relatively quickly. As with other clusters, it would be more difficult for the bacteria at the centre of the islands to feed than those at the edge. It is possible that diffusion gradients lead to the local depletion of nutrients with no regeneration. Compensating for this realisation could result in the bacteria living longer.

In order for the permanent setting of bacteria within a gelatin matrix to become a useful tool in a microbiology laboratory, the bacteria has to live within the gelatin medium and should be recoverable after setting. Optical tweezers have been used previously to determine the bacterial viability of trapped *E. coli* [6].

Even after being set in gelatin for 72 hours with nutrient broth, the *E. coli* (taken from the stationary phase) could be recovered and cultured overnight on an agar plate incubated at 37°C. All samples tested produced colony forming units, whilst the control segment shows no contamination as shown in Figure 7.15.

It was noticed that when the *E. coli* multiplied within the gelatin before it hardened, that the *E. coli* formed "clusters" or "bacterial islands". It is unclear why this happens although it can be postulated that: Firstly, the strain of *E. coli* used in these experiments, MC4100, lacks the flagella that most *E. coli* use to move around. This could easily prevent the bacteria from moving away from each other after division. Secondly, the gelatin itself may be a factor in preventing the cells from separating effectively.

Figure 7.15: Even after being set in gelatin for 72 hours with nutrient broth, the *E. coli* could be recovered and cultured overnight on an agar plate incubated at 37°C. All five samples tested produced colony forming units, whilst the control segment shows no contamination. See Section7.4.5.

Although the bacteria in this study were not trapped within an optical tweezers, previous work looking at MC4100 *E. coli* stained with propidium iodide trapped using a 830 nm trapping laser concluded that neither the dye or trapping laser had any effect on the doubling time of the bacteria [6]. Regardless of power, the *E. coli* could double at room temperature approximately every 50 mins in the stationary phase provided conditions were good.

7.5 Conclusions

7.5.1 Permanent setting of silica microparticles

Whereas 2D permanent structures have already been demonstrated, it has been shown here that it is possible to create 3D structures consisting of 2

μm diameter silica spheres in a gelatin polymer using holographic optical tweezers. These structures can remain intact for a number of weeks.

7.5.2 Fluorescent permanent 3D structures

Both 2D and 3D structures were created and set using fluorescent spheres within a gelatin matrix using optical tweezers. These structures were sealed and successfully moved to a different geographic location, and re-imaged using confocal and multi-photon microscopy. The 3D permanently set structure imaged in using confocal and multi-photon microscopy further demonstrates the "optical sectioning" ability of these techniques.

7.5.3 Permanently set unlabelled *E. coli*

It was possible not only to trap and set dielectric particles in a gelatin matrix, but also to trap and set biological objects. *E. coli* was trapped and set in true 3D cubic structures, with *E. coli* trapped in positions axially above and below each other, which had not been done with the silica or fluorescent spheres.

7.5.4 Permanently set labelled *E. coli*

It was possible to add a fluorescent tag to the *E. coli* and set the bacteria in a 2D structure within the optical tweezers. It was possible to find the structure again and re-image it ex-situ using confocal microscopy. This ability to tag and position the *E. coli* in a pre-determined position could provide a useful tool in the image staining of many bacteria in the future.

7.5.5 Viability of *E.coli* in gelatin

It was shown that *E. coli* bacteria could survive within a gelatin and nutrient broth mixture for up to 8 days. There would appear to be two major contributing factors determining the behaviour and lifetime of the bacteria. Firstly, the concentration of the gelatin used to create the matrix that the bacteria was set in and secondly, whether the *E. coli* used was taken from stationary or exponential growth phases. Bacteria taken from an exponential growth phase multiplied to form bacterial "clusters" while the bacteria taken from a stationary growth phase did not normally multiply to the same extent and resulted in individually set *E. coli*.

7.6 Conclusion

The flexible nature of holographic optical tweezing techniques opens up the possibility of a wide range of future applications.

The techniques demonstrated may offer significant advantages in fields as diverse as photonic crystal construction, creating metrological standards within micro and nano technology and creation of structures within a biocompatible host, enabling future applications in biotechnology.

This advancement of holographic optical tweezers opens up the possibility for organising microscopic matter into novel or complex geometries, allowing for the study of the collective behaviour of many-body cell structures, particularly since it has been demonstrated that *E. coli* is viable in such a gel matrix for a period of days.

It was interesting to note that the infra-red laser appeared to heat the gelatin mixture less than the green laser using exactly the same solutions.

Using the infra-red laser the gelatin solution set within approximately 1 hour compared to 3-4 hours using the 532 nm laser.

Absorption spectra and Faraday rotation measurements have previously been made on nanocrystals randomly embedded in gelatin [143] and magnetic susceptibility measurements have been carried out on ground single crystals held inside a gelatin capsule [144]. In future, the use of permanent 3D structuring of composites using optical tweezers may provide a new method by which materials components can be combinatorially produced, to create a greater diversity of new materials. Determination of crystal structures using this new technique could also prove invaluable in evaluating novel material properties, allowing for interesting device applications [145, 146].

Further applications may lie within the field of biotechnology and bioengineering. Previously, optical tweezers have provided a valuable tool in research, with applications including measuring the compliance of bacterial tails [2], measuring the forces exerted by motor proteins [3] and stretching DNA molecules [104]. In the context of cell manipulation, gelatin is already commonly used as a substrate for the culture of a variety of cells, including both bacterial and mammalian cells. One long-term aim in bioengineering has been to produce artificial tissue to replace organs that have failed. The importance of the methods described in this paper may, in future, be illustrated by the ability to organize cells spatially into well-defined 3D arrays to help in tissue replacement therapies. In one example, it may prove possible to build upon the observation that hepatocytes cultured as a monolayer quickly loose specific functions, whilst those same cells in a quasi 3D collagen matrix (mimicing their natural structure) retain these same functions for weeks in culture [147]. It is thus possible to envisage the construction of

better artificial organs, in which one or more cell types are precisely arranged in pre-defined geometries with respect to each other. The fact that bacteria can survive, and still reproduce, after being set within the gelatin makes all of these options a more realistic avenue of research to pursue.

The work presented in this Chapter has resulted in the following journal publication:

- P. Jordan, H. Clare, L. Flendrig, J. Leach, J. Cooper and M. Padgett, "Permanent 3D microstructures in a polymeric host created using holographic optical tweezers", J. Mod. Opt. 51, 627-632 (2004).

- Pamela Jordan, Jonathan M. Cooper, Mattias Goksör, Dag Hanstorp, Amanda Wright, John Girkin, Paul Blackburn and Miles Padgett, "Ex-situ imaging of fluorescent permanent 3D structures created using holographic optical tweezers", in preparation 2005.

Chapter 8

Conclusions and future work

This thesis has demonstrated some new applied uses of optical tweezers, most of which are cross-disciplinary and, in addition to physics, has involved branches of chemistry and biology. Chapters 3 – 5 were concerned with the development of suitable partially coated microparticles such that they could be used in the optical tweezers to stimulate and record a SERRS signal. Chapters 6 – 7 described holographic optical tweezers for the trapping and manipulation of several particles simultaneously and independently of each other with the option to turn them into permanent structures.

8.1 SERRS detection in optical tweezers

It has been demonstrated that it is possible to trap partially silvered microspheres using a standard TEM_{00} 532 nm focussed optical trap with an efficiency, $Q = 0.086 \pm 0.008$, similar to that of a dielectric particle, $Q = 0.092 \pm 0.004$, at zero axial displacement. This is far simpler than previous methods of trapping for conventional metallic particles that involved scanning or annular beams to create an optical "cage" around the microparticle. More importantly, it allows the three dimensional manipulation of the particle which was

not possible with some of the metallic trapping methods that relied upon the repulsive nature of beam. In short, this new kind of partially silvered particle allows for the easy trapping associated with dielectrics whilst allowing the metallic nature of the particle to be exploited.

It was found that the deposition of silver using the reduction of the Tollen's reagent on the spheres ceased after 10-20 minutes, implying that the coating time is not critical after this time scale. It was also shown that the silver coating on the silica spheres was not uniform, but consisted of silver deposits on the surface. Consequently, silica spheres that were partially coated with less than 25% of silver on their surface could be trapped easily. Interestingly, after a few minutes of coating, there was no appreciable difference in the percentage of particles that could be trapped, implying that the coating effectively takes place within the first few minutes of the Tollen's reaction.

The trapping mechanism of these partially silvered particles may be explained by the fact that the particles are sufficiently transparent to enable refraction of the beam through the sphere to produce a net attractive force to the region of highest light intensity. In other words, it was trapped using a similar mechanism to that of a dielectric particle.

One practical application of trapping partially silvered microparticles, that have rough silver deposits on their surface, is that they can be coated with an azo dye and used to generate and record SERRS spectra. This technique relies on optical signal enhancement, associated with the interaction of a molecular species with a surface plasmon, generated at a metal surface. By over coming the difficulties for trapping metallic particles, it was possible to collect an intense, characteristic vibrational spectrum, associated with a

molecular species adsorbed on the surface of a partially silvered particle in real time.

The dye and silver coated particles could be easily trapped within a standard 532 nm TEM_{00} optical tweezers. The azo dye was chosen such that its SERRS response could be stimulated by 532 nm excitation light. In this case the 532 nm laser both trapped the particle and stimulated the SERRS signal. Interestingly, it was the particles with the weakest SERRS emission that were the easiest to trap. This may be indicative of the amount of silver coating on the surface of the sphere. In all cases, the SERRS from the particles stopped once the particles were trapped. This is most likely due to the fact that the dye photobleached from the intense laser beam.

The dye further reduced the Q value of particles in the optical tweezers to Q=0.061±0.002, as the dye makes the particle absorb the trapping light more strongly. However, the amount of silver on the surface still dominated whether the particle could be trapped easily or not. The stronger the dye concentration, the stronger the visual SERRS emission appeared on the CCD camera. However, the SERRS emission for a sphere trapped in a 532 nm optical tweezers only lasted for 100 ms or less.

In order to increase the length of time the SERRS response could be recorded for, the optical setup was changed. In the new setup, a 1064 nm optical tweezers was constructed, with microwatt's of 532 nm colinear excitation light generated through the use of a frequency doubling crystal. By introducing small quantities of 532 nm light into an infra-red optical trap, via a frequency doubling KTP crystal, it was possible to record a SERRS signal from the trapped particle that was sustainable over periods of a few minutes, compared to 100 ms for a 532 nm optical trap.

This ability to trap partial metallic beads to create a combined SERRS and optical tweezers system provides an attractive platform for microsystems and microfluidic technologies in which sensory particles can be independently manipulated both with respect to each other and/or other entities. Furthermore, the use of an IR laser makes the whole system more biologically "friendly" than if a visible wavelength laser was used, resulting in less damage to the sample. By combining the spectroscopic nature of SERRS with the ability to trap and manipulate these beads, it will in future be possible to develop new platforms, such as biological probes, that can readily compete with those being developed using fluorescence.

Whereas Raman and resonance Raman have been routinely carried out in optical tweezers, the ability to trap and manipulate a partially silvered microparticle in an optical trap opens up the possibility of future SERS and SERRS related experiments in optical tweezers. Trapping a partially silvered sphere and dragging it over a bar code of different dyes laid down in parallel lines on the cover slip of a sample cell may offer one such experiment.

8.2 3D microstructures in optical tweezers

Whereas the previous results only required the optical tweezers to trap one object at a time, it was shown that holographic optical components can be used to split the incident laser beam into several beams such that many objects can be trapped simultaneously. In addition to introducing lateral displacements, holograms allow particles to be displaced axially along the laser beam, giving full 3D control of trap positions. The holographic optical tweezers constructed here used an SLM as its diffractive component.

It was shown that, using a variety of different hologram generation techniques, that symmetric and arbitrary 3D structures could be constructed and manipulated in real time.

By their nature, holographic optical tweezers can be computer controlled in order to adjust the symmetry, periodicity and depth of any desired pattern. Furthermore, these patterns can be extended to be quasiperiodic or aperiodic, allowing for a range of "crystals" to be designed. This will not only enable current optical tweezers applications to be optimised, but will also offer exciting prospects for new technologies such as lab-on-a-chip, where micro-manipulation of multiple objects is a key issue.

By combining the ability to create and manipulate 3D structures using holographic optical tweezers, it was demonstrated that these structures could be made permanent by fixing them in a gelatin matrix.

Permanent 3D structures, that could be created and then imaged ex-situ, were constructed using silica spheres, fluorescent spheres, *E. coli* and fluorescently tagged *E. coli*. A bacterial viability study on *E. coli* within a gelatin matrix prepared with nutrient broth confirmed that the bacteria could live within such an arrangement for a period of days.

In future, the use of permanent 3D structuring of composites using optical tweezers may provide a new method by which materials components can be combinatorially produced, to create a greater diversity of new materials. Seeding of crystal structures using this new technique could also prove invaluable in evaluating novel material properties, allowing for interesting device applications.

The techniques demonstrated may offer significant advantages in fields as diverse as photonic crystal construction, creating metrological standards

within micro and nano technology and creation of structures within a biocompatible host, enabling future applications in biotechnology. In the context of cell manipulation, gelatin is already commonly used as a substrate for the culture of a variety of cells, including both bacterial and mammalian cells. However, the size of mammalian cells (typically 10–20 μm diameter) makes them different to trap optically compared to bacteria (typically 1–10 μm diameter). One long-term aim in bioengineering has been to produce artificial tissue to replace organs that have failed. The importance of the methods described here may, in future, be illustrated by the ability to organize cells spatially into well-defined 3D arrays to help in tissue replacement therapies. It is thus possible to envisage the construction of better artificial organs, in which one or more cell types are precisely arranged in pre-defined geometries with respect to each other. The fact that bacteria can survive, and still reproduce, after being set within the gelatin makes all of these options a more realistic avenue of research to pursue.

Bibliography

[1] A. Ashkin, J. M. Dziedzic, J. E. Bjorkholm, and S. Chu. Observation of a single-beam gradient force optical trap for dielectric particles. *Opt. Lett.*, 11:288–290, 1986.

[2] S. M. Block, H. C. Blair, and H. C. Berg. Compliance of bacterial flagella measured with optical tweezers. *Nature*, 338:514 518, 1989.

[3] J. T. Finer, R. M. Simmons, and J. A. Spudich. Single myosin molecule - piconewton forces and nanometer steps. *Nature*, 368:113–119, 1996.

[4] J. E. Molloy, J. E. Burns, J. C. Sparrow, R. T. Tregear, J. Kendrick-Jones, and D. C. S. White. Single molecule mechanics of heavy-meromyosin and S1 interacting with rabbit or drosophila actins using optical tweezers. *Biophys. J.*, 68(4):298–305, 1995.

[5] S. Sato and H. Inaba. Optical trapping and manipulation of microscopic particles and biological cells by laser beams. *Opt. Quant. Electron*, 28:1-16, 1996.

[6] M. Ericsson, D. Hanstorp, P. Hagberg, J. Enger, and T. Nyström. Sorting out bacterial viability with optical tweezers. *J. Bacteriol.*, 182(19):5551-5555, 2000.

[7] M. Oskan, T. Pisanic, J. Scheel, C. Barlow, S. Esener, and S. N. Bhatia. Electro-optical platform for the manipulation of live cells. *Langmuir*, 19:1532–1538, 2003.

[8] Matthew J. Lang, Polly M. Fordyce, and Steven M. Block. Combined optical trapping and single-molecule fluorescence. *Journal of Biology*, 2(1):6, 2003.

[9] Hiroaki Misawa, Keiji Sasaki, Masanori Koshioka, and Noboru Kitamura. Multibream laser manipulation and fixation of microparticles. *Appl. Phys. Lett.*, 60(3):310, 1992.

[10] Keiji Sasaki, Masanori Koshioka, Hiroaki Misawa, and Noboru Kitamura. Optical trapping of a metal particle and a water droplet by a scanning laser beam. *Appl. Phys. Lett.*, 60(7):807–809, February 1992.

[11] J. Hofkens, J. Hotta, K. Sasaki, H. Masuhara, and K. Iwai. Molecular assembling by the radiation pressure of a focused laser beam: Poly(N-isopropylacrylamide) is aqueous solution. *Langmuir*, 13:414 419, 1997.

[12] Alex Terray, John Oakley, and David W. M. Marr. Microfluidic control using colloidal devices. *Science*, 296:1841–1844, June 2002.

[13] Nicolas Garnier, Roman O. Grigoriev, and Michael F. Schatz. Optical manipulation of microscale fluid flow. *Phys. Rev. Lett.*, 91(5):054501, 2003.

[14] Yuichi Wakamoto, Senkei Umehara, Kazunori Matsumura, Ippei Inoue, and Kenji Yasuda. Development of non-destructive, non-contact single-cell based differential cell assay using on-chip microcultivation and optical tweezers. *Sensor Actuat. B-Chem.*, 96:693 700, 2003.

[15] M. P. MacDonald, G. C. Spalding, and K. Dholakia. Microfluidic sorting in an optical lattice. *Nature*, 426:421 424, November 2003.

[16] Xin-Cheng Yao and Alonso Castro. Optical trapping microfabrication with electophoretically delviered particles inside glass capillaries. *Opt. Lett.*, 28(15):1335–1337, August 2003.

[17] Jonas Enger, Mattias Goksör, Kerstin Ramser, Petter Hagberg, and Dag Hanstorp. Optical tweezers applied to a microfluidic system. *Lab Chip*, 4:196–200, 2004.

[18] Justin E. Molloy and Miles J. Padgett. Light, action: optical tweezers. *Contemp. Phys.*, 43(4):241–258, 2002.

[19] Justin E. Molloy, Kishan Dholakia, and Miles J. Padgett. Preface: Optical tweezers in a new light. *J. Mod. Opt.*, 50(10):1501–1507, 2003.

[20] H. Misawa and S. Juodkazis. Photophysics and photochemistry of a laser manipulated microparticle. *Prog. Polym. Sci.*, 24(5):665 697, August 1999.

[21] David G. Grier. A revolution in optical manipulation. *Nature*, 424:810-816, August 2003.

[22] Thomas T. Perkins, Hung-Wen Li, Ravindra V. Dalal, Jeff Geles, and Steven M. Block. Forward and reverse motion of single RecBCD molecules on DNA. *Biophys. J.*, 86:1640–1648, March 2004.

[23] Erik Fällman, Staffan Schedin, Jana Jass, Magnus Andersson, Bernt Eric Uhlin, and Ove Axner. Optical tweezers based force measurement system for quantitating binding interactions: system design

and application for the study of bacterial adhesion. *Biosens. Bioelectron.*, 19:1429–1437, 2004.

[24] Vincent R. Daria, Peter J. Rodrigo, and Jesper Glückstad. Dynamic formation of optically trapped microstructure arrays for biosensor applications. *Biosens. Bioelectron.*, 19:1439–1444, 2004.

[25] Tudor N. Buican, Miriam J. Smyth, Harry A. Crissman, Gary C. Salzman, Carleton C. Stewart, and John C. Martin. Automated single-cell manipulation and sorting by light trapping. *Appl. Opt.*, 26(24):5311 5316, December 1987.

[26] J. Arlt, V. Garcés-Chávez, W. Sibbett, and K. Dholakia. Optical micromanipulation using a Bessel light beam. *Opt. Commun.*, 197:239 245, October 2001.

[27] Kosta Ladavac and David G. Grier. Microoptomechanical pumps assembled and driven by holographic optical vortex arrays. *Opt. Express*, 12(6):1144 -1149, March 2004.

[28] Shoji Maruo, Koji Ikuta, and Hayaton Korogi. Submicron manipulation tools driven by light in a liquid. *Appl. Phys. Lett.*, 82(1):133 135, January 2003.

[29] Vincent R. Daria, René L. Eriksen, and Jesper Glükstad. Dynamic optical manipulation of colloidal systems using a spatial light modulator. *J. Mod. Opt.*, 50(10):1601–1614, 2003.

[30] Zhiwei Sun, Shenghua Xu, Guoliang Dai, Yinmei Li, Liren Lou, Quisheng Liu, and Ruzeng Zhu. A microscopic approach to studying colloidal stability. *J. Chem. Phys.*, 119(4):2399 2405, 2003.

[31] Anna T. O'Neil and Miles J. Padgett. Three-dimensional optical confinement of micron-sized metal particles and the decoupling of the spin and orbital angular momentum within an optical spanner. *Opt. Commun.*, 185:139–143, 2000.

[32] A. T. O'Neil, , I. MacVicar, L. Allen, and M. J. Padgett. Intrinsic and extrinsic nature of the orbital angular momentum of a light beam. *Phys. Rev. Lett.*, 88:03601, 2002.

[33] V. Garcés-Chávez, K. Volke-Sepulveda, S. Chávez-Cerda, W. Sibbett, and K. Dholakia. Transfer of orbital angular momentum to an optically trapped low-index particle. *Phys. Rev. A*, 66(063402), 2002.

[34] Dianwen Zhang, X. C. Yuan, S. C. Tjin, and S. Krishnan. Rigorous time domain of momentum transfer between light and microscopic particles in optical trapping. *Opt. Express*, 12(10):2220–2230, May 2004.

[35] Young and Freedman. *University Physics*. Addison Wesley, 9th edition, 1996.

[36] A. Ashkin. Atomic-beam deflection by resonance radiation pressure. *Phys. Rev. Lett.*, 25(19):1321–1324, November 1970.

[37] A. Ashkin. Acceleration and trapping of particles by radiation pressure. *Phys. Rev. Lett.*, 24(4):156–159, January 1970.

[38] Shunichi Sato, Yasunori Harada, and Yoshio Waesda. Optical trapping of microscopic metal particles. *Opt. Lett.*, 19(22):1807–1809. November 1994.

[39] P. A. Prentice, M. P. MacDonald, T. G. Frank, A. Cuschieri, G. C. Spalding, W. Sibbett, P. A. Campbell, and K. Dholakia. Manipulation and filtration of low index particles with holographic Laguerre-Gaussian optical trap arrays. *Opt. Express*, 12(4):593 600, February 2004.

[40] Peter John Rodrigo, Vincent Ricardo Daria, and Jesper Glückstad. Real time interactive optical micromanipulation of a mixture of high and low index particles. *Opt. Express*, 12(7):1417- 1425, April 2004.

[41] A. Ashkin and J. M. Dziedzic. Optical levitation by radiation pressure. *Appl. Phys. Lett.*, 19(8):283–285, October 1971.

[42] A. Ashkin. Trapping of atoms by resonance radiation pressure. *Phys. Rev. Lett.*, 40(12):729 732, March 1978.

[43] A. Ashkin. Forces of a single-beam gradient laser trap on a dielectric sphere in the ray optics regime. *Biophys. J.*, 61:569 582, February 1992.

[44] A. V. Kachynski, A. N. Kuzmin, H. E. Pudavar, D. S. Kaputa, A. N. Cartwright, and P. N. Prasad. Measurement of optical trapping forces by use of the two-photon-excited fluorescence of microspheres. *Opt. Lett.*, 28(23):2288–2290, December 2003.

[45] Pu Chun Ke and Min Gu. Characterization of trapping force on metallic particles. *Appl. Opt.*, 38(1):160–167, January 1999.

[46] Min Gu, Dru Morrish, and Pu Chun Ke. Enhancement of transverse trapping efficiency for a metallic particle using an obstructed laser beam. *Appl. Phys. Lett.*, 77(1):34 36, 2000.

[47] Erik Fällman. *Optical Tweezers: a tool for nonintrusive micromanipulation of biological objects.* PhD thesis, Umeaa University, Sweden, 2001.

[48] Francis A. Jenkins and Harvey E. White. *Fundamentals of Optics.* McGraw-Hill International Editions, fourth edition, 1981.

[49] Robin L. Garrell. Surface enhanced Raman spectroscopy. *Anal. Chem.*, 61(6):401A–411A, 1989.

[50] M. Moskovits. Surface-enhanced spectroscopy. *Rev. Mod. Phys.*, 57:783–826, 1985.

[51] A. Campion and P. Kambhampati. Surface-enhanced Raman scattering. *Chem. Soc. Rev.*, 27:241-250, 1998.

[52] Horia Metiu and Purna Das. The electromagnetic theory of surface enhanced spectroscopy. *Annual Reviews*, 35:507–536, 1984.

[53] Katrin Kneipp, Harald Kneipp, Irving Itzkan, Ramachandra R. Dasari, and Michael S. Feld. Ultrasensitive chemical analysis by Raman spectroscopy. *Chem. Rev.*, 99:2957–2975, 1999.

[54] Changan Xie, Mumtaz A. Dinno, and Yong quig Li. Near-infrared Raman spectroscopy of single optically trapped biological cells. *Opt. Lett.*, 27(4):249–251, February 2002.

[55] K. Ramser, K. Logg, M. Goksör, J. Enger, M. Käll, and D. Hanstorp. Resonance Raman spectroscopy of opticaly trapped functional erythrocytes. *J. Biomed. Opt.*, 9:593–600, 2004.

[56] Changan Xie and Yong quig Li. Raman spectra and optical trapping of highly refractive and nontransparent particles. *Appl. Phys. Lett.*, 81(6):951–953, August 2002.

[57] C. V. Raman and K. S. Krishnan. A new type of secondary radiation. *Nature*, 121:501, 1928.

[58] Michael J. Pelletier. *Analytical applications in Raman spectroscopy.* Blackwell Science Ltd, 1999.

[59] Derek A. Long. *The Raman effect: A unified treatment of the theory of Raman scattering by molecules.* Wiley, 2002.

[60] Peter Atkins and Julio do Paula. *Atkins' physical chemistry.* Oxford University Press, 7th edition, 2002.

[61] M. G. Albrecht and J. A. Creighton. Anomalously intense Raman spectra of pyridine at a silver electrode. *J. Am. Chem. Soc.*, 99(15):5215 5217, 1977.

[62] D. C. Jeanmarie and R. P. Van Duyne. Surface Raman spectroelectrochemistry part I. Heterocyclic, aromatic, and aliphatic amines adsorbed on the anodized silver electrode. *J. Electroanal. Chem.*, 84:1 20, 1977.

[63] J. A. Creighton, C. G. Blatchford, and M. G. Albrecht. . *J. Chem. Soc. Faraday Trans. II*, 75:790, 1979.

[64] P. C. Lee and D. Meisel. Adsorption and surface-enhanced Raman of dyes on silver and gold sols. *J. Phys. Chem.*, 86(17):3391. 1982.

[65] Peter Hildebrandt and Manfred Stockburger. Surface-enhanced resonance Raman spectroscopy of Rhodamine 6G adsorbed on colloidal silver. *J. Phys. Chem.*, 88:5935–5944, 1984.

[66] C. G. Blatchford, J. R. Campbell, and J. A. Creighton. Plasma resonance enhanced Raman scattering by absorbates on gold colloids: The effects of aggregation. *Surface Sci.*, 120(2):435 455, 1982.

[67] K. C. Grabar, R. G. Freeman, M. B. Hommer, and M. J. Natan. Preparation and characterization of Au colloid monolayers. *Anal. Chem.*, 67:735 743, 1995.

[68] K. C. Grabar, K. R. Brown, C. D. Keating, S. J. Stranick, S. J. Tang, and M. J. Natan. Nanoscale characterization of gold colloid monolayers: A comparison of four techniques. *Anal. Chem.*, 69:471 477, 1997.

[69] A. C. Curtis, D. G. Duff, P. P. Edwards, D. A. Jefferson, B. F. G. Johnson, A. I. Kirkland, and A. S. Wallace. Preparation and structural characterization of an unprotected copper sol. *J. Phys. Chem.*, 92:2270. 1988.

[70] H. H. Huang, F. Q. Yan, Y. M. Kek, C. H. Chew, G. Q. Xu, W. Ji, P. S. Oh, and S. H. Tang. Synthesis, characterization, and nonlinear optical properties of copper nanoparticles. *Langmuir*, 13:172 175, 1997.

[71] A. Otto. Surface enhanced Raman scattering (SERS), what do we know? *Applications of Surface Science*, 6:309–355. 1980.

[72] A. Otto. . *J. Raman. Spectrosc.*, 22:743. 1991.

[73] A. Otto, I. Mrozeck, H. Grabhorn, and W. Akemann. Surface-enhanced Raman scattering. *J. Phys. Condens. Matter*, 4:1143–1212, 1992.

[74] D. A. Guzonas, D. E. Irish, and G. F. Atkinson. Evidence for a photon-driven charge-transfer enhancement in the surface-enhanced Raman scattering of 1,4-diazabicyclo[2.2.2]octane at a silver electrode. *Langmuir*, 6:1102–1112, 1990.

[75] M. Moskovits. Surface roughness and the enhanced intensity of Raman scattering by molecules adsorbed on metals. *J. Chem. Phys.*, 69(9):4159–4161, November 1978.

[76] Roberto Rojas and F. Claro. Theory of surface enhanced Raman scattering in colloids. *J. Chem. Phys.*, 98(2):998–1006, January 1993.

[77] Joel Gersten and Abraham Nitzan. Electromagnetic theory of enhanced Raman scattering by molecules adsorbed on rough surfaces. *J. Chem. Phys.*, 73(7):3023–3037, October 1980.

[78] Joel I. Gersten. Rayleigh, Mie and Raman scattering by molecules adsorbed on rough surfaces. *J. Chem. Phys.*, 72(10):5780–5781, May 1980.

[79] Joel I. Gersten. The effect of surface roughness on surface enhanced Raman scattering. *J. Chem. Phys.*, 72(10):5779–5780, May 1980.

[80] A. M. Glass, P. F. Liao, J. G. Bergman, and D. H. Olson. Interaction of metal particles with adsorbed dye molecules: absorption and luminescence. *Opt. Lett.*, 5(9):368–370, September 1980.

[81] A. Hartstein, J. R. Kirtley, and J. C. Tsang. Enhancement of the infrared absorption from molecular monolayers with thin metal overlayers. *Phys. Rev. Lett.*, 45(3):201–204, July 1980.

[82] A. Wokaun, H. P. Lutz, A. P. King, U. P. Wild, and R. R. Ernst. Energy transfer in surface enhanced luminescence. *J. Chem. Phys.*, 79(1):509–514, July 1983.

[83] R. A. Wolkow and M. Moskovits. Enhanced photochemistry on silver surfaces. *J. Chem. Phys.*, 87(10):5858–5869, November 1987.

[84] A. M. Stacy and R. P. Van Duyne. Surface enhanced Raman and resonance Raman spectroscopy in a non-aqueous electrochemical environment: Tris(2,2'-bipyridine)ruthenium(II) adsorbed on silver from acetonitrile. *Chem. Phys. Lett.*, 102(4):365–370, 1983.

[85] A. Backackashvilli, B. Katz, Z. Priel, and S. Efrima. Surface Raman scattering of azo dyes. *J. Phys. Chem.*, 88:6185–6190, 1984.

[86] S. Efrima. Raman scattering of dye molecules adsorbed on metal surfaces. Theoretical considerations. *J. Phys. Chem.*, 89:2843–2849, 1985.

[87] Caroline Rodger, W. Ewen Smith, Geoffrey Dent, and Michael Edmondson. Surface-enhanced resonance Raman scattering: an informative probe of surfaces. *J. Chem. Soc., Dalton Trans.*, pages 791–799, 1996.

[88] Shuming Nie and Steven R. Emory. Probing single molecules and single nanoparticles by surface enhanced Raman scattering. *Science*, 275:1102–1106, February 1997.

[89] Karen Faulds, W. Ewen Smith, and Duncan Graham. Evaluation of surface-enhanced resonance Raman scattering for quantitative DNA analysis. *Anal. Chem.*, 76(2):412–417, 2004.

[90] Karen Faulds, Ramina P. Barbagallo, Jacquie T. Keer, W. Ewen Smith, and Duncan Graham. SERRS as a more sensitive technique for the detection of labelled oligonucleotides compared to fluorescence. *Analyst*, 129:, 2004.

[91] Juan Yguerabide and Evangelina E. Yguerabide. Light scattering submicroscopic particles as highly fluorescent analogs and their use as tracer labels in clinical and biological applications. *Anal. Biochem.*, 262:137-156, 1998.

[92] C. Sönichsen, T. Franzl, T. Wilk, G. von Plessen, and J. Feldmann. Plasmon resonances in large noble-metal clusters. *New J. Phys.*, 4:93, 2002.

[93] Karel Svoboda and Steven M. Block. Optical trapping of metallic Rayleigh particles. *Opt. Lett.*, 19(13):930–932, July 1994.

[94] Hiromitsu Furukawa and Ichirou Yamaguchi. Optical trapping of metallic particles by a fixed Gaussian beam. *Opt. Lett.*, 23(3):216-218, February 1998.

[95] Y. Saito, J. J. Wang, D. A. Smith, and D. N. Batchelder. A simple chemical method for the preparation of silver surfaces for efficient SERS. *Langmuir*, 18(8):2959–2961, 2002.

[96] Ebbing Gammon. *General Chemistry.* Houghton Mifflin Company. Boston, Nwew York. sixth edition, 1999.

[97] http://dwb.unl.edu/chemistry/microscale/mscale42.html.

[98] Imran Khan, Ewan Polwart, David W. McComb, and W. Ewen Smith. Correlation of optical properties with structure of immobilised nanoparticles - a method for probing the mechanism of SERRS. *Analyst*, 129(10):950–955, 2004.

[99] Robert A. Alberty and Robert J. Silbey. *Physical Chemistry.* John Wiley & Sons, 2nd edition, 1997.

[100] Bruce C. Gates. *Catalytic Chemistry.* John Wiley & Sons, 1992.

[101] Karen Faulds, Rachael E. Littleford, Duncan Graham, Geoffrey Dent, and W. Ewen Smith. Comparison of surface-enhanced resonance Raman scattering from unaggregated and aggregated nanoparticles. *Anal. Chem.*, 76(3):592–598, February 2004.

[102] Nick Barnett. Ocean optics. Personal Communication.

[103] A. Ashkin, J. M. Dziedzic, and T. Yamane. Optical trapping and manipulation of single cells using infrared laser beams. *Nature*, 330(6150):769–771, 1987.

[104] W. D. Wang, H. Yin, R. Landick, J. Gelles, and S. M. Block. Stretching DNA with optical tweezers. *Biophys. J.*, 72:1335–1346, 1997.

[105] Y. R. Shen. *The principles of nonlinear optics.* Wiley-Interscience, 1984.

[106] J. Wilson and J. F. B. Hawkes. *Lasers principles and applications.* Prentice Hall, Prentice Hall Europe, Campus 400, Marylands Avenue, Hertfordshire HP2 7EZ, 1987.

[107] Microsoft Office. Excel.

[108] Chen Tong-Sheng, Zeng Shao-Qun, Zhou Wei, and Luo Qing-Ming. A quantitative theory model of a photobleaching mechanism. *Chin. Phys. Lett.*, 20(11):1940–1943, 2003.

[109] Meindert A. van Dijk, Lukas C. Kapitein, Joost van Mameren, Christoph F. Schmidt, and Erwin J. G. Peterman. Combining optical trapping and single-molecule fluorescence spectroscopy: enhanced photobleaching of fluorophores. *J. Phys. Chem. B*, 108:6479–6484, 2004.

[110] Joel Gersten and Abraham Nitzan. Spectroscopic properties of molecules interacting with small dielectric particles. *J. Chem. Phys.*, 75(3):1139–1152, August 1981.

[111] Abraham Nitzan and L. E. Brus. Can photochemistry be enhanced on rough surfaces. *J. Chem. Phys.*, 74(9):5321–5322, May 1981.

[112] Abraham Nitzan and L. E. Brus. Theoretical model for enhanced photochemistry on rough surfaces. *J. Chem. Phys.*, 75(5):2205–2214, Spetember 1981.

[113] R. Ruppin. Decay of an excited molecule near a small metal sphere. *J. Chem. Phys.*, 76(4):1681–1684, February 1982.

[114] Krasimir Vasilev, Fernando D Stefani, Volker Jacobsen, Wolfgang Knoll, and Maximilian Kreiter. Reduced photobleaching of choromphores close to a metal surface. *J. Chem. Phys.*, 120(14):6701–6704, April 2004.

[115] Meindert A. van Dijk, Lukas C. Kapitein, Joost van Mameren, Christoph F. Schmidt, and Erwin J. G. Peterman. Combined optical trapping and single-molecule fluorescence spectroscopy: enhanced photobleaching of fluorophores. *J. Phys. Chem. B*, 108:6479–6484, 2004.

[116] Erik J. Sánchez, Lukas Novotny, Gary R. Holtom, and X. Sunney Xie. Room temperature fluorescence imaging and spectroscopy of single moleucles by two-photon excitation. *J. Phys. Chem. A*, 101(38):7019–7023, 1997.

[117] Tong-Sheng Chen, Shao-Qun Zeng, Qing-Ming Luo, Zhi-Hong Zhang, and Wei Zhou. High order photobleaching of green fluorescent protein inside live cells in two-photon excitation microscopy. *Biochem. Biophys. Res. Commun.*, 291:1272–1275, 2002.

[118] K. Vissher, G. J. Brakenhoff, and J. J. Krol. Micromanipulation by multiple optical traps created by a single fast scanning trap integrated with the bilateral confocal scanning laser microscope. *Cytometry*, 14(2):105–114, 1993.

[119] P. Korda, G. C. Spalding, E. R. Dufresne, and D. G. Grier. Nanofabrication with holographic optical tweezers. *Rev. Sci. Instrum.*, 73(4):1956–1957, April 2002.

[120] J. Liesener, M. Reicherter, T. Haist, and H. J. Tiziani. Multi functional optical tweezers using computer generated holograms. *Opt. Commun.*, 185:77–82, November 2000.

[121] M. Reicherter, T. Haist, E. U. Wagemann, and H. J. Tiziani. Optical particle trapping with computer-generated holograms written on a liquid-crystal display. *Opt. Lett.*, 24(9):608–610, May 1999.

[122] P. C. Mogensen and J. Gluckstad. Dynamic array generation and pattern formation for optical tweezers. *Opt. Commun.*, 175:75–81. February 2000.

[123] J. E. Curtis, B. A. Koss, and D. G. Grier. Dynamic holographic optical tweezers. *Opt. Commun.*, 207:169–175, June 2002.

[124] Eric R. Dufresne and David G. Grier. Optical tweezer arrays and optical substrates created with diffractive optics. *Rev. Sci. Instrum.*, 69(5):1974–1977, May 1998.

[125] E. N. Leith and J. Upatnieks. Reconstructed wavefronts and communication theory. *J. Opt. Soc. Am.*, 52:1123–1130, 1962.

[126] E. N. Leith and J. Upatnieks. Wavefront reconstruction with diffused illumination and three-dimensional objects. *J. Opt. Soc. Am.*, 54:1295–1301, 1964.

[127] P. Hariharan. *Optical holography, principles, techniques and applications.* Cambridge University Press, 1986.

[128] M. A. Seldowitz, J. P. Allebach, and D. W. Sweeny. Synthesis of digital holograms by direct binary search. *Appl. Opt.*, 26:2788, 1987.

[129] Z. J. Laczik. 3D beam shaping using diffractive optical elements. *Proc. SPIE*, 4770:104–111, 2002.

[130] R. W. Gerchberg and W. O. Saxton. A practical algorithm for the determination of the phase from image and diffraction plane pictures. *Optik*, 35:237–246, 1972.

[131] T. Haist, M. Schönleber, and H. J. Tiziani. Computer generated holograms from 3D-objects written on twisted nematic liquid crystal displays. *Opt. Commun.*, 140:299–308, 1997.

[132] D. J. Cho, S. T. Thurman, J. T. Donner, and G. M. Morris. Characteristics of a 128 x 128 liquid-crystal spatial light modulator for wave-front generation. *Opt. Lett.*, 23:969–971, 1998.

[133] I. C. Khoo, M. V. Wood, M. Y. Shih, and P. H. Chen. Extremely nonlinear photosensitive liquid crsytals for image sensing and sensor protection. *Opt. Express*, 4(11):432–442, May 1999.

[134] Matthew T. Rakher. Liquid crystals as spatial light modulators for optical quantum computation. University of Illinois, August 2002.

[135] V. soifer, V. Kotlyar, and L. Doskolovich. *Iterative methods for diffractive optical elements computation.* Taylor and Francis Ltd, London, 1997.

[136] E. R. Dufresne, G. C. Spalding, M. T. Dearing, S. A. Sheets, and D. G. Grier. Computer-generated holographic optical tweezer arrays. *Rev. Sci. Instrum.*, 72(3):1810–1816, March 2001.

[137] Gavin Sinclair, Pamela Jordan, Jonathan Leach, Miles Padgett, and Jon Cooper. Defining the trapping limits of holographical optical tweezers. *J. Mod. Opt.*, 51:409–414, 2004.

[138] Gavin Sinclair, Jonathan Leach, Pamela Jordan, Zolt John Laczik, Graham Gibson, Eric Yao, Miles J Padgett, and Johannes Courtial. Modified Gerchberg-Saxton algorithm for holographic three-

dimensional light shaping and its interactive application in optical tweezers. *Opt. Express*, 12:1665–1670, 2004.

[139] Edward A. Sziklas and A. E. Seigman. Mode calculations in unstable resonators with flowing saturable gain. 2: Fast fourier transform method. *Appl. Opt.*, 17(8):1874–1889, August 1975.

[140] C. Mio and D. W. M. Marr. Tailored surfaces using optically manipulated colloidal particles. *Langmuir*, 15:8565–8568, 1999.

[141] J. P. Hoogenboom, D. L. J. Vossen, C. Faivre-Moskalenko, M. Dogterom, and A. van Blaaderen. Patterning surfaces with collodial particles using optical tweezers. *Appl. Phys. Lett.*, 80(25):4828–4830, June 2002.

[142] Robert H. Webb. Confocal optical microscopy. *Rep. Prog. Phys.*, 59:427–471, 1996.

[143] A. I. Savchuk, V. I. Fediv, Y. O. Kandyba, T. A. Savchuk, I. D. Stolyarchuk, and P. I. Nikitin. Platelet-shaped nanoparticles of PbI_2 and $PbMnI_2$ embedded in polymer matrix. *Mat. Sci. Eng. C-Bio. S.*, 19:59–62, 2002.

[144] Katharine E. Stitzer, Mark D. Smith, and Hans-Conrad zur Loye. Crystal growth, structure determination and magnetic properties of $Ba_4Ir_3O_{10}$ and $Ba_4(Co_{0.4}Ir_{0.6})Ir_2O_{10}$. *J. Alloy Compd.*, 338:104–111, 2002.

[145] A. D. Yoffe. Low-dimensional systems: quantum size effects and electronic properties of semi-conductor microcrystallites (zero-dimensional

systems) and some quasi-two-dimensional systems. *Adv. Phys.*, 42(173), 1993.

[146] A. D. Yoffe. Semiconductor quantum dots and related systems: electronic, optical, luminescence and related properties of low dimensional systems. *Adv. Phys.*, 50(1):1–208, 2001.

[147] J. C. Y. Dunn, M. L. Yarmush, H. G. Koebe, and R. G. Tompkins. Hepatocyte function and extracellular-matrix geometry - long-term culture in a sandwich configuration. *Faseb. J.*, 3:174–177, 1989.